Calculation of quantum mechanical rate constants directly from ab initio atomic forces

Andri Arnaldsson

A dissertation submitted in partial fulfillment
of the requirements for the degree of

Doctor of Philosophy

University of Washington

2007

Program Authorized to Offer Degree: Chemistry

University of Washington
Graduate School

This is to certify that I have examined this copy of a doctoral dissertation by

Andri Arnaldsson

and have found that it is complete and satisfactory in all respects,
and that any and all revisions required by the final
examining committee have been made.

Chair of the Supervisory Committee:

_____

Hannes Jónsson

Reading Committee:

_____

Hannes Jónsson

_____

William P. Reinhardt

_____

Oleg V. Prezhdo

Date: _____

Signature_____

Date_____

University of Washington

Abstract

Calculation of quantum mechanical rate constants directly from ab initio atomic forces

Andri Arnaldsson

Chair of the Supervisory Committee:
Professor Hannes Jónsson
Chemistry

Harmonic quantum transition state theory (HQTST), sometimes referred to as 'instanton theory' or 'ImF theory', has been implemented in an efficient way and tested. HQTST is analogous to the more familiar classical harmonic transition state theory (HTST), where the rate is estimated from the energy difference between a reactant state minimum and a first order saddle point on the potential energy surface ridge that separates reactants and the products, along with a prefactor derived from harmonic expansion of the potential around both the minimum and the saddle point. The method described here makes use of a generalized minimum mode following method to locate saddle points on the effective quantum mechanical energy surface for discretized Feynman path integrals (FPI). The overall computational cost of estimating rate constants with this method is relatively low and it is possible to use directly atomic forces obtained from first principle calculations. The method is also well suited for systems containing many degrees of freedom, on the order of a few hundred. Usually, a well converged results is achieved with 500 - 700 force calls per system replica used to represent the FPI.

The method has been tested on several one- and two-dimensional systems where more accurate (or even analytical) solutions for the rate constant can be obtained. Not only is it found to robust and fast, but accurate as well, yielding results within a factor of 2-3 from the exact values, indicating that the approximations inherent in the procedure are

well justified for chemically relevant systems. In addition, the method has been used for calculating the rate of various transitions involving hydrogen atoms or molecules where the atomic forces are derived from empirical, semi-empirical or first principle calculations. Calculations presented here include the rate of hydrogen abstraction from gas phase H_3BN_3, hydrogen atom diffusion in Ta and Pd, adsorption/desorption of H_2 onto/from Cu(100) and Cu(110) surfaces and hydrogenation of N on Ru(0001) surface. Comparison is made with either higher level theoretical calculations or experimental results when available, and the agreement is found to be good in all instances.

TABLE OF CONTENTS

Page

LIST OF FIGURES

LIST OF TABLES

GLOSSARY

AB-INITIO: From first principles. This expression can mean different things in different fields. In the field of quantum chemistry, it means that a calculation was done by solving Schrödinger's equation for the electrons in the system without using any empirical data. In solid state physics the term also includes methods such as density functional theory.

CLASSICAL DYNAMICS: The time evolution of Newton's equations for a classical system.

CFP: Closed Feynman path

CLOSED FEYNMAN PATH: The Feynman paths that are periodic in imaginary time, that is start and terminate in the same point. Since the quantum partition function is given by the trace of the density matrix, it is represented only with closed Feynman paths.

DENSITY FUNCTIONAL THEORY: An approximate method of solving Schrödinger's equation for a system of electrons. The energy and force of the system is calculated from the electron density. DFT scales better than many-body orbital based quantum chemistry methods and can be used with larger systems.

DIMER METHOD: A method for finding saddle points that requires energy and force but not second derivatives. The dimer method can be used to find many different saddle points on the potential energy rim surrounding a potential minimum.

DFT: Density functional theory.

EAM: Embedded atom method.

EMBEDDED ATOM METHOD: A form of empirical potential function which quite accurately describes some metals including aluminum, nickel, silver and copper.

FPI: Feynman path integral

FEYNMAN PATH INTEGRAL: One formulation of quantum mechanics. The probability of a particle starting from a given configuration and ending at another some time later is given by an integral over all possible path connecting the two configurations. In real time it describes quantum dynamics and in imaginary time, quantum statistical dynamics.

HARMONIC TRANSITION STATE THEORY: A simplified form of transition state theory in which the potential is assumed to be of harmonic form both at the minimum and at the saddle point. This is a good approximation at low enough temperature, unless quantum effects become important. It typically works well for metals at room temperature.

HTST: Harmonic transition state theory.

HESSIAN MATRIX: The matrix of force constants (second derivatives of the potential energy). When this matrix is divided by the masses of the atoms, the eigenvectors are the normal modes, and the eigenvalues are the square of the normal mode frequencies.

INSTANTON: Stationary phase approximation to the thermal Boltzmann operator. In the context of this study, the instanton is the saddle point along the MAP. That is, the CFP with the highest action. It is the quantum mechanical analog to the classical saddle point in hTST.

MAP: Minimum action path

MEP: Minimum energy path.

MINIMUM ACTION PATH: Optimal sequence of closed Feynman paths connecting the reactant and product states and passing through the instanton. The path has the highest statistical relevance in the quantum mechanical partition function since it represents the lowest action.

MINIMUM ENERGY PATH: A path between two points on a potential surface of the lowest possible energy. This path follows the direction of steepest descent.

NEB: Nudged elastic band.

NUDGED ELASTIC BAND: A method for finding the minimum energy paths between two points on a potential surface. A path of discrete images of a system are connected by springs (elastic band) and allowed to collectively relax. The 'nudging' refers to the fact that the spring forces act only along the band, and the potential forces act only perpendicular to the band. Typically this method is used to find the MEP and saddle point(s) between two potential minima.

PES: Potential energy surface.

POTENTIAL ENERGY SURFACE: Each point in configuration space represents one configuration or position of the atoms in the system. For this position, there is a potential energy. The potential energy surface is the surface defined by the value of the potential energy at each point in configuration space.

SADDLE POINT: A point on a potential surface at which the force is zero and at which there is one negative curvature or unstable mode in the Hessian matrix.

TRANSITION STATE: A bottle neck region which a system must cross in order to undergo a transition from a given initial state. The transition state has dimension one less than the full system.

TRANSITION STATE THEORY: A theory for calculating the rate at which a system leaves a given initial state (potential energy basin) though a bottle neck region.

TST: Transition state theory.

ACKNOWLEDGMENTS

First of all I want to thank my scientific advisor, Professor Hannes Jónsson. If it had not been for his remarkable insight into chemical physics and persistence, this project most likely would had perished some years ago.

I want to acknowledge my amiable office mates in Bagley Hall 311A, Graeme Henkelman and Kiril Tsemekhman, both for teaching me a great deal about theoretical/computational chemistry, as well for their camaraderie. Our various collaborators, Thomas Bligaard (DTU CAMP), Gregory Schenter (PNNL), Stefan Andersson (Göteborg University) and Roar Olsen (University of Leiden) have contributed to my understanding of the subject to a great extend.

Finally, I want to express my sincerest gratitude to all the people (and satellites) in the Theory suite, all of the past and present members of Hannes's group, both here at the University of Washington and the University of Iceland, as well as my dears friends and family that have supported me through the years. Combined, they probably contributed more to this project than they can ever imagine.

DEDICATION

To Laura for keeping my espresso strong and Nicole for keeping the bourbon stiff.

Chapter 1

INTRODUCTION

At the heart of physical chemistry and chemical physics lies reaction rate theory. It is also of importance in solid state physics, for example in studies of diffusion and materials processing. In principle, the study of transitions requires the study of dynamics, i.e. classical or quantum dynamics of atoms should be followed to obtain an estimate of the rate of transitions from one atomic configuration to another. But, such a direct approach fails because of the disparity between the time scale of atomic vibrations and the time scale of transitions involving significant rearrangements of the atoms. Typically, the thermal energy, $k_B T$, that is available to a system per degree of freedom is much smaller than a typical energy barrier separating two metastable states of the system. The motion of the atoms is most of the time simply vibrations back and forth within a well or a basin representing a stable or metastable state and only rarely does a fluctuation bring the system from one state to another over a free energy barrier. The system spends most of its time fluctuating within one of the metastable states and only infrequently do the random thermal fluctuations combine in such a way that a barrier crossing becomes possible. Assuming Arrhenius behavior and a typical prefactor of 10^{13} s^{-1}, combined with a low energy barrier of 0.5 eV (48 kJ/mol), a barrier crossing event will on average occur tens of times per microsecond at 300 K. Molecular vibrations, however, occur on a time scale of tens of femtoseconds (10^{-14} s) so it would on average be necessary to follow a trajectory in a dynamics simulation for about 10^{10} vibrational periods in order to observe a transition. In a typical simulation algorithm the time step for a dynamical trajectory is a tenth of a vibrational period, so 10^{11} time steps would need to be simulated. With current computer technology and any technological advances in the foreseeable future, this presents an insurmountable task even when a simple, classical description of the atomic dynamics is used. When a quantum

mechanical description of the atoms is required, as is sometimes the case, the calculation of the dynamics is many orders of magnitude more difficult.

The disparity of time scales between atomic vibrations and thermally induced transitions makes it impossible to simply follow the dynamical evolution of a system in order to study typical, thermally activated transitions in chemistry and solid state physics. Rather, a statistical theory needs to be applied. The most successful approach is transition state theory (TST). It is well established and widely used for calculating rates of thermally activated processes in systems where the motion of the atoms can be described with classical dynamics. The main strength of TST is that the rate at which a transition takes place can be calculated statistically instead of dynamically. Classically, the rate could be estimated by following a swarm of dynamical trajectories by integrating Newton's equations motion forward in time and count how many managed to move from the reactant state to the product state over a given time interval. A more feasible way, as presented by TST, is to estimate the statistical probability of finding the system in a *transition state* between the reactants and products and calculating the flux out from the transition state towards the products. The problem is reduced from having to explicitly follow each coordinate's time evolution by solving Newton's equations of motion to one where the reaction rate is proportional to the relative probability of the system coordinates to be found at a *transition state*. The dynamical problem is transformed into a problem of evaluating a thermodynamic partition function.

Given that a system adheres to the basic assumption of TST, remarkably accurate results can be achieved over a wide range of temperature. The assumptions made in TST are: (1) that the time scales be such that a thermal equilibrium is maintained for each degree of freedom in the initial state throughout the process, and (2) that a dividing surface between reactant and product regions can be found so that each trajectory which originates in the reactant state and crosses the dividing surface will end up on the product side without crossing the dividing surface again. Most often the dividing surface is chosen to be a hyperplanar surface located in a region where the potential energy is high. But, it is, in fact, not necessary for there to be an energy barrier separating the reactants and products, entropic barriers suffice as well. For instance, effusion of particles from a pressured

container through a pin hole is exactly described by TST. The recrossing criterion leads to a variational principle since some of the paths crossing the dividing surface will not end up in the product state but instead recross the surface, heading towards the reactants again. Any recrossing of the dividing surface results in an overestimation of the true rate. The TST rate is a rigorous upper bound to the true rate. Through the variational principle [1, 2], a dividing surface in configuration space can be found, that separates the products and the reactants and minimizes the rate. Optimization of the location [3] and shape of the dividing surface such that the number of recrossings is minimized is generally referred to as variational TST (VTST). In some cases, a hyperplanar dividing surface cannot give a good rate estimate and it is then important to allow the surface to curve and bend freely so as to minimize the calculated rate. However, finding such a surface in high dimensional space is practically impossible, although some success has been made for low dimensional systems [4]. No matter what dividing surface is used, it is in principle possible to correct the TST estimate of the rate constant by running classical trajectories from the transition state and counting the recrossings. However, such a calculation becomes impractical unless the dividing surface is chosen well. The combination of a VTST followed by dynamical corrections due to recrossings represents a two step algorithm for calculating the exact rate constant without ever having to run the impossibly long trajectories that start at the initial state.

Within the harmonic approximation to TST, HTST, the transition state is chosen to be a hyperplane that contains the highest saddle point on the potential energy surface that lies on the minimum energy path that connects the reactant and product energy minima. A rate constant can then be obtained if one can find this saddle point and evaluate the frequency of the vibrational modes both at the saddle point and the initial state. This is the form of TST that is most often used. First principles calculations, where the electronic degrees of freedom are solved using the Schrödinger equation, are routinely coupled to HTST to estimate rates since the computational effort of finding saddle points and the vibrational frequencies is not too large, typically on the order of 1000 force evaluations. The combination of full TST in conjunction with first principles methods is however rarely done. The computational effort is still too large, on the order of 100,000 force evaluations.

Transition state theory is inherently classical. However, it is well known that quantum mechanical effects can be important especially when light atoms such as hydrogen are involved in the transition. Such effects can be due to the fact that a quantum particle is delocalized and therefore cannot have the minimum potential energy - the zero point energy effect. A stronger quantum effect, which again is a consequence of the quantum delocalization, is the possibility that a quantum mechanical particle tunnels from one local minimum to another on the potential energy surface. For several systems, such as hydrogen atom diffusion in metals, a drop in the effective activation energy as temperature is lowered has been interpreted as onset of such quantum, tunneling mechanism. The extension of TST to quantum systems has been a long standing effort and is still a matter of active research. It is even more important for quantum systems to apply some kind of TST approximation and get away from calculating dynamical evolution of the system and evaluate statistical properties instead, as is done in TST. Accurate quantum dynamics calculation can only be performed for very short periods of time and for systems with only a few degrees of freedom, on the order of 6 or so. Various theoretical approaches have been developed. The most successful ones rely upon the imaginary time Feynman path integral (FPI) [5] formalism of quantum mechanics as pioneered by Gillan [6] and later developed further by Voth, Chandler and Miller [7], and by Messina, Schenter and Garrett [8] and by Mills, Schenter, Makarov and Jónsson [9, 10, 11]. The evaluation of the rate constant with those methods requires many force evaluations, many more than full, classical TST, and is therefore not practical to use in combination with first principles methods.

A harmonic version of FPI based quantum transition state theory, HQTST, has been developed and is generally referred to as 'instanton theory'. It requires much fewer force calculations in the evaluation of a rate constant, although many more than classical HTST. The goal of the work presented in this thesis was to develop an efficient implementation of instanton theory to make it possible to carry out calculations of quantum mechanical rate constants that include the tunneling mechanism directly from first principles atomic forces. This implementation is described in Chapter 2. Chapter 3 reports on a few test cases to assess the accuracy of the HQTST method and Chapter 4 reports on rate constant calculations using first principle atomic forces. The rest of chapter 1 is devoted to a review

of the various flavors of rate theory, both classical and quantum mechanical.

1.1 Classical transition state theory

If the transition state (TS) represents a tight bottle neck for going from reactants (R) to products (P), then one can approximate the rate constant in a simple way

$$\begin{aligned} k_{\mathrm{TST}} &= (\text{probability of making it to the TS}) \cdot (\text{rate of crossing TS from R to P}) \\ &= \frac{\sigma \int_{\ddagger} e^{-V(\vec{x})/k_B T}\, d\vec{x}}{\int_R e^{-V(\vec{x})/k_B T}\, d\vec{x}} \frac{< v_\perp >}{\sigma} \end{aligned} \tag{1.1}$$

where $< v_\perp >$ is the average velocity in crossing the TS, in a direction normal to the dividing surface and σ is the width of the transition state. Since the width of the TS is infinitesimal, the potential energy can be taken to be constant in the direction normal to the dividing surface. The key assumption here is that if the system leaves the TS in the direction towards the product region, P, then the system will continue to stay in the product region and spend an extended time there until another energetic fluctuation takes it back to R. This is the central approximation in TST. This is a good approximation if the dynamics are simple and the classical trajectories do not go back and forth over the dividing surface before landing in either R or P. The other two other approximations in TST are the assumption that classical dynamics on the Born-Oppenheimer surface are a valid description of the dynamics, and that the reactant has reached equilibrium conditions, i.e. the energy in each degree of freedom is described by the Boltzmann distribution. For a typical transition rate, there is a very large number of vibrations in between reactive events (on the order of 10^{10}), so the last approximation is usually an excellent one.

The average velocity in crossing the TS $< v_\perp >$ can be calculated from the Maxwell distribution

$$< v_\perp > = \frac{\int_0^\infty v\, e^{-\sum_i \frac{1}{2}\mu v^2/k_B T}\, dv}{\int_{-\infty}^\infty e^{-\sum_i \frac{1}{2}\mu_i v_i^2/k_B T} dv} = \sqrt{\frac{k_B T}{2\pi\mu}} \tag{1.2}$$

Here μ is an effective mass for the motion across the TS, a linear combination of the masses of the atoms that get displaced in the transition, $\mu = \sum \mu_i n_i^2 \mathrm{m}$, where n_i are the components of the normalized vector representing the unstable mode at the transition state. The TST

approximation to the rate constant can then be written as

$$k_{\mathrm{TST}} \;=\; \sqrt{\frac{k_B T}{2\pi\mu}}\;\frac{Z^{\ddagger}}{Z^{R}} \tag{1.3}$$

where Z (configurational integrals) denotes the integral of the Boltzmann factor over the specified region of configuration space.

1.1.1 Variational classical transition state theory

If a classical trajectory crosses the TS and then for some reason gets reflected and ends up again in the reactant region, R, before settling down in the product region, then the TST approximation will have overcounted the number of reactive trajectories and the TST rate constant estimate will be too high. Also, if a trajectory crosses the dividing surface three times, the TST approximation will count that as two reactive trajectories even though it really is only one. Again the TST approximation will lead to an overestimate of the rate constant. It can be shown that these and other corrections to the "no recrossing" approximation in TST all lead to an overestimate, so we have

$$k_{\mathrm{TST}} \;\geq\; k_{\mathrm{exact}} \tag{1.4}$$

This gives a variational principle for placing the dividing surface, i.e. one can vary its position so as to obtain a minimal value of k_{TST}. That is the best estimate that can be obtained from TST. It can be shown that this minimization of k_{TST} corresponds to finding the dividing surface that has the maximum free energy. This is referred to as variational TST (VTST).

If a good dividing surface is found, then the TST estimate of the rate constant is typically within a factor of two or so of the exact rate constant. This is typically accurate enough, there are other errors that tend to be more important, such as the construction of the potential energy surface. However, if a more accurate estimate of the rate constant is needed, then it is quite easy to start classical trajectories from the TS and count how often recrossings occur. This only requires short trajectories because the system falls quite rapidly from the TS towards either R or P. This way a correction factor, κ, can be computed such

that

$$k_{\text{exact}} \;=\; \kappa \; k_{\text{TST}} \tag{1.5}$$

In the end, TST is then just an intermediate construct that enables the computation of k_{exact} without having to do the impossibly long classical dynamics calculations of a trajectory that oscillates back and forth in the reactant region before getting a rare, high energy kick from the heat bath that is large enough to make it through the bottle neck region.

1.2 Harmonic, classical transition state theory

For systems where the atoms are vibrating about fixed average positions, such as atoms in solids, or molecules reacting on the surface of a solid, the region of the potential surface that is of greatest importance can be represented by a harmonic approximation. For a diatomic molecule, the interaction potential, which is only a function of the distance between the atoms, can be expanded in a Taylor expansion that gets truncated at the second power to give $v(r) \;\approx\; v(r_0) + \frac{1}{2}kx^2$ where $x \;=\; r - r_0$ and r_0 is the distance at which the potential energy is minimal. The generalization of this to systems with more than one vibrational degree of freedom involves the calculation of normal mode coordinates, q_i. The normal mode expansion can be carried out for any point on the potential energy surface, in particular at the minimum in the potential surface corresponding to R. Since the force is zero at the minimum, the first derivative of the potential vanishes and the expansion of the potential is

$$V^R(\vec{x}) \;\approx\; V_{min} \;+\; \sum_i^D \frac{1}{2} k_i^R q_{R,i}^2 \tag{1.6}$$

in the region close to the minimum. Here, V_{min} is the energy at the minimum, k_i^R are the force constants for each normal mode and D is the number of degrees of freedom. While this will not be a good approximation for regions far from the minimum, the approximation is good enough if the potential energy is high enough in those regions that the probability of finding the system there is insignificant.

If the dividing surface is chosen to lie along the potential energy ridge that separates the reactant state from the product state, then the most important point on the dividing surface, the point with largest statistical weight, is a saddle point. It is a minimum with

respect to all the degrees of freedom within the dividing surface, but a maximum with respect to the motion normal to the dividing surface. If more than one saddle point exists on the potential energy ridge, then the lowest energy one is most important. Let's assume there that there is only one saddle point, and carry out a Taylor expansion there of the potential energy within the dividing surface

$$V^{\ddagger}(\vec{x}) \;\approx\; V_{SP} \;+\; \sum_{i}^{D-1} \frac{1}{2} k_i^{\ddagger} q_{\ddagger,i}^2 \tag{1.7}$$

The first term on the right, V_{SP}, is the energy at the saddle point. The normal mode corresponding to motion normal to the dividing surface is not included. The width, σ, of the TS is so small normal to the dividing surface that the potential is taken to be constant in that direction. With these approximations to the potential energy surface, the TST expression for the rate constant becomes the harmonic TST (HTST) approximation

$$k_{\rm HTST} \;=\; \sqrt{\frac{k_B T}{2\pi\mu}}\; \frac{Z^{\ddagger}}{Z^R} \;=\; \sqrt{\frac{k_B T}{2\pi\mu}}\; \frac{\int_{-\infty}^{\infty} e^{-\sum_i^{D-1} \frac{1}{2} k_i^{\ddagger} q_{\ddagger,i}^2 / k_B T}\; dq_{\ddagger,i}}{\int_{-\infty}^{\infty} e^{-\sum_i^{D} \frac{1}{2} k_i^{R} q_{R,i}^2 / k_B T}\; dq_{R,i}} \tag{1.8}$$

For each one of the normal modes

$$\int_{-\infty}^{\infty} e^{-\frac{1}{2} k_i q_i^2 / k_B T}\; dq_i \;=\; \sqrt{\frac{2\pi k_B T}{k_i}} \tag{1.9}$$

So,

$$k_{HTST} \;=\; \sqrt{\frac{k_B T}{2\pi\mu}}\; \frac{\Pi_i^{D-1} \sqrt{\frac{2\pi k_B T}{k_{\ddagger,i}}}}{\Pi_i^{D} \sqrt{\frac{2\pi k_B T}{k_{R,i}}}}\; e^{-(V_{SP}-V_{min})/k_B T} \tag{1.10}$$

The factors of $k_B T$ cancel out and all factors of 2π except for one

$$k^{HTST} \;=\; \frac{1}{2\pi}\; \frac{\Pi_i^{D} \sqrt{k_{R,i}/\mu_i}}{\Pi_i^{D-1} \sqrt{k_{\ddagger,i}/\mu_i}}\; e^{-(V_{SP}-V_{min})/k_B T} \tag{1.11}$$

Here, the square root of the effective mass for the normal modes has been multiplied both in the numerator and the denominator. Recall that the vibrational frequency is $\nu \;=\; \omega/2\pi \;=\; \frac{1}{2\pi}\sqrt{\frac{k}{\mu}}$ so

$$k_{HTST} \;=\; \frac{\Pi_i^{D} \nu_{R,i}}{\Pi_i^{D-1} \nu_{\ddagger,i}}\; e^{-(V_{SP}-V_{min})/k_B T} \tag{1.12}$$

The HTST approximation agrees with the empirically observed Arrhenius expression for the temperature dependence of the rate constant. It is simply the potential energy difference

between the saddle point and the minimum corresponding to the reactant region. The prefactor has to do with the vibrational entropy. If the vibrational frequencies are low at the saddle point compared with the minimum, corresponding to a wide mountain pass, then the prefactor is large. If the potential energy rises quickly away from the SP within the dividing surface, quicker than in the vicinity of the minimum, then the prefactor is small.

So far, only vibrational contribution to the partition functions has been considered. Assuming separability of the various degrees of freedom, contributions from translational, rotational and electronic partition functions can be properly accounted for by [12]

$$Q(T) = Q_{\text{elect}} Q_{\text{trans}} Q_{\text{rot}} Q_{\text{vib}}. \tag{1.13}$$

How the individual terms are treated is discussed in Sec. (1.5). Most often in this thesis, the simple case of only vibrational contributions will be used

$$k_{\text{HTST}}(T) = \frac{1}{2\pi} \frac{\prod_i^{3N} \omega_i^R}{\prod_i^{3N-1} \omega_i^{\ddagger}} \exp\left(-\Delta E / k_B T\right) \tag{1.14}$$

where N is the number of atoms used, ω's are the angular vibrational (harmonic)-frequencies of the reactant state and the saddle point and ΔE is the energy difference between the two configurations on the Born-Oppenheimer surface. Note that the imaginary frequency, corresponding to the unstable vibrational mode at the saddle point is left out from the product.

1.3 Quantum mechanical corrections to TST

The discussion above has been entirely in terms of classical mechanics. At low temperature the classical treatment of the atomic motion is often not good enough. First of all, one needs to take into account the zero point energy of the vibrational ground state. In the most extreme case, one needs to take into account that the system might tunnel from the reactant configuration to the the final product configuration. The full extension of TST to quantum systems is still an area of active research. Often, the effect of quantum delocalization is added to TST calculations by including zero point energy in the activation energy. This is then done replacing $V_{min} - V_{SP}$ by

$$E_a \;=\; \left(V_{SP} \;+\; \sum_i^{D-1} \frac{h\nu_{\ddagger,i}}{2}\right) - \left(V_{min} \;+\; \sum_i^{D} \frac{h\nu_{R,i}}{2}\right) \tag{1.15}$$

Since there is one fewer vibrational mode at the SP than at the minimum, the addition of the zero point energy tends to reduce the energy barrier. One consequence of this is that transitions involving the displacement of a deuterium atom tend to have higher barrier than transitions where a hydrogen atom is displaced. The zero point energy of deuterium is smaller because of the larger mass (more classical). This is often referred to as the kinetic isotope effect. However, this is not necessarily so, if the vibrational frequencies are higher at the SP than at the minimum, then the total zero point energy at the SP can be higher than at the minimum, even though there is one fewer modes there. This can lead to the so called *reverse* isotope effect. The use of such a zero point energy correction in thermally activated transitions where the system is necessarily confined to the ground vibrational state is, however, of questionable validity. This issue is addressed in the appendix in calculations of methane and hydrogen desorption from Ni(111) surface.

Another particularly simple way to introduce quantum effects into the rate expression is to substitute the classical partition function, especially for vibration, with their quantum mechanical analogs. With that, Eq. (1.14) becomes

$$k_{\mathrm{qq-HTST}}(T) = \frac{k_B T}{2\pi h} \frac{\prod_i^{3N} 2\sinh\left(\hbar\omega_i^R/2k_BT\right)}{\prod_i^{3N-1} 2\sinh\left(\hbar\omega_i^{TS}/2k_BT\right)} \exp\left(-\Delta E/k_BT\right). \tag{1.16}$$

This introduces zero point energy in a more self-consistent manner than simply adding it to the exponent. Still, no tunneling has been accounted for.

A more elaborate method, which includes quantum effects along the reaction coordinate is the small curvature tunneling (SCT) approximation [13, 14, 15]. The SCT approximation is based on considering a harmonic expansion of the potential energy surface written in terms of the reaction coordinate, s, and the $3N$-1 orthonormal normal modes of vibration, centered along s. Averaging the resulting Hamiltonian over the the vibrational degrees of freedom introduces an *effective* mass into the one dimensional description of the system movement along the reaction coordinate. The effective mass can be interpreted in terms of the curvature along the reaction coordinate. In the standard WKB semi-classical approximation [16, 17, 18] the rate is approximated as ratio of (canonical)-probability of a nonclassical transmission through the barrier over the classical probability, multiplied by

the classical rate constant

$$k^{\mathrm{SCT}}(T) = \frac{\int_0^\infty P(E)\exp(-E/k_BT)dE}{\int_0^\infty H(E-V(s^\ddagger))\exp(-E/k_BT)dE}\; k_{\mathrm{classical}}(T) \tag{1.17}$$

with $H(...)$ as the Heaviside function, $V(s^\ddagger)$ as the maximum along the reaction coordinate and where the transmission probability is given by

$$P(E) = \{1+\exp 2\theta(E\}^{-1} \tag{1.18}$$

and $\theta(E)$ is the imaginary action integral

$$\theta(E) = \frac{1}{\hbar}\int_{s_<}^{s_>} \{2\mu(s)[V(s)-E]\}^{1/2}\,. \tag{1.19}$$

Here $s_<, s_>$ are the turning points for the classically forbidden region, ($V(s_<) = V(s_>) = E$). By including tunneling from the classically forbidden region, where the momentum is imaginary (negative kinetic energy) a negative centrifugal effect is introduced. So instead of moving outwards away from the path, the system climbs up along the inside wall of the potential (cuts the corner), effectively shortening the reaction path and making the reaction barrier look lower and thiner to the penetrating particle [19]. Both contribute to an increased reaction rate, as compared to purely classical over-the-barrier movement By including the effective mass, the imaginary action integral becomes.

$$\theta(E) = \frac{1}{\hbar}\int_{s<}^{s>} \{2\mu_{\mathrm{eff}}(s)[V(s)-E]\}^{1/2} \tag{1.20}$$

where the mass has been substituted with an effective tunneling mass, μ_{eff}. The effective mass can be calculated by setting up Hessian matrices along the reaction path and diagonalizing. In addition, the curvature of each vibrational mode must be found along the reaction coordinate. Although Hessian matrices can be updated along the path starting from a few neighboring exact matrices via a Bofill [20] updating scheme, this procedure is still prohibitively expensive for large systems. If the reaction path curvature is ignored then $\mu_{\mathrm{eff}} = \mu$ and tunneling along the classical reaction coordinate is recovered. For further information, see [13, 14, 15].

1.4 Quantum rate theory based on Feynman path integrals

In Feynman's formalism for quantum statistical dynamics, a quantum partition function, Q, is the trace of the equilibrium, thermal density matrix, ρ. The density matrix is directly derived from the real-time propagator from quantum dynamics, which gives the amplitude for a system to go from q_1 to q_2 in time t, by introducing a Wick rotation where the real time is rotated to pure imaginary time. The density matrix is

$$\rho(q_1, q_2, \beta\hbar) = \int e^{-S_E[q(\tau)]/\hbar}\ \mathcal{D}[q_{1\to 2}(\tau)]. \tag{1.21}$$

Here $\mathcal{D}[q_{1\to 2}(\tau)]$ extends over all possible paths connecting q_1 and q_2 in (imaginary) time $\beta\hbar$ where each path is weighted by the exponent of the corresponding Euclidian action ($S_E = \int_0^{\beta\hbar} H d\tau$) and where H is the classical Hamiltonian. In the real time quantum dynamics, the action is a time line integral of the classical Lagrangian. When imaginary time is substituted for real time in the Lagrangian, two 'i' will change the sign on the potential energy term, converting the Lagrangian to a Hamiltonian. By considering the trace of the density matrix, the quantum partition function is obtained,

$$\begin{aligned} Q &= \mathrm{Tr}(\rho(q_1, q_2, \beta\hbar)) && (1.22)\\ &= \int e^{-S_E[q(\tau)]/\hbar}\ \mathcal{D}[q_{1\to 1}(\tau)]. && (1.23) \end{aligned}$$

Since the trace Tr operates on the diagonal of the density matrix, only closed paths are included. Thus the quantum partition function relies only on paths starting at configuration q_1, traveling along a path for $\beta\hbar$ time units and then returning to the point of origin. Such paths will be called *closed Feynman paths* (CFP). The period of the path is $\beta\hbar$.

For transitions in classical systems, the path with largest statistical weight is the minimum energy path, MEP, which can be represented as a chain of system replicas stretching from the reactant region to the product region in configuration space in such a way that the perpendicular force on each replica is zero and the replicas are connected together via springs obeying Hook's law. This is effectively the picture provided by the NEB (Nudged Elastic Band) method for finding MEPs [21]. The point of highest energy along the MEP is a saddle point and the transition state in HTST is chosen to be a hyperplane that includes

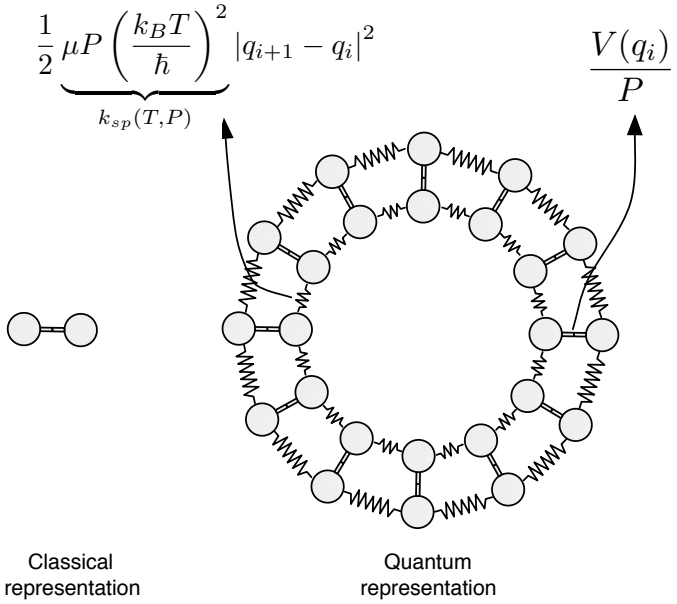

Figure 1.1: Closed Feynman path (CFP) for a diatomic molecule. The classical molecule is situated on the left hand side of the figure, the quantum mechanical CFP on the right. P is the number of system replicas (here $P = 12$). The kinetic energy term (due to the imaginary time) is presented as springs with temperature dependent spring constants (k_{sp}) between the system replicas where each atom is connected to itself in the neighboring replicas and the interatomic (within each replica) potential energy is scaled by the number of replicas. Given a high enough temperature the springs will contract the CFP to the classical configuration.

the saddle point. The quantum mechanical analog of the MEP is the MAP (minimum action path) [9]. Along the MAP, each point is a CFP and the MAP is traced out in such a way as to be parallel to the gradient of the Euclidian action in each point and the neighboring CFPs are connected through Hook springs. Being the path of least action, the MAP is the path that contributes most to the quantum partition function. The CFP of maximum action along the MAP (the saddle point) is a saddle point of an extended, quantum mechanical energy surface and is called the *instanton* [22].

In accordance with harmonic transition state theory, the task is to locate the saddle point along the MAP, i.e. the point of maximum action along the MAP. By using a discrete

Euclidian action along the CFP, gives

$$S_E(\mathbf{q}) = \Delta\tau \sum_{j=1}^{P} \left[\frac{\mu}{2} \left| \frac{q_{\mathrm{mod}(k,P)+1} - q_j}{\Delta\tau} \right|^2 + V(q_j) \right]. \tag{1.24}$$

Here the mod subscript is used because the CFP is periodic, system replica with coordinates q_P is connected to system replica with coordinates q_1., $\Delta\tau = \tau/P = \hbar/k_B T P$ is the imaginary time step and μ is the mass of each degree of freedom. The CFP has been made discrete by placing P system replicas along the closed path. This discrete path integral formulation becomes exact as $P \to \infty$ [5]. Each replica has a set of coordinates, denoted by q and the appropriate subscript. The coordinates for the entire CFP is denoted by boldfaced $\mathbf{q}$. In terms of vector lengths, the q's are of length N (the number of degrees of freedom) and q is of length NP, where P is the number of systems replicas in the CFP.

Since it is intuitively simpler to think of potentials (at least for chemists) rather than action, it can be beneficial to introduce the temperature dependent spring constant $k_{sp}(T)$ such that

$$k_{sp}(T) \;=\; \mu P \left(\frac{k_B T}{\hbar} \right)^2. \tag{1.25}$$

A simple rearrangement of Eq. (1.24) yields

$$S_E(\mathbf{q}) = \frac{\hbar}{k_B T} \underbrace{\sum_{k=1}^{P} \left[\frac{1}{2}\, k_{sp}(T) \left| q_{\mathrm{mod}(k,P)+1} - q_k \right|^2 + \frac{V(q_k)}{P} \right]}_{V_{eff}(\mathbf{q},T)} \tag{1.26}$$

where the sum has been defined to be some *effective* potential energy surface since it has units of energy. It is equivalent to weigh each closed path in the quantum partition function (Eq. (1.23)) by $\exp(-S_E(\mathbf{q})/\hbar)$ or by $\exp(-V_{eff}(\mathbf{q},T)/k_B T)$. The physical interpretation of this effective potential surface is quite obvious [23]: The classical system has been divided into P replicas of itself along the closed Feynman path where each replica is connected to its immediate neighbors via temperature dependent springs obeying Hook's law and experience a $1/P$ of the potential energy that a classical system at the same location would. Above the crossover temperature Eq. (1.27) the effective potential equals the classical potential as all the system replicas collapse to a single point in the N-dimensional coordinate space.

At low enough temperature, the effective potential V_{eff} will develop saddle points off the classical MEP which correspond to paths where thermally assisted tunneling is the

dominating mechanism, see Fig. (1.2). The crossover temperature, where tunneling starts to play a significant role, can be estimated from the curvature of the MEP at the classical saddle point. If ω is the magnitude of the imaginary vibrational frequency of the unstable mode at the saddle point, the crossover temperature is given by [6]

$$T_c = \frac{\hbar\omega}{2\pi k_B}. \tag{1.27}$$

In terms of the spring constants in the CFP this corresponds to temperature where the spring constants become to weak to overcome the curvature of the potential. The restoring force of the springs is not strong enough to keep the CFP collapsed at a single point, so the path opens up and spreads out towards the reactant and products, representing quantum mechanical delocalization and onset of thermally assisted tunneling.

1.5 Instanton theory, a harmonic quantum mechanical TST

In classical, harmonic transition state theory, where reaction rates can be estimated by expanding the potential energy surface around the classical saddle point in a second order Taylor polynomial. Applying the same analogy as before between the MEP and MAP then an approximate quantum mechanical rate can be obtained by expanding the Euclidian action around the instanton on the MAP to second order. The instanton rate constant, k_{inst} is given by [24]

$$Q^R \; k_{inst} = \sqrt{\frac{S_0}{2\pi\hbar}} \; \frac{1}{\Delta\tau |\prod_j' \lambda_j|} \; e^{-S_{ins}/\hbar}. \tag{1.28}$$

Here, S_{ins} is the value of the effective potential at the instanton, the λ_j are the frequencies of the normal modes of vibration of the chain at the instanton. If the system has NP dimensions then $NP-2$ frequency values will be real and positive. One will be purely imaginary corresponding to the unstable mode. The absolute sign around the the product in Eq. (1.28) is the result of the imaginary frequency, only the magnitude of the frequency is relevant. The last eigenvalue is zero and is not included in the product, the prime on the product sign denotes the absence of this 'zero-mode'. The mode with zero eigenvalue corresponds to moving the replicas along the CFP path (or, shifting the labels on the

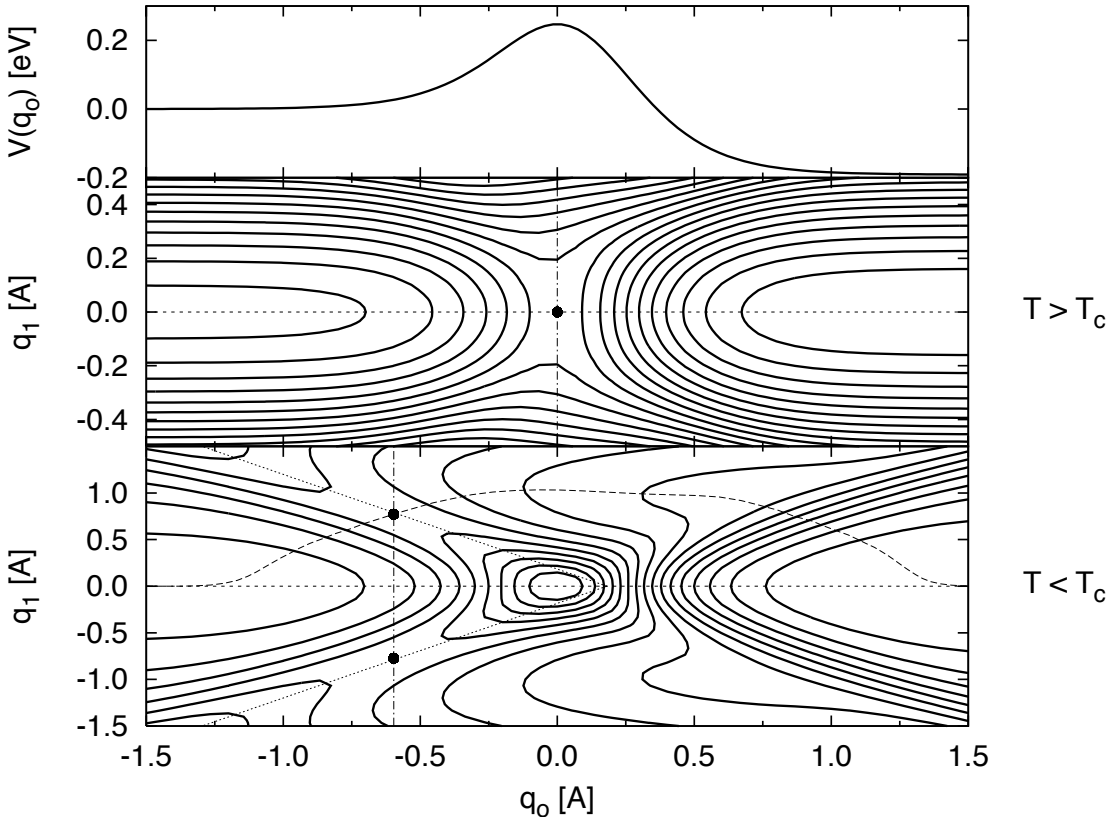

Figure 1.2: Figure is adopted from Ref.[9]. The top panel show a asymmetric Eckart barrier with the parameters used in Sec. (3.1). The middle panel show a contour plot of the effective potential, Eq. (2.1), where the CFP of the simple form $q(\tau) = q_o + q_1 \sin(2\pi\tau/\beta\hbar)$. The q_o coordinate represents the centroid of the CFP and the q_1 the extent, or delocalization of the CFP. When the temperature is higher than the crossover temperature, T_c, the CFP is collapsed at the centroid (q_o) coordinate. Any attempt to move of $q_1 = 0$, i.e. introducing quantum mechanical delocalization, results in a rise in the effective potential. The reaction coordinate is then the classical MEP, dotted horizontal line, and the CFP is located at the classical saddle point, black circle. The bottom panel depicts the situation when the temperature is lower than the crossover temperature. The CFP has now opened up and the system is delocalized. As described in the text, the effective potential has developed new saddle points that lie of the classical MEP. The new saddle points are the instantons. The instanton are the saddle points along a quantum mechanical reaction coordinate, the MAP, shown as a dashed line going through the instanton (black circle).

replicas) and is treated separately. Here,

$$S_0 = \frac{\mu P}{\beta\hbar}\sum_{j}^{P}(q_{\mathrm{mod}(k,P)+1} - q_j)^2 \tag{1.29}$$

and is twice the instanton action due to the (imaginary-time) kinetic energy.

1.5.1 HQTST rate

Once the saddle point on the effective potential energy surface has been located, the HQTST rate can be calculated according to Eq. (1.28). How to calculate Q^R on the left hand side is discussed in the Sec. (1.5.2). As Eq. (1.28) is written, only the vibrational part of the partition function is accounted for. For reactions taking place on a crystal surface, or inside the crystal bulk, where free translation and rotation are quenched, Eq. (1.28) is of the appropriate form. But when dealing with a gas phase reaction, the degrees of freedom corresponding to the three translational and three (assuming a nonlinear system) rotational degrees of freedom must be project out of the Hessian matrix when calculating the rate prefactor and substituted back in as independent approximations. Assuming separability of the various degrees of freedom, the total partition function can be approximated as a simple product of the electronic, translational, rotational and vibrational contributions. Since the Born-Oppenheimer approximation is employed the electronic contributions to the overall rate expression will cancel each other out and can be ignored. The translational part is given by the usual expression [12]

$$Q_{trans} = \left(\frac{Mk_BT}{2\pi\hbar^2}\right)^{3/2} V \tag{1.30}$$

with M and V as the total mass and volume of the system, respectively. Since the both the reactant partition function and the instanton partition function contribute the same amount to the translational partition function, the translational contribution is cancelled in the rate constant expression ($k \propto Q^{TS}/Q^R$) as well.

Here, it is implicitly assumed that the temperature is high enough that the rotation can always be considered to be purely classical. Care must to taken to validate this assumptions as the rate is calculated for extremely low temperature values. For the instanton, the

moments of inertia are approximated as the geometrical mean of the inertia moments of the individual system replicas along the CFP, as

$$Q_{rot}^{CFP} = \left(\left(\frac{2k_BT}{\hbar^2}\right)^3\pi\right)^{1/2}\exp\left\{\frac{k_BT}{\hbar}\int_0^{\hbar/k_BT}d\tau\log_e\left(\prod_i I_i^{CFP}(\tau)\right)^{1/2}\right\} \quad (1.31)$$

$$\approx \left(\left(\frac{2k_BT}{\hbar^2}\right)^3\pi\right)^{1/2}\exp\left\{\frac{1}{P}\sum_{k=1}^{P}\log_e\left(\prod_i I_i^{CFP}(\tau_k)\right)^{1/2}\right\} \quad (1.32)$$

An alternative route would be to assume the CFP to be one super-molecule and simply calculate the the moments of inertia assuming that each system replica one accounts for the $1/P$-th part of the total mass. The value of the rotational partition function must be multiplied on the right hand side of Eq. (1.28), at each temperature.

Finally, considering the vibrational partition functions, the CFP is evaluated as always by diagonalizing the instanton Hessian matrix and projecting out the zero modes. For a gas phase system there will be seven zero modes, 3 translational modes, 3 rotational modes (assuming a nonlinear molecule) and the mode corresponding to free rotation of the periodic orbit. The translational and rotational modes have already been accounted for and are ignored in the eigenvalue spectra of the Hessian matrix. The remaining mode is handled in the usual manner, see Eq. (1.29).

1.5.2 Calculating the reactant state partition function

The vibrational partition function for the reactant state is treated exactly alike as for the instanton. A CFP (discretized with the same number of system replicas) is formed that is collapsed in the reactant state. As a consequence all the Hessian blocks for individual system replicas in the CFP are identical and the Hessian matrix for the CFP can be factored into two parts, one is the Hessian block part with the individual replicas along the diagonal and the other is the spring constant contributions. The eigenvalues for the spring constant matrix are known analytically (each one is replicated $3N-6$ times, where N is the number of atoms)

$$\lambda_{sp}^{(k)} = 4\sin^2\left(\frac{\pi k}{P}\right) \quad , \quad k = 1, 2, \ldots, P. \quad (1.33)$$

By adding each one of the $\lambda_{sp}^{(k)}$ to the the reactant state vibrational modes, the entire CFP spectrum is obtained. So at the cost of a single diagonalization for one system replica, the vibrational modes of an arbitrarily sized (collapsed) CFP can be found. It is important to note that in the limit of infinite resolution of the CFP, the partition function for $3N-6$ independent harmonic oscillators is reclaimed,

$$\prod_{i=1}^{3N-6} \lim_{P\to\infty} \prod_{k=1}^{P} \left\{ 4\sin^2\left(\frac{\pi k}{P}\right) + (\Delta\tau)^2(\omega_i)^2 \right\} = \prod_{i=1}^{3N-6} \frac{1}{2\sinh(\hbar\omega/2k_BT)} = Q_{vib}^R(T). \quad (1.34)$$

The classical rotational partition function for an ideal polyatomic molecule is given by [12] (ignoring any symmetry numbers)

$$Q_{rot}^R = \left(\left(\frac{2k_BT}{\hbar^2}\right)^3 \pi \prod_i I_i^R \right)^{1/2}. \quad (1.35)$$

Here the I_i's are the principle moments of inertia (I_A, I_B and I_C) and are easily found as the eigenvalues of the moment of inertia tensor. For the reactant state, the translational partition function, Eq. (1.30) is handled identically as in the previous section.

Chapter 2

EFFICIENT IMPLEMENTATION OF INSTANTON THEORY

The present chapter describes an efficient implementation of instanton theory (harmonic quantum TST, HQTST), economical enough to be used in systems with tens or even hundreds of degrees of freedom and in combination with first principles evaluation of the atomic forces. Previously, calculations instantons by identifying periodic, classical orbits on the inverted potential energy surface [25, 26, 27]. While such an approach can be applied to systems with two or three degrees of freedom, extension to larger systems is difficult and the large number of force calculations required to evaluate the classical trajectories makes it impractical to apply such an approach in combination with first principles calculations of the atomic forces.

The implementation presented here relies on the fact that the instanton is a saddle point on the effective, quantum mechanical potential surface [27, 28]. There are several analogies between instanton theory and harmonic classical transition state theory. Just as the saddle point is the point of highest energy along a minimum energy path (MEP), the instanton is the configuration of a closed Feynman path (CFP) that represents the largest Euclidian action along a quantum mechanical reaction coordinate, the minimum action path (MAP) [9, 10, 29]. The well established techniques for locating saddle points on energy surfaces for systems with many degrees of freedom [30, 31, 32, 33, 34, 21] can, therefore, also be used to find instantons. The main difference in working with the quantum mechanical action surface as opposed to the classical potential energy surface is the large number of degrees of freedom. In going from the classical description to the quantum mechanical CFPs, the number of degrees of freedom increases by a factor of P, where P is the number of discrete system replicas used to represent the CFPs - typically between 10 and 100 for the systems of interest here. However, by applying robust methods for finding saddle points starting from a given initial configuration, the task of finding instantons turns out

to be tractable even for large systems, provided that a good initial guess for the instanton can be generated.

At low temperature where tunneling is the dominant transition mechanism, the transition path can deviate significantly from the MEP. Where the MEP is curved, the tunneling path will tend to 'cut the corner', i.e. be shorter at the expense of going through a higher energy region. It can, therefore, be hard to guess the shape of the CFP at the instanton [19]. The computational approach presented here assumes that one would like to calculate the transition rate at not just one particular value of the temperature, but rather over a whole range of temperatures that includes the crossover region, just below T_c. There, the replicas in the CFP at the instanton configuration are all close to the classical saddle point and spread only slightly away from it, mostly along the direction of the unstable mode. The rate constant calculations are, therefore, started at a temperature that is only slightly lower than T_c. A good initial guess for the instanton configuration can then be generated by distributing the system replicas in an initial CFP along the direction of the unstable mode, centered at the classical saddle point. After the instanton has been found at this first temperature value, the temperature is lowered, typically by 10 degrees or so, and the initial guess for the instanton configuration at the lowered temperature is taken to be the converged instanton from the previous, higher temperature calculation. From this study, we have found that the converged instanton CFP is always collapsed in such a way that pairs of system replicas within the CFP lie on top of each other. This can be used to cut the number of degrees of freedom in the instanton search in half, leading to large savings in the calculation both because of the reduction in the number of degrees of freedom and also because the convergence is more rapid. The generation of the initial configuration is described in the next section.

Once an initial guess of the instanton configuration has been obtained, the minimum mode algorithm [30, 31, 32] is used to iteratively change the CFP configuration to converge on the instanton. This is essentially the same algorithm as has been used in finding classical saddle points on potential energy surfaces, but it is reviewed here for completeness.

At the beginning of the calculation, the classical MEP and the saddle point on the potential energy surface are used to estimate the crossover temperature, T_c, in order to

choose the first value of the temperature for which the instanton is found. Necessarily, the number of system replicas in the CFPs is chosen to be as small as possible to reduce the computational effort. It turns out that the temperature at which the discrete CFPs begin to open up; the effective crossover temperature for a discrete CFP, is quite sensitive to the number of system replicas used in the calculation. The discretization causes a shift in the temperature scale, but the calculated value of the rate constant is otherwise not affected strongly. In the last section of this chapter, an analytical analysis of this shift in the effective crossover temperature with the number of system replicas in the CFPs is given. It can be used to get a better estimate of what temperature to start the calculation and to correct the results obtained from the numerical calculations.

The method described here to find instantons and evaluate quantum mechanical rate constants, within a harmonic approximation, has been implemented in the plane wave based density functional theory software called *Vienna Ab-initio Simulation Package* (VASP) [35, 36, 37, 38]. Typically a few hundred force evaluations are needed in the calculation per system replica to carry out the calculation at one value of the system temperature. In a cluster of computers where one or more CPU can be used for each of the system replicas, this does not represent a particularly large computational time. Application to several condensed phase systems is given in Chapter 4.

2.1 Numerical procedure

2.1.1 Initial guess for the instanton: collapsed pairs of replicas

In the early stages of the work presented here, initial guesses for the instanton configuration were constructed by generating system replicas forming a circle around the classical saddle point. Half of the system replicas were situated on the reactant side of the saddle point and the other half on the product side. This initial CFP was then converged to the instanton as described in Sec. (2.1.2). Empirically, it was noted that in the converged instanton, system replicas in the CFP had paired up, see Fig. (2.1) for an illustrative cartoon. Being superimposed in such a way in the classical space does not lead to an increase in the potential energy since the replicas only interact through the springs connecting adjacent replicas and

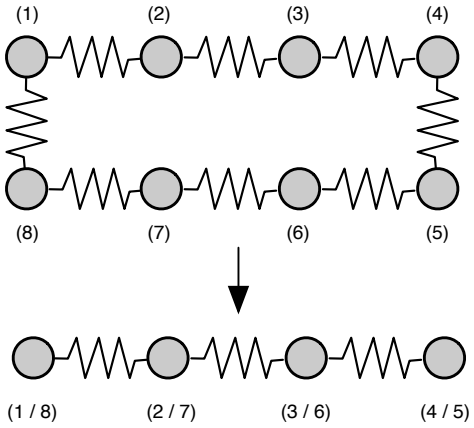

Figure 2.1: A schematic of a collapsed CFP. The upper portion displays a CFP with 8 system replicas. Each system replica is depicted as a single bead and the springs denote connections from each atom in the system to the same atoms in the neighboring replicas. The replicas are numbered in parenthesis above and below the individual beads. The lower half of the schematic shows the collapsed CFP. This is the preferred configuration of the CFP once converged to an instanton. Replicas have formed 'pairs' by exactly overlapping one another. It is important to note that there is no resulting increase in energy or forces since the replicas only feel each other through the springs.

not the potential energy term in Eq. (2.1). This pairing of the system replicas can be built in to the CFP right from the initial guess and throughout the calculation to reduce the computational effort. Half of the replicas are treated as 'shadows' of the other half. In practice, atomic forces are only calculated for half of the replicas, and these forces are then imposed onto the 'shadow' replicas. The result is about a 50% reduction in the force calculations necessary for each iteration in the calculation and faster convergence (i.e. fewer iteration steps). Tests showed that, for most temperatures, using only half of the replicas and forcing the other half to shadow produces the same results as allowing all the replicas to move freely. Since the springs become weaker as the temperature is decreased and the quantum delocalization increases, it is necessary to increase the number of system replicas as the temperature is lowered. In test cases where the number of replicas was not increased, the paring of the replicas at the converged result was sometimes not perfect. But, as the number of replicas was increased, the pairing occurred again. It was, therefore, concluded

that as long as the number of replicas was sufficient, pairing would take place.

Starting from the classical saddle point lying on the MEP connecting the reactant and product states, an initial CFP is formed by generating configurations of the system along the direction of the unstable mode as determined by the diagonalized Hessian matrix. The temperature is set slightly (typical ∼5 degrees) below the crossover temperature as estimated by Eq. (1.27). The extent of the CFP is usually chosen to be on the order of 0.1-0.2 Å in either direction away from the saddle point. The replicas are assumed to be paired. The initial, linear CFP along the unstable mode direction consists of half of the system replicas used in the calculation, the second half of the replicas are placed on top to create the collapsed pairs. As the temperature is lowered further, the converged instanton configuration from a previous, higher temperature is used as an initial guess for the instanton search.

2.1.2 Converging a CFP to the instanton

The object function to be maximized when locating the instanton is the Euclidian action, as given by Eq. (1.24). A simple rearrangement gives a more intuitive expression in terms of an *effective* potential energy function, facilitating a direct connection to the classical problem of locating a saddle point on a potential energy surface. Using a discrete representation of the Euclidian action, with P system replicas, results in

$$\begin{aligned} S_E(\mathbf{q}) &= \Delta\tau \sum_{k=1}^{P} \left[\frac{\mu}{2} \left| \frac{q_{\mathrm{mod}(k,P)+1} - q_k}{\Delta\tau} \right|^2 + V(q_k) \right] \\ &= \frac{\hbar}{k_B T} \sum_{k=1}^{P} \left[\frac{1}{2}\, k_{sp}(T) \left| q_{\mathrm{mod}(k,P)+1} - q_k \right|^2 + \frac{V(q_k)}{P} \right] \\ &= \frac{\hbar}{k_B T} V_{\mathrm{eff}}(\mathbf{q}, T), \end{aligned} \tag{2.1}$$

where the sum is defined as an effective potential energy surface, $V_{\mathrm{eff}}(\mathbf{q}, T)$, since it has units of energy. The 'mod(k,P)+1' subscript in Eq. (2.1) is necessary since the Feynman path is closed, so a system replica with coordinates q_P is connected to a system replica with coordinates q_1. According to Eq. (1.23), it is equivalent to weigh each closed path in the quantum partition function by $\exp(-S_E(\mathbf{q})/\hbar)$ or by $\exp(-V_{eff}(\mathbf{q}, T)/k_B T)$; maximizing the effective potential is equivalent to maximizing the Euclidian action. The problem is

now analogous to finding a saddle point on a potential energy surface, except that in the quantum mechanical case the potential energy surface depends on the system temperature. The physical interpretation of the effective potential surface is that the classical system, with N degrees of freedom, has been divided into P replicas along the CFP where each replica is connected to its immediate neighbors via temperature dependent springs obeying Hook's law. The replicas experience $1/P$ of the potential energy that a classical system at the same location would. Above the crossover temperature, Eq. (1.27), the effective potential equals the classical potential as all the system replicas collapse to a single point in the N-dimensional coordinate space.

In this work where the CFP is moved to converge to a instanton, a minimum mode method [30] is adapted. From a given starting configuration (the initial CFP), the lowest local curvature is found and the force acting on the system is projected along the lowest curvature direction. The system is subsequently moved along the lowest curvature direction in order to minimize the force projected along it. Once the lowest curvature becomes negative (i.e. the mode has become unstable), it is followed in a stepwise manner up to a first order saddle point.

Previously, the dimer [30] and Lanczos [39, 40] methods have been used with great success to locate saddle points. In a recent study [32], both methods were found to be nearly identical with regards to efficiency. In Ref. [30], the dimer method is used to find the direction of the lowest curvature. The dimer method uses two system replicas (a dimer), separated by a finite difference distance, to estimate the local curvature along the dimer. The torque acting on the dimer is used to align the dimer along the lowest curvature mode. In this study, the minimum mode Lanczos algorithm [40] is used instead of the dimer method as it leads to a simpler data structure: the dimension of the closed Feynman path (CFP) is NP but would be twice that if the dimer method were used as each system replica would then be a dimer. Even though applications of the Lanczos algorithm to minimum mode saddle point searches have been discussed in detail in Ref. [32], it will be reviewed here for completeness.

A real and symmetric matrix, such as the Hessian matrix, can be transformed through an orthogonal similarity transformation to a symmetric tridiagonal matrix. If the original

matrix is H then the relationship between the original matrix and the tridiagonal matrix is $T = W^t H W$, where the W matrix is orthonormal and the t superscript denotes a mathematical transpose. The two matrices, H and T, share the same eigenvalues, and the eigenvectors are trivially connected as well. If H has the eigenpairs $\{\lambda_i, z_i\}$, then T has the eigenpairs $\{\lambda_i, W^T z_i\}$.

Originally, the Lanczos algorithm was suggested as a procedure for performing a full tridiagonalization, but inherent numerical instabilities render it useless without costly remedies. The great virtue of the Lanczos algorithm is that by performing a partial reduction on the k-first columns, a sequence of tridiagonal matrices, T_2, $T_3, \ldots$, can be generated, each of much lower dimension than the original matrix and providing a progressively more refined estimate for the extrema eigenvalues of the original matrix [41]. The corresponding eigenvectors can be extracted through the similarity transformation relations, saving considerable time since a full diagonalization of a dense matrix represents a substantial computational barrier. The algorithm itself is remarkably simple: by using $T_k = W_k^t A W_k$ as $A W_k = W_k T_k$ suggests (by equating columns of $A W_k = W_k T_k$), an iteration scheme based on a three term recursion relation is developed:

$$A\mathbf{w}_k = \beta_{k-1}\mathbf{w}_{k-1} + \alpha_k \mathbf{w}_k + \beta_k \mathbf{w}_{k+1} \qquad , \qquad \beta_0 \mathbf{w}_0 = 0 \tag{2.2}$$

where the α's and β's are diagonal and sub/super diagonal elements of T and $\mathbf{w}_k$'s are normalized column vectors of W. Here, as before, boldfaced vectors represent all the coordinates of the CFP and the α's and β's are scalars. The matrix T is constructed as

$$T_n = \begin{bmatrix} \alpha_1 & \beta_1 & & & \\ \beta_1 & \alpha_2 & \beta_2 & & \\ & \beta_2 & \alpha_3 & \ddots & \\ & & \ddots & \ddots & \beta_{n-1} \\ & & & \beta_{n-1} & \alpha_n \end{bmatrix}$$

and at each step of the iteration a new line and column are added to the matrix. Beginning with an arbitrary nonzero starting vector $\mathbf{t}_0$ (or a converged eigenvector from a previous

step) and setting $\beta_0 = \left\|\mathbf{t}_0\right\|_2$ and $w_0 = 0$, the following steps are repeated ($k = 1, \ldots, n$) [42]

$$\begin{aligned}
\mathbf{w}_k &= \frac{\mathbf{t}_{k-1}}{\beta_{k-1}} \\
\mathbf{u}_k &= H\mathbf{w}_k \\
\mathbf{t}_k &= \mathbf{u}_k - \beta_{k-1}\mathbf{w}_{k-1} \\
\alpha_k &= \mathbf{w}_k^T\mathbf{t}_k \\
\mathbf{t}_k &= \mathbf{t}_k - \alpha_k\mathbf{w}_k \\
\beta_k &= \left\|\mathbf{t}_k\right\|_2.
\end{aligned}$$

To avoid having to set up the full Hessian matrix, the second step is replaced by the first order finite difference approximation

$$\mathbf{u}_k = -\frac{\mathbf{F}_k(\mathbf{q} + \delta q\mathbf{w}_k) - \mathbf{F}(\mathbf{q})}{\delta q}$$

where $\mathbf{q}$ is the coordinate of the system where the lowest curvature is to be estimated, $\mathbf{F}$ is the force (negative gradient of the effective potential) and δq is the finite difference step size and is uniform in length for each coordinate. At the end of each step, the matrix T_k is diagonalized using a standard LAPACK[1] routine and the convergence of the lowest (not smallest) eigenvalue, here called $C_{(k)}$, is monitored. If

$$\left|\frac{C_{(k)} - C_{(k-1)}}{C_{(k-1)}}\right| < \text{tol} \qquad , \tag{2.3}$$

then the eigenvalue is considered to have been located. Criteria (tol in Eq. (2.3)) of the order 10^{-2}-10^{-4} works well for most cases.

With the lowest eigenvalue, $C_{(k)}$, (the lowest curvature on the effective potential energy surface) converged, the corresponding eigenvector can be found by an inverse iteration scheme. First the entire eigenvalue spectra for the tridiagonal Lanczos matrix, T, is shifted such that it becomes positive definite, i.e. all the eigenvalues are larger than zero. Further, to ensure rapid convergence for the inverse iteration, the lowest eigenvalue is set to a small positive number. Experience has shown 10^{-4} to work quite well. With the Lanczos matrix

[1]DSTEV, available at http://www.netlib.org/lapack or as a canned routine from most processor vendors

now fixed to be positive definite, Cholesky factorization can be applied in the inverse iteration scheme instead of LU factorization. Since the matrix is also tridiagonal and symmetric, the Cholesky factorization scales as $8k$. A convergence to the eigenvector is usually found in about 3 iterations. Once the eigenvector has been found, the lowest curvature mode ($\vec{N}$) can be obtained through the similarity relation between T_k and H. Here no reorthogonalization is performed to overcome the numerical instabilities; it is explicitly assumed that convergence is reached before any instability issues become important. No case has been encountered so far that gives any indication to distrust this assumption.

After the lowest curvature mode has been found the system is moved along an effective force ($\vec{F}_{eff}$) determined by the sign of the curvature [32, 30]

$$\vec{F}_{eff} = \begin{cases} -\left(\vec{F}\cdot\vec{N}\right)\vec{N} & \text{if } C > 0 \\ \vec{F} - 2\left(\vec{F}\cdot\vec{N}\right)\vec{N} & \text{if } C < 0 \end{cases} \tag{2.4}$$

Here $\vec{F}$ are the actual forces on the system. This is to ensure a rapid exit from the convex regions ($C > 0$) around the potential energy minimum. It has been shown that this choice of an effective force leads to fast convergence to a saddle point. F_{eff} can be minimized with any effective minimization procedure. Here, a conjugate gradient method with a force based line search is used. The step size is determined solely on the forces since after projecting the 'true' force according to Eq. (2.4), there is no longer correspondence between the effective force and the energy. So the gradient of the energy is not necessarily the effective force [30, 32].

Once the CFP has been converged to an instanton, $\mathbf{q}_{\text{ins}}$, the action (or $V_{\text{eff}}(\mathbf{q}, T)$) is expanded to second order around $\mathbf{q}_{\text{ins}}$,

$$\begin{aligned} S_E(\mathbf{q}) &\approx S_{\text{ins}} + \nabla^T S_{\text{ins}} \cdot (\mathbf{q} - \mathbf{q}_{\text{ins}}) + \frac{1}{2}(\mathbf{q} - \mathbf{q}_{\text{ins}})^T \cdot \left(\nabla\nabla^T S_{\text{ins}}\right) \cdot (\mathbf{q} - \mathbf{q}_{\text{ins}}) \quad (2.5) \\ &= S_{\text{ins}} + \frac{1}{2}(\mathbf{q} - \mathbf{q}_{\text{ins}})^T \cdot \left(\nabla\nabla^T S_{\text{ins}}\right) \cdot (\mathbf{q} - \mathbf{q}_{\text{ins}}). \quad (2.6) \end{aligned}$$

The first order term is dropped because the instanton is a local maximum with a zero derivative. S_{ins} is the action at the instanton. The matrix of second derivatives of the action ($\nabla\nabla^T S_{\text{ins}}$) needs to be set up and diagonalized. Carrying out the differentiation

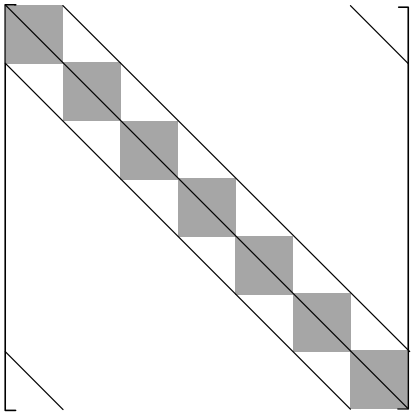

Figure 2.2: Structure of the HQTST prefactor matrix. Along the block diagonal are the matrix of second derivatives of the true potential in mass-scaled coordinates for each system replica (here P = 7), multiplied by $(\Delta\tau)^2$ ($\Delta\tau$ is the imaginary time step). The contribution from the temperature dependent spring constants through interactions with the nearest neighbor replicas lie on the main diagonal (+2) and the super/sub-diagonals (-1). Since the CFP is a closed path, there are contributions to the top right corner and the bottom left corner of the matrix, representing the spring connections from the first replica to the last.

results in

$$K(\mathbf{q}) = (\Delta\tau)^2 \left\{ \frac{\partial^2 V(q_i)}{(m_k m_l)^{1/2}\, \partial q_{i,k} \partial q_{i,l}} - \frac{\partial}{\partial \tau^2} \right\} \tag{2.7}$$

Here q_i are the coordinates of the i-th system replica, $q_{i,k}$ and $q_{i,l}$ are the k and l coordinate components for the i-th replica and m_k, m_l are the corresponding masses of the coordinates. Fig. (2.2) shows the general structure of the matrix. On the block diagonal are the Hessian matrices in mass-scaled coordinates for each system replica. The spring constant $(-(\Delta\tau)^2\partial/\partial\tau^2)$ contributions, resulting from each replica being connected to the nearest neighbors along the CFP, are on the main diagonal and the super- and subdiagonals as depicted in Fig. (2.2). The spring constants add +2 to the main diagonal and -1 to the super- and subdiagonals. The matrix will be become more and more sparse as the number of system replicas grows. With use of an effective method that exploits the spareness and symmetric structure, there can be considerable computational savings with the diagonalization. Robust methods exist to perform a full diagonalization on large symmetric matrices using only matrix-vector multiplication. Because of the relatively low number of

dimensions used here (the matrix size is usually around 500x500), the efficiency is not of the highest importance but should be kept in mind when systems of higher dimensionality are studied. Usually it takes more computational effort to converge to the instanton than to set up and solve the eigenvalue problem. In this study only a standard diagonalization scheme, assuming a dense matrix, has been employed.

Diagonalization of Eq. (2.7) provides the vibration spectrum necessary for calculating the rate constant according to Eq. (1.28). Arranging the eigenvalues of $K(\mathbf{q})$ in ascending order with λ_i^2 , $i = 1, 2, \ldots, NP$, where N is the number of degrees of freedom, and P the number of system replicas in the CFP. If the CFP has been converged properly to an instanton, then $\lambda_1^2 < 0$, $\lambda_2^2 = 0$ and all other λ_i's are positive. The negative λ values corresponds to the unstable reactive direction and the zero valued λ is related to free rotation of the replicas around the CFP (Eq. (1.29)). Only the nonzero eigenvalues are used in calculating the rate constant in Eq. (1.28). Any translational or rotational motion will introduce auxiliary zero eigenvalues into Eq. (2.7) and must be eliminated from the product of eigenvalues in Eq. (1.28).

2.2 Correction to the crossover temperature obtained from discrete Feynman paths

This section presents an analysis that can be used to estimate how much the crossover temperature is affected by the finite number of system replicas in the CFPs. In the limit of an infinite number of replicas, the WKB [16, 17, 18] estimate given by Gillan is obtained. But the fact that a finite number of system replicas is used in practical calculations means that the crossover temperature, and the temperature scale, is shifted. Consider the situation depicted in Fig. (2.3). The figure describes an instanton around a potential barrier at a temperature slightly lower than the crossover temperature. The instanton is comprised of 8 system replicas, but pairs have collapsed, creating the appearance of only 4 system replicas. Each replica is at a force equilibrium, i.e. the potential force dragging it downwards is exactly opposed by the neighboring spring forces. It is further assumed that the replicas are displaced only by an infinitesimal distance from the potential barrier so the force acting on them can be well described with a second order Taylor expansion from the top of the

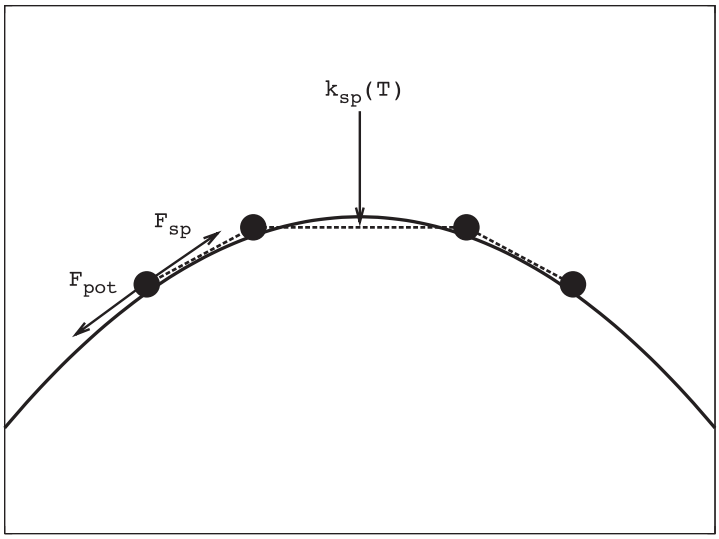

Figure 2.3: An instanton at static equilibrium on a parabolic potential. The temperature is assumed to be just under the crossover temperature, Eq. (1.27), so the instanton has started to spread out. The springs connecting the system replicas with temperature dependent spring constants, $k_{sp}(T)$, are shown as dotted lines. Acting on each replica are the force from the potential (F_{pot}) dragging the replicas downward and the restoring force from the springs, F_{sp}, acting to collapse the instanton. The Feynman path integral is resolved using 8 system replicas but, at the static equilibrium, replicas collapse into pairs so only four are visible. By considering the forces at equilibrium the coordinates for each of the system replicas can be determined.

barrier and that the springs obey Hook's law. Noting the location of the replica furthest to the right in Fig. (2.3) as q_2, the next neighbor as q_1 and the barrier top as q_0, the following system of equations arises by considering the balanced forces

$$\begin{aligned} -V''(q_0)(q_2 - q_0)/P + k_{sp}(T)(q_1 - q_2) &= 0 \\ -V''(q_0)(q_1 - q_0)/P + k_{sp}(T)(q_2 - q_1) - 2k(q_1 - q_0) &= 0, \end{aligned} \tag{2.8}$$

where $V''(q_0)$ is the curvature at the barrier top, P is the number of replicas and k_{sp} is the spring constant between the replicas (Eq. (1.25)). The P comes from the effective force, Eq. (2.1), where the potential energy experienced by each replica is scaled by the total number of replicas in the CFP. Arranging the above set of equations into a more convenient

matrix form,

$$\begin{bmatrix} -(s-1) & 1 \\ 1 & -(s+1) \end{bmatrix} \begin{bmatrix} q_2 - q_0 \\ q_1 - q_0 \end{bmatrix} = \begin{bmatrix} 0 \\ 0 \end{bmatrix} \tag{2.9}$$

using

$$s = \frac{V''(q_0)}{k_{sp}(T)P} + 2 \tag{2.10}$$

The non-trivial solutions (the trivial being $q_2 = q_0$ and $q_1 = q_0$, representing a collapsed CFP) are found by insisting the determinant of the matrix be zero:

$$\det\left(\begin{bmatrix} -(s-1) & 1 \\ 1 & -(s+1) \end{bmatrix}\right) = 0. \tag{2.11}$$

The solutions to Eq. (2.11) are $\pm\sqrt{2}$. Inserting the solution with the highest numerical value (maximizes the effective potential) back into Eq. (2.10) and using the definition for $k_{sp}(T)$ and the fact that $V''(q_0) = -\mu\omega^2$ (ω is the *magnitude* of the imaginary barrier frequency) gives

$$\begin{aligned} 2 - s_{\max} &= \frac{\mu\omega^2}{\mu P^2 \left(k_B T_P/\hbar\right)^2} \\ &= \left(\frac{\hbar\omega}{P k_B T_P}\right)^2. \end{aligned} \tag{2.12}$$

Isolating T_P from the above expression yields the temperature value where the chain has just started to spread, i.e. the onset of quantum effects. With the number of replicas, P, equal to 8 (8 is used for illustrative purposes)

$$T_P = \frac{\hbar\omega}{P\sqrt{2 - s_{\max}} k_B} = \frac{\hbar\omega}{8\ \sqrt{2-\sqrt{2}}\ \ k_B} \simeq \frac{\hbar\omega}{6.122\ k_B} \tag{2.13}$$

This is the same general equation for the crossover temperature as derived by Gillan using WKB theory [6] (see. Eq. (1.27)), differing only by a numerical constant.

By using an arbitrary number of replicas in the analysis above, a general formula is easily derived. Considering the static force equilibrium on a chain with the number of replicas as

$P = 2^{j+2}$, the determinant is

$$\underbrace{\begin{vmatrix} -(s-1) & 1 & & & & & \\ 1 & -s & 1 & & & & \\ & 1 & -s & 1 & & & \\ & & \ddots & \ddots & \ddots & & \\ & & & 1 & -s & 1 & \\ & & & & 1 & -(s+1) \end{vmatrix}}_{2^j} = 0. \tag{2.14}$$

The solutions are

$$s_j \;=\; \underbrace{\pm\sqrt{2 \pm \sqrt{2 \pm \sqrt{2 \pm \cdots \pm \sqrt{2}}}}}_{j-terms}. \tag{2.15}$$

Inserting the solution with the greatest magnitude, s_{max}, back into Eq. (2.12) gives

$$\begin{aligned} 2 - \underbrace{\sqrt{2 + \sqrt{2 + \sqrt{2 + \cdots + \sqrt{2}}}}}_{j-terms} &= \left(\frac{\hbar\omega}{P k_B T_P}\right)^2 \\ &= \left(\frac{\hbar\omega}{2^{j+2} k_B T_P}\right)^2. \end{aligned}$$

By considering the ratio of the predicted crossover temperature as a function of the number of system replicas, T_P, to the Gillan estimate, Eq. (1.27) of the crossover temperature results in

$$\frac{T_P}{T_c} = \frac{\pi}{2^{j+1}\sqrt{2 - \underbrace{\sqrt{2 + \sqrt{2 + \sqrt{2 + \cdots + \sqrt{2}}}}}_{j-terms}}}. \tag{2.16}$$

The series $\{\sqrt{2 + \sqrt{2 + \sqrt{2 + \cdots + \sqrt{2}}}}\}$ is a well know *nested radical* and converges in the limit of infinite j ,

$$\lim_{j\to\infty} \underbrace{\sqrt{2 + \sqrt{2 + \sqrt{2 + \cdots + \sqrt{2}}}}}_{j-terms} \;=\; 2 \tag{2.17}$$

Table 2.1: Convergence of the crossover temperature predicted from instanton rate theory to the crossover temperature predicted by Gillan [6] from WKB theory. P is the number of replicas in the discrete formulation of Feynman's path integral, s_j is the maximum solution of Eq. (2.14) and T_p/T_c is the ratio given by Eq. (2.16).

j	P	s_max	T_P/T_c
0	4	0.000000	1.1107207
1	8	1.414214	1.0261722
2	16	1.847759	1.0064545
3	32	1.961571	1.0016082
4	64	1.990369	1.0004017
5	128	1.997591	1.0001004
6	256	1.999398	1.0000251
7	512	1.999849	1.0000063
8	1024	1.999962	1.0000016
9	2048	1.999991	1.0000004
10	4096	1.999998	1.0000001

and $2^{j+1}\sqrt{2-\sqrt{2+\sqrt{2+\sqrt{2+\cdots+\sqrt{2}}}}}$ is among the numerous series that converged to π in the limit of infinite j,

$$\lim_{j\to\infty} 2^{j+1}\sqrt{2-\underbrace{\sqrt{2+\sqrt{2+\sqrt{2+\cdots+\sqrt{2}}}}}_{j-terms}} \;=\; \pi. \tag{2.18}$$

In the limit of infinite system replicas, where the discrete representation of the CFP becomes continuous, Gillan's equation for the crossover temperature is retrieved as (with $P = 2^{j+2}$)

$$\lim_{j\to\infty} \frac{T_P}{T_c} = \frac{\pi}{\pi} = 1. \tag{2.19}$$

Chapter 3

TEST CASES USING ANALYTICAL POTENTIAL ENERGY FUNCTIONS

The computational procedure for locating instantons and evaluating the corresponding rate constants is tested by applying it to various problems, which range from a single coordinate to a system with hundreds of degrees of freedom. Potential functions simple enough to allow closed form solution for the rate constant for comparison, to semi-complex multi-component, many-body empirical potentials are used. Results are compared to previously published results where possible.

3.1 Asymmetric Eckart barrier

As a simple test problem, consider the asymmetric Eckart potential barrier [43, 44]. The barrier has a simple one dimensional form that allows for an analytical solution of Schrödinger's equation. The potential function is given by

$$\begin{aligned} V(x) &= \frac{V_A\, y}{1+y} + \frac{V_B\, y}{(1+y)^2} \qquad \text{, where} \\ y &= \left(\frac{V_B + V_A}{V_B - V_A}\right) e^{\alpha x}. \end{aligned} \tag{3.1}$$

When $x \to -\infty$, $V(x)$ tends to 0 and when $x \to \infty$ to V_A. V_A sets the asymmetry of the barrier. The potential describes a gas phase collinear exchange reaction, and the parameters are chosen to be he same as in Ref. [24] for the larger of the two asymmetries used there, $V_A = -0.191$ eV, $V_B = 1.343$ eV, $\alpha = 5.726$ Å and $m = 1.008$ amu, resulting in a reaction barrier height with respect to $V(x \to -\infty)$ of $V_{max} = V(0) = 0.247$ eV and an imaginary angular frequency at the barrier top with magnitude 7531.3 cm^{-1}. According to Gillan's equation, Eq. (1.27), the corresponding crossover temperature is $T_c = 273.4$ K. A graphical representation of the barrier is given in Fig. (3.1). The analytical reactive flux, $Q^R k$, can

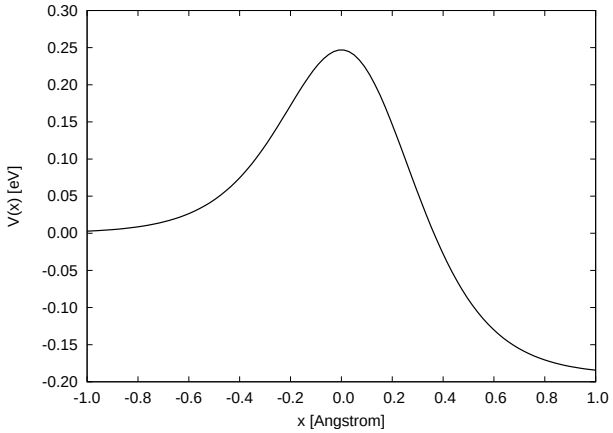

Figure 3.1: The asymmetric Eckart barrier with parameters from Ref. [24].

be calculated by [24]

$$Q^R k_{\text{exact}} = \frac{1}{2\pi\hbar}\int_0^\infty \mathrm{d}E\, P(E)\exp(-\beta E), \tag{3.2}$$

where $\beta = 1/k_B T$, $Q^R k$ is the reactant state partition function, $P(E)$ is the barrier transmission probability and is calculated according to

$$P(E) = \frac{\cosh(a+b)+\cosh(a-b)}{\cosh(a+b)+\cosh(d)} \tag{3.3}$$

where

$$a = \frac{2\pi\sqrt{2mE}}{\hbar\alpha}, \tag{3.4}$$

$$b = \frac{2\pi\sqrt{2m(E-V_A)}}{\hbar\alpha}, \tag{3.5}$$

$$d = \frac{2\pi\sqrt{2m\left(\sqrt{V_{\max}}+\sqrt{V_{\max}-V_A}\right)^2-\left(\frac{\hbar\alpha}{2}\right)^2}}{\hbar\alpha}. \tag{3.6}$$

According to classical HTST the reactive flux is simply

$$\begin{aligned} Q^R k_{\text{HTST}} &= \frac{1}{2\pi\hbar}\int_0^\infty \mathrm{d}E\, P(E)\exp(-\beta E) \\ &= \frac{1}{2\pi\hbar}\int_{V_{\max}}^\infty \mathrm{d}E\exp(-\beta E) = \frac{1}{2\pi\hbar\beta}\exp\left(-\beta V_{\max}\right). \end{aligned} \tag{3.7}$$

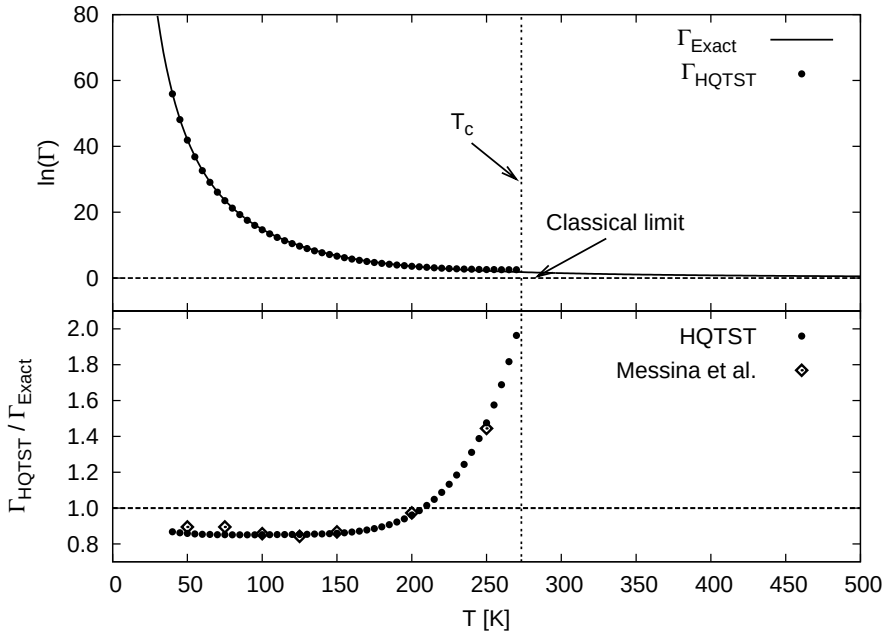

Figure 3.2: Comparison between the analytical quantum correction factor and the correction factor obtained from instanton calculations (HQTST) for the asymmetric Eckart barrier. The top half shows the natural logarithm values while the bottom half plots the ratio of the absolute magnitudes. The HQTST results overestimate the correction factor close to the crossover temperature, as expected. The ratio levels of where the HQTST rate underestimates the true rate about 20%. The open diamonds in the lower panel are previously published results from Messina et al., Ref. [24]. The dotted, vertical line represents the crossover temperature, T_c, calculated to be 273.4 K.

The purely classical transmission probability is a simple step function. If the energy is below the activation barrier, $V_{\max}$, the transmission probability is zero, andif the energy is higher than the barrier, the transmission probability is one. Finally, the reactive flux can be calculated from the instanton as prescribed by Eq. (1.28).

By calculating the the quantum correction factor ($\Gamma(T)$), i.e. the ratio of the quantum mechanical reaction rate to the classical HTST rate, the instanton method can be compared to the analytical solution. Fig. (3.2) displays the comparison between Γ_{HQTST} and Γ_{exact}. A comparison between the two different values at each temperature can be used as a gauge of the precision that can be expected from instanton calculations. The top half of Fig. (3.2) shows how the instanton fairs against the analytical solution on a logarithmic scale. Since

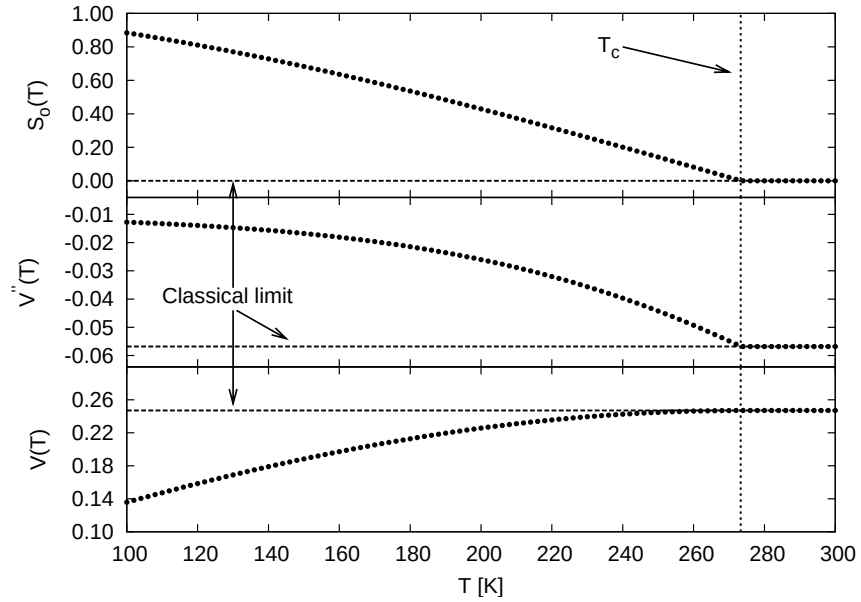

Figure 3.3: The dependence of various instanton gauges on temperature. The top panel shows S_0, the imaginary time kinetic energy, Eq. (1.29), as a function of temperature. Above the crossover temperature, all the system replicas that represent the closed Feynman path (CFP) collapse at the classical saddle point. Below the crossover temperature the path spreads out and kinetic energy rises. The middle panel shows the value of the frequency of the unstable mode as a function of temperature. Above the crossover temperature the instanton is collapsed at the classical saddle point. As the instanton spreads out the curvature tends to zero as the activation barrier becomes effectively smaller and smaller due to tunneling. The value of the curvature is then the classical value, divided by the number of images in the closed Feynman path. The bottom panel shows the value of the instanton on the effective potential surface Eq. (2.1). As before the instanton is collapsed to the classical saddle point (0.247 eV) above the crossover temperature. Below the crossover temperature the instanton spreads out and the instanton energy decreases, indicating a decreased activation energy due to onset of tunneling. The vertical dotted line marks the crossover temperature, $T_c = 273.4$ K, Eq. (1.27). 100 system replicas were used in the discrete representation of the Feynman path integral.

this perspective tends to skew any real comparison by diminishing any difference, a closer (and more honest) comparison is made in the lower half of the figure where the ratio of the absolute magnitudes is plotted as a function of temperature. As previously shown [9], the instanton severely overestimates the quantum rate and correction factor very close to the crossover temperature. However, over most of the temperature range in this study,

the instanton results underestimate the analytical solution by about 20%. The instanton calculations from Ref. [24] are superposed on the lower half of the figure for comparison. Since the results from Ref. [24] are only reported with two significant digits, the data look a bit more jagged on the scale used here.

Once the temperature is below the crossover temperature, the springs are no longer sufficiently stiff to maintain the CFP collapsed at the the classical image, and the path opens up. This is interpreted as quantum delocalization of the system and the onset of thermally assisted tunneling as a competing mechanism to the classical, over the barrier mechanism. It can be illuminating to study the behavior of some of the characteristic variables for the instanton under the influence of varying temperature. The top panel of Fig. (3.3) shows the "free instanton action", the middle panel is the curvature of the effective potential and the bottom panel is the instanton energy. Above the crossover temperature (labeled T_c in the figure) all the values are collapsed to their classical limits, i.e. the S_o is zero since all the images are collapsed at the classical saddle point. For the same reason, the energy is the classical barrier energy and the curvature is the classical barrier curvature, divided by the number of images in the chain. In fact, S_o offers an effective gauge for determining when the crossover temperature is reached as it is extremely sensitive to the length of the CFP. As soon as the temperature dips below T_c, S_o rises abruptly. This property can be used to identify precisely the crossover temperature for a discrete representation of the CFP, for direct comparison with results from Gillan's formula, Eq. (1.27).

As a further check on the implementation presented here, the location of the instanton centroid is calculated as

$$q_{\text{centroid}} = \frac{1}{\beta\hbar}\int_0^{\beta\hbar} q(\tau)d\tau \approx \frac{1}{P}\sum_{k=1}^{P} q_k \tag{3.8}$$

and compared to results previously published by Messina et al. [24] using the same potential. As presented in Fig. (3.4), the comparison is satisfactory. The instanton centroid slides down to the left hand side of the potential as the temperature is reduced. Since the potential is asymmetric around the barrier and steeper on the right hand side than the left hand side, system replicas on the right hand side will extend further from the barrier top. More system replicas are then needed on the left hand side to reach force equilibrium, hence the centroid

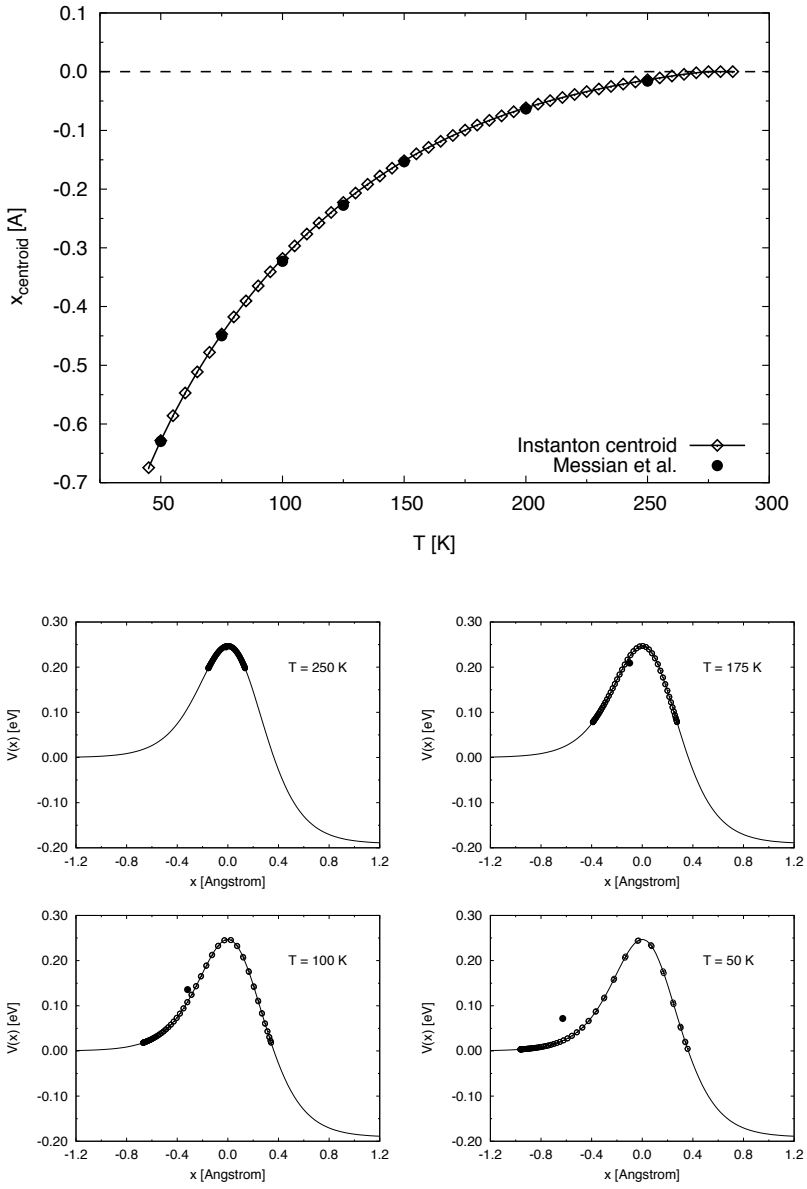

Figure 3.4: Centroid coordinate for the instanton as a function of temperature on the asymmetric Eckart potential. The topmost figure shows the instanton centroid coordinate as it varies with temperature. The lower figures show snapshots at 250 K, 175 K, 100 K and 50 K. The solid dot is the centroid coordinate. On the high temperature end all the images are collapsed to a single point. As the temperature is lowered the images spread out along the reaction coordinate, lowering the activation energy, indicating onset of quantum mechanical delocalization and thermally assisted tunneling. For comparison, results from Messina et al., Ref. [24], are in excellent agreement with the current study.

migrates towards the left as the temperature is decreased. Any attempt to estimate the rate by constraining the CFP centroid to the top of the barrier will not work if the barrier is not symmetric [7].

3.2 Symmetric Eckart potential coupled to a harmonic oscillator

Following McRae et al. [45], a two dimensional system is studied where a symmetric Eckart barrier [43] is coupled linearly to a harmonic oscillator. The initial motivation for constructing a model potential of this type was to study a reaction in solution, i.e. a single "solute" coordinate (represented by the Eckart barrier) coupled to a "solvent" (represented by a set of harmonic oscillators). Varying the friction (related to the harmonic oscillator frequency) between the solute coordinate and the the solvent, McRae et al. [45] compare the results at two different temperatures for two different approximations: variational transition state theory with semi-classical tunneling corrections and a centroid density method. Unfortunately, both the temperature values McRae et al. are above the classical to quantum crossover temperature. The results presented in Ref. [45] indicate that both approximate methods yield results comparable to the exact quantum reaction rate for both high and medium friction but deviate somewhat at lower frictions. Here, the low frequency regime has been especially targeted as a test for the HQTST method.

Based on the results in Ref. [45], a single solvent coordinate is adequate in describing the solvent effect on the solute coordinate, and hence only one harmonic oscillator is used here. This reduces the potential energy function to a simple form,

$$V(x,z) = V_o \, \mathrm{sech}^2(\alpha x/2) + \frac{1}{2}\mu\omega^2(z - Cx)^2 \quad , \tag{3.9}$$

here x is the solvent coordinate, z is the oscillator coordinate and the parameters V_o, α, μ and ω are chosen to reproduce the H+H_2 gas-phase reaction. The coupling constant, C, is meant to mimic the linear response of a Gaussian friction kernel and is calculated by

$$C = \frac{4f\omega_x}{\pi\omega} e^{-\pi^2/32} \quad , \tag{3.10}$$

ω_x is the magnitude of the imaginary angular frequency at the top of the the Eckart barrier, ω is the angular frequency of the harmonic oscillator and is chosen to be related to the

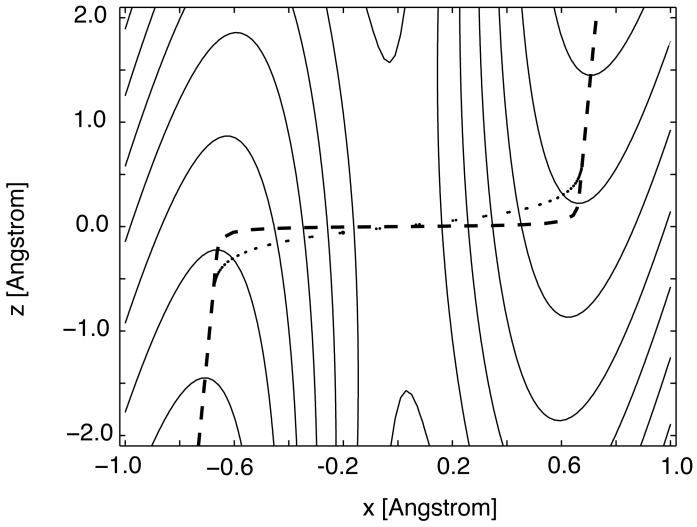

Figure 3.5: Corner cutting effect at 40 K for the symmetric Eckart potential, linearly coupled to a harmonic oscillator. The classical MEP and the instanton are represented by the dashed line and dots, respectively. The Feynman path at the instanton is approximated with 100 discrete system replicas.

characteristic timescale, σ, of the friction kernel through $\omega = \pi/(4\sigma)$. Finally, f is dimensionless friction parameter. The potential parameters chosen are $V_o = 0.425$ eV, $\alpha = 3.97$ Å, $\mu = 0.672$ amu, $\omega_x = 2.232\ \tau^{-1}$, $\omega = 0.0921\ \tau^{-1}$ and $C = 10.0$ ($f \approx 4.4$). The base units for energy, length, mass and temperature are eV, Å, amu and K as respectively; the corresponding time unit is $1\ \tau = 10.18$ fs. For more on the friction and how Eq. (3.10) is deduced, refer back to McRae et al. [45]. A contour plot of the potential, along with the classical MEP is shown in Fig. (3.5). The sharp turn in the classical MEP path results in a considerable corner cutting effect at lower temperatures, as is evident in Fig. (3.5). In Fig. (3.6) the reactive flux (i.e. $\log_e(Q^R k)$) from two different methods is compared to the HQTST flux. A discrete representation of the Feynman path integral is used with 100 system replicas in the chain. The first method, here referred to as 'Exact', sets up a discrete version of the system Hamiltonian on a grid and solves the corresponding eigenvalue problem for the state energies and wavefunctions. These are then used to calculate Miller's reactive flux

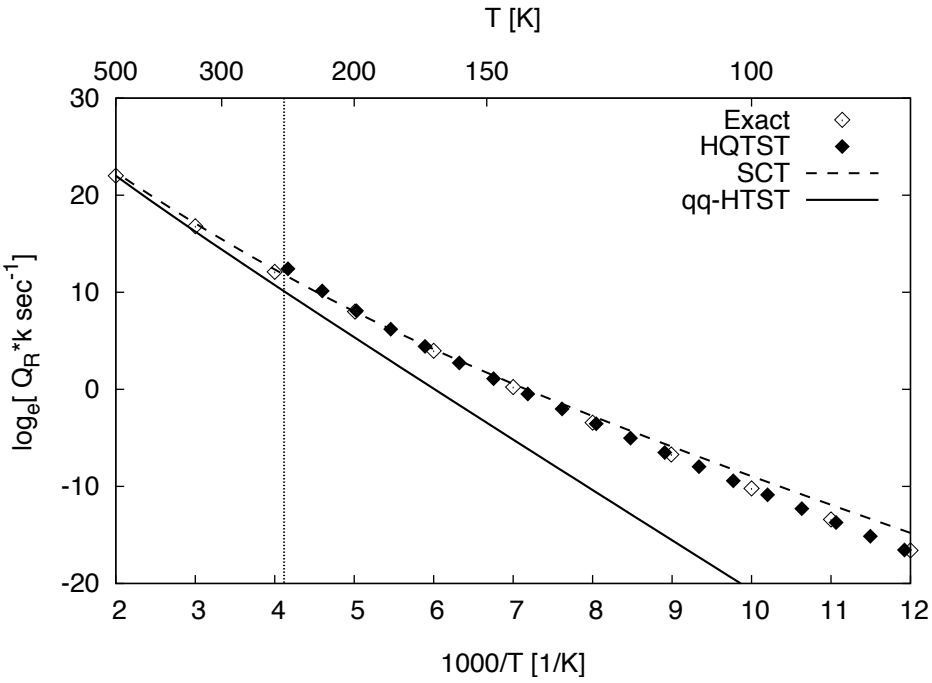

Figure 3.6: Reactive flux for the symmetric Eckart barrier, linearly coupled to a harmonic oscillator. HQTST results are compared exact quantum mechanical solution and results based on the small curvature tunneling (SCT) approximation to the classical rate. Excellent agreement is found between the exact reactive flux and the HQTST flux. Above the crossover temperature, the SCT approximation agrees favorably with the exact solution, but starts to deviate at lower temperatures, as expected. The HQTST results are obtained by using 100 discrete system replicas in the Feynman paths. The classical to quantum crossover temperature is 242.9 K.

correlation function [46]. The second method compared to is a small curvature tunneling (SCT) correction [14, 13, 47] to the classical (quasi-quantum) rate. It is expected to be reliable over a wide temperature range and more accurate at higher temperatures. The SCT accounts for the tunneling probability by expanding the potential in a Taylor series up to the quadratic term and finds the optimal tunneling path, including corner cutting. The tunneling probability is then represented by a multiplicative term in the classical reaction rate. As is evident in Fig. (3.6), there is an excellent correspondence between the HQTST reactive flux and the the "exact" solution. As expected, the SCT approximation yields good results at the higher temperatures but starts to deviate as the temperature is decreased.

3.3 Electron scattered by embedded Gaussian peaks in a two dimensional parabolic potential

Gudmundsson et al. [48, 49, 50] have performed numerical as well as theoretical studies of electron conductance through a quantum nanowire with embedded impurities (both attractive and repulsive) of a finite extent. Cases both with or without external homogenous magnetic field have been considered. Here, efforts will be concentrated on the case of repulsive impurities in the presence of a zero magnetic field. The model potential is adopted from Gudmundsson et al. and is composed of two independent components. The wire is described to be of infinite length but parabolically confined along the transverse direction, and the scattering potential is chosen to be one or more Gaussians. The potential parameters are chosen to mimic the GaAs semi-conductor system as much as possible, resulting for the parabolic confinement in

$$V_{par}(x) = \frac{1}{2} m\omega^2 x^2 \tag{3.11}$$

with $m = 6.10 \cdot 10^{-32}$ kg ($0.067\ m_e$), the effective mass of a electron in the GaAs system and $\omega = 3.04 \cdot 10^{12}$ s^{-1} so that the energy spacing between levels for the parabolic confinement potential is $E_o = 2.0$ meV. The scattering potentials have the form

$$V_{scatt}(x,z) = \sum_{i=1}^{N} V_i \; e^{-\beta_i^2 \; ((x-x_i)^2+(z-z_i)^2)}. \tag{3.12}$$

Three different cases are studied here. The first case is a single Gaussian barrier situated at the center of the wire ($N = 1$, $V_1 = 4.0$ meV, $\beta_1 = 0.012247$ nm, and $x_1 = z_1 = 0.0$), the second case is two Gaussian barriers symmetrically offset around the center with the same barrier height ($N = 2$, $V_1 = V_2 = 4.0$ meV, $\beta_1 = \beta_2 = 0.031623$ nm, and $x_1 = z_1 = -x_2 = -z_2 = 20.0$ nm). The final case is two Gaussian barriers situated along the axis of the parabolic confinement potential, with $N = 2$, $V_1 = V_2 = 4.0$ meV, $\beta_1 = \beta_2 = 0.12247$ nm, and $x_1 = z_1 = -x_2 = -z_2 = 85.0$ nm. When the distance between the barriers is such that no potential from the neighbors on either side is felt, the total rate constant will be given by a simple multiplication of all the independent rate constants. As the barriers are brought closer together, stronger resonance effects, which are not included in the instanton

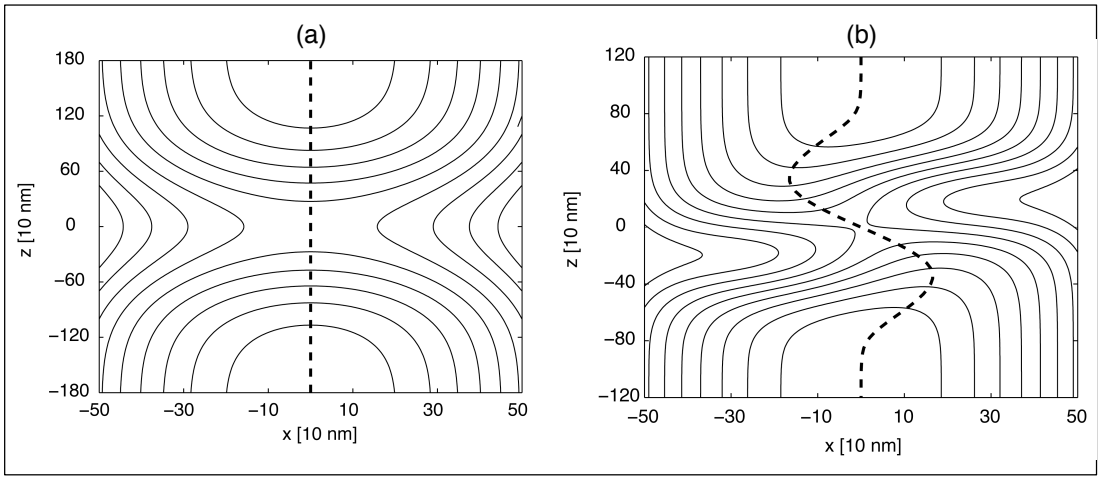

Figure 3.7: Contour plots for an electron traveling along a model quantum nanowire with embedded impurity. In panel (a) a single Gaussian function is used to represent an impurity in the wire. The maximum barrier height is 4.0 meV and the exponential decay parameter , β, is 0.012247 nm. In panel (b) two Gaussian functions are used to represent the impurity where one is offset from the center by (20.0 , 20.0) nm and the other one by (-20.0 , -20.0) nm. Both have barrier heighs of 4.0 meV and exponential decay parameters of 0.031623 nm, resulting in a saddle point with an energy of 3.594 meV located at $(x, z) = (0.0\ ,\ 0.0)$. The classical MEP, as determined by the NEB method [21], is represented as a dashed line.

rate theory, will be present. A contour plot and a cross section of the third potential are shown in Fig. (3.9).

A curved MEP offers the system the possibility to shorten the tunneling path via corner cutting at low enough temperatures. Contour plots of the first two potentials are shown in Fig. (3.7) along with the classical MEPs, as determined by the NEB method [21]. The HQTST rate is compared to results obtained from the full quantum mechanical wave function calculations and flux-flux autocorrelation function formalism for the rate constant calculation [46], this gives an 'exact' value of the rate constant to which the HQTST approximation can be compared.

In the flux-flux correlation formalism, the rate constant takes on the solution

$$Q^R k = \int_0^\infty C_f(t)\,\mathrm{d}t \tag{3.13}$$

with Q^R as the partition function for the reactant state and $C_f(t)$ as the flux-flux correlation

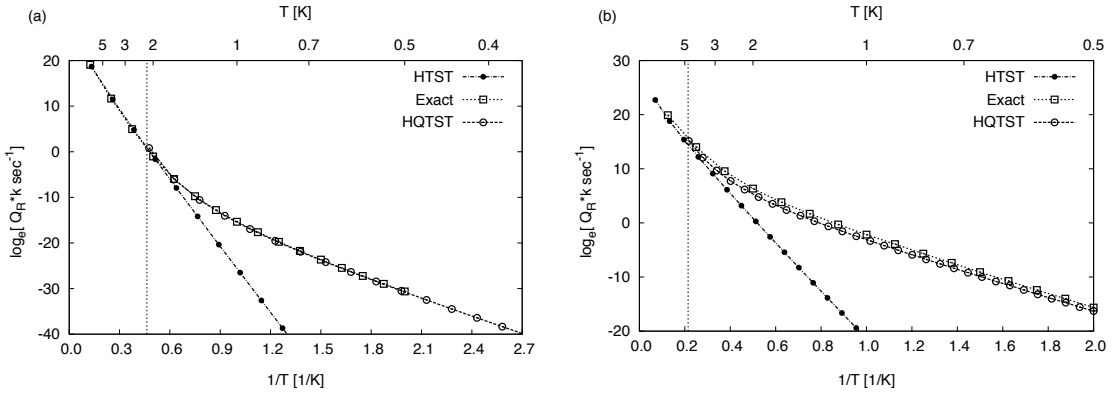

Figure 3.8: Comparison between rates calculated from HQTST theory and exact quantum mechanical theory for the model quantum wire with Gaussian impurities. For illustration of quantum effects the purely classical rate is presented as well. Panel (a) shows the results for symmetric impurity (see accompanying text) and panel (b) for asymmetric impurity. In both cases the comparison between HQTST theory and exact theory is found to be excellent. The dotted vertical lines indicate the representative crossover temperature values for each system, 2.16 K and 4.67 K respectively

function. A discrete system Hamiltonian is constructed on a uniform grid of n_x points along the x-coordinate and n_z along the z-coordinate. The corresponding matrix representation is diagonalized to produce the eigenfunctions $(\phi_i(x,z), i = 1,\ldots,n_x n_z)$ and eigenvalues $(\epsilon_i, i = 1,\ldots,n_x n_z)$. In this representation the correlation function becomes

$$C_f(t) = \sum_{i,j}^{n_x n_z} \exp\left(-\frac{\epsilon_i+\epsilon_j}{2k_BT}\right)\cos\left(\frac{\epsilon_i-\epsilon_j}{\hbar}t\right)\left(\frac{\hbar}{2m}\right)^2 \int \left|\psi_i'\psi_j - \psi_i\psi_j'\right|^2, \tag{3.14}$$

where in the last integral, the wave functions are evaluated at the classical transition state and their derivatives estimated along the reaction coordinate. The integration extends over all other degrees of freedom, except the reaction coordinate. By integrating the correlation function according to Eq. (3.13), the rate expression becomes

$$Q^R k = \lim_{t\to\infty} \sum_{i,j}^{n_x n_z} \exp\left(-\frac{\epsilon_i+\epsilon_j}{2k_BT}\right)\frac{\sin\left((\epsilon_i-\epsilon_j)t/\hbar\right)}{\epsilon_i-\epsilon_j}\left(\frac{\hbar}{2m}\right)^2 \int \left|\psi_i'\psi_j - \psi_i\psi_j'\right|^2. \tag{3.15}$$

In [46] it is noted that due to discretization of the energy spectrum, the infinite time limit of Eq. (3.15) does not explicitly exist; as time grows the discrete nature of the spectrum (i.e. $(\epsilon_i - \epsilon_j)t$) will become apparent and lead to erroneous behavior. Given a large enough

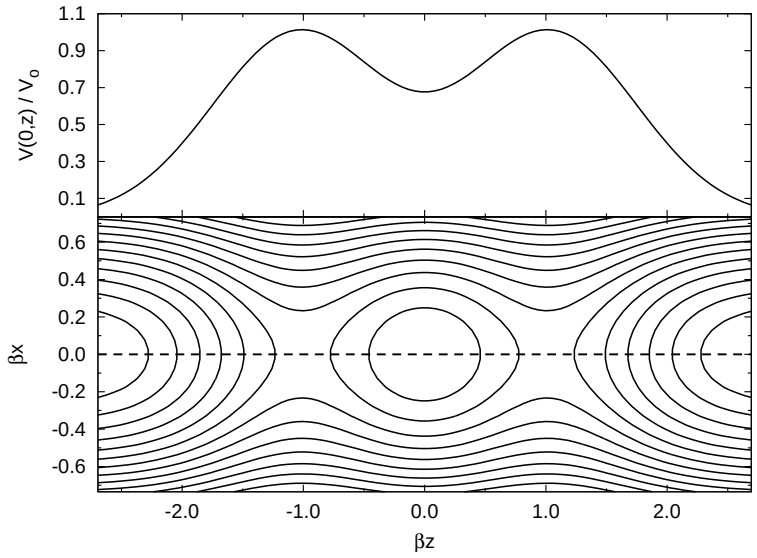

Figure 3.9: The upper panel shows a cross section (x=0) through the potential when two Gaussian barriers are aligned symmetrically along the axis of the parabolic confinement potential. The lower panel shows a contour plot of the same potential. The dotted line is the MEP and lies along the x=0 cross section.

number of eigenfunctions and hence a small spacing between energy levels, the hope is that this shortcoming will not be problematic and the rate will converge in a short time to its infinite time value. This is indeed what is observed to happen. In this study, great effort has been concentrated on reaching the convergence limit with respect to the number of eigenfunctions.

A comparison between results obtained from HQTST rate theory, Eq. (1.28), and exact quantum rate theory, Eq. (3.15), is made in Fig. (3.8). To emphasize the quantum nature of the rate constant for temperature values below the crossover temperature, the classical rate is presented as well, Eq. (1.14). Above the crossover temperature, the exact rate corresponds nicely to the classical rate but below the crossover temperature, where the HQTST rate can be obtained, the comparison to the exact rate is excellent. In both cases the HQTST rate theory is found to be within an order of magnitude of the "exact" quantum mechanical results. The ratio $k_{\mathrm{HQTST}}/k_{\mathrm{exact}}$ is found to be ~ 0.8 for the symmetric impurity and ~ 0.2

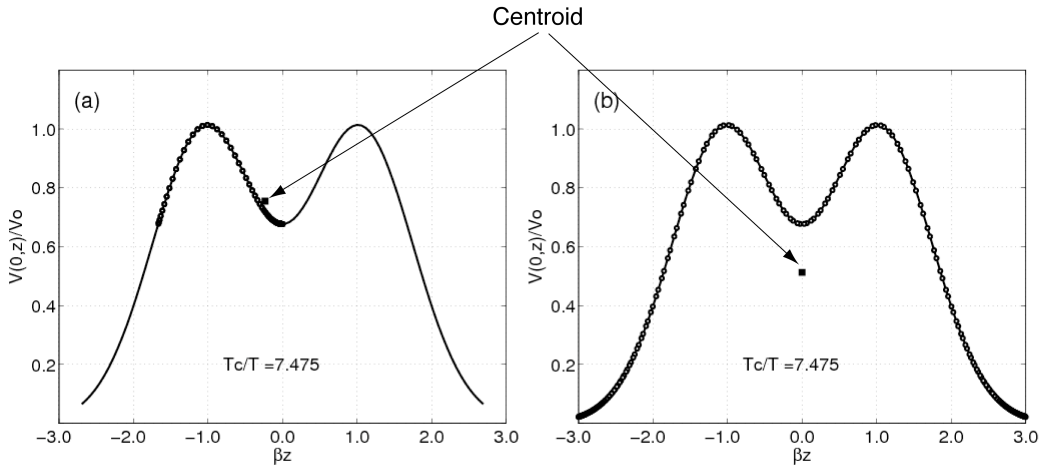

Figure 3.10: Two different instanton for a potential with two Gaussian barrier along a parabolic confinement potential. In (a), the instanton corresponds to tunneling through the first 'hump'. The instanton is shown along with the centroid coordinate at the instanton energy. The centroid will travel to the minima between the two 'humps' and stop there since the force will become zero. In (b), the instanton corresponds to tunneling through the entire barrier. At low enough temperatures it dominates the rate since its energy is much lower than for the instanton in (a). Up to 300 system replicas were used to properly resolve the CFP.

for the asymmetric one. This is quite satisfactory for most purposes.

The last case is where the two Gaussian barriers are situated along the axis of parabolic confinement potential. The HQTST rate is compared to the rate obtained from integrating the reaction probability over energy. According to Ref. [46], this procedure is identical to the flux-flux scheme used previously in this section. As before, the Hamiltonian is set up on a discrete grid and diagonalized. But instead of time propagating the flux-flux auto-correlation function, the reaction probability is calculated according to

$$P(E) = \frac{1}{2}(2\pi\hbar)^2 \mathrm{Tr}[\bar{F}\delta(E-H)\bar{F}\delta(E-H)] \tag{3.16}$$

$$\approx w\frac{\pi\hbar^4}{m}\sum_{jk} e^{-w(\epsilon-\epsilon_j)^2} e^{-w(\epsilon-\epsilon_k)^2} \left|\phi_j'(0)\phi_k(0) - \phi_j(0)\phi_k'(0)\right|^2 \tag{3.17}$$

where $\bar{F}$ is the flux operator [46], E and H are the energy and Hamiltonian, respectively. The delta function is approximated as $\sqrt{w/\pi}e^{-w\epsilon^2}$. The eigenvalues, ϵ, and eigenfunctions,

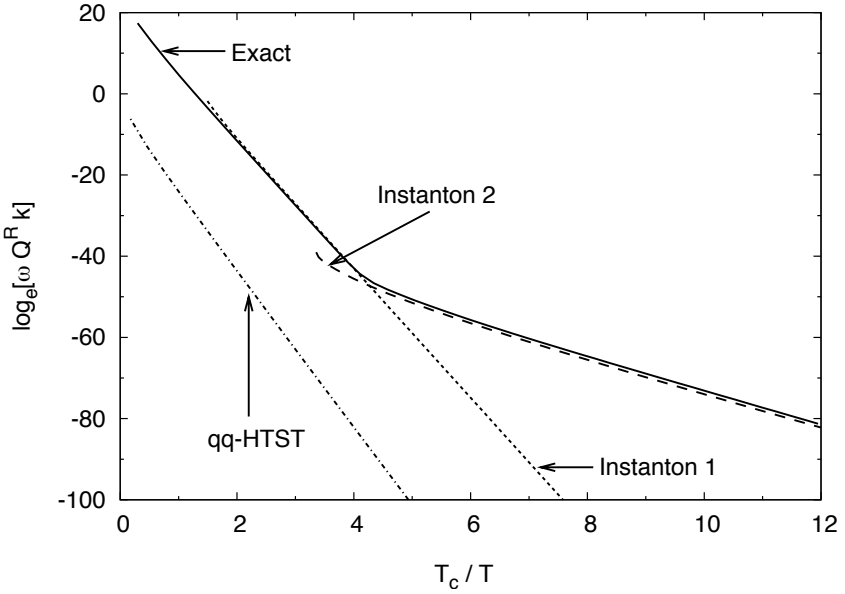

Figure 3.11: The reactive flux versus temperature for the two Gaussian barriers in a parabolic confinement potential. The results are compared to numerically exact calculations based on the integrated reaction probability (see text). At high enough temperatures instanton 1 matches well with the exact rate, but starts to deviate significantly at lower temperatures. At lower temperatures instanton 2 matches the exact rate, as the dominating mechanism is then tunneling through the entire barrier. Note the crossover from instanton 1 to instanton 2. Initially when the second instanton opens up, its energy is higher than for the first one, eventually becoming lower. The crossover corresponds nicely to the break in the exact rate.

ϕ, are the same as before. The eigenfunctions and their derivatives are evaluated at the origin. Finally, the rate is integrated as

$$Q^{\mathrm{R}} k_{\mathrm{exact}} = \frac{1}{2\pi\hbar} \int_0^\infty P(E) e^{-E/k_B T} dE, \tag{3.18}$$

with $P(E)$ as the reaction probability. As mentioned above, this procedure results in the same final answer as the one based on flux-flux auto-correlation functions.

In the case where the two Gaussian barriers are aligned along the parabola axis, two distinct instantons are found, see Fig. (3.10). One corresponds to the tunneling through a single Gaussian barrier, the other one to tunneling through the entire barrier. Calculations of the reactive flux, based on the integrated reaction probability, Eq. (3.18), as well

as HQTST calculations for both instantons are shown in Fig. (3.11). At high enough temperature, the prevalent reaction mechanism is tunneling through the first Gaussian barrier, followed by a subsequent tunneling through the other barrier. As the temperature is further lowered, a new reaction channel opens up: tunneling through the entire barrier. As is seen from Fig. (3.10), the effective activation energy (the energy of the centroid) for the second instanton eventually becomes lower than the centroid energy for the other instanton. At low enough temperatures, tunneling through the entire barrier is the dominant mechanism.

3.4 Associative desorption of H_2 molecule from a Cu(110) surface

Thermally activated processes on surfaces and interfaces are at the heart of heterogeneous catalysis and such events have been probed extensively both with experimental and computational techniques. One prototypical system that has attracted considerable interest is dissociative adsorption and associative desorption of H_2 on various facets of Cu. Both experimental and quantum calculations indicate an unambiguous deviation from the classical Arrhenius law at lower temperatures [51]. Mills et al. have published results [9, 11] for the associative desorption of H_2 from a Cu(110) surface using an empirical, many-body EAM potential [52]. The potential form includes a pair potential term (ϕ) for the screened Coulomb repulsion interaction between ions and a term for each ion embedded into a valance electron density (ρ) of its neighboring ions (F). For more details on the exact form of each term and parameters used, see Ref. [11]. This type of a potential can be expected to work well for Cu, as it has little directional bonding due to its filled d-shell. It has recently been shown [53] that the particular parameter set employed here reproduces the physical characteristics of the interaction potential energy surface somewhat poorly. But it will suffice for the purpose of this study, which is to compare the HQTST rate to a method based on free energy calculations (hence including full anharmonic effects) to estimate the rate constant. In [9, 10] Mills et al. used a free energy based method (RAW-QTST or reversible action-space work quantum transition state theory) to calculate the rate of desorption of H_2 from a Cu(110) surface. The method uses Feynman's (imaginary time) formulation of

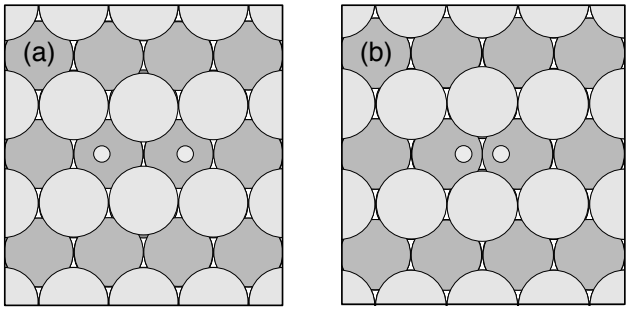

Figure 3.12: H_2 adsorbed onto a Cu(110) surface (a) and the classical desorption saddle point (b). In the minimum energy configuration the H atoms are 2.06 Å above their nearest Cu neighbors. The distance between the two H atoms is 3.05 Å. At the saddle point the distance between the H atoms is reduced to 1.34 Å and the distance to the nearest Cu neighbors increased to 2.17 Å. The energy compared to a H_2 molecule above the surface is 0.157 eV and 0.702 eV for the absorbed state and transition state, respectively.

the quantum partition function

$$Q = \int e^{-S_E(q)/\hbar}\, \mathcal{D}[q], \tag{3.19}$$

where $S_E = \int_0^{\beta\hbar} \mathcal{H} d\tau$ is the Euclidian action with $\mathcal{H}$ and q as the system (N dimensional) Hamiltonian and coordinates, respectively. In a discrete representation the integral becomes a finite sum. Utilizing P system replicas for a discrete representation of the Feynman path integral, the Euclidean action in Eq. (3.19) becomes

$$S_E(\mathbf{q}) = \Delta\tau \sum_i^P \left(\frac{\mu}{2} \left| \frac{q_{i+1} - q_i}{\Delta\tau} \right|^2 + V(q_i) \right). \tag{3.20}$$

Here, $\Delta\tau = \hbar / k_B T P$ is the imaginary time step along the CFP and $\mathbf{q}$ represent the coordinates of all the N classical coordinates of the P system replicas. The free energy is then calculated as the cumulated reversible work needed to move this higher dimensional system from the reactant state to the transition state, constrained to a $NP-1$ dimensional cone along the reaction coordinate. The reaction coordinate is chosen to be the minimum action path (MAP) which is analogous to the classical MEP, expect that the beads along the elastic band are now discrete, closed imaginary time Feynman paths. Since the system replicas in the Feynman paths (the CFPs) are connected to their neighbors through springs

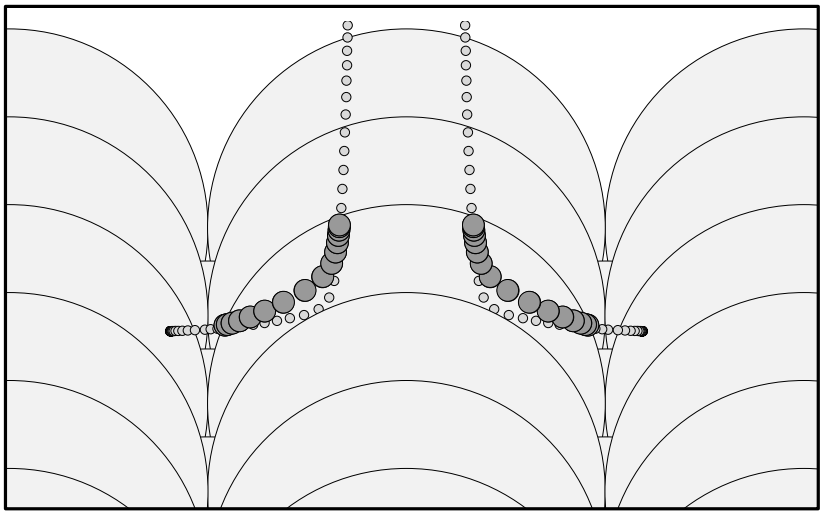

Figure 3.13: The MEP (small grey circles) for associative desorption of H_2 off a Cu(110) surface, along with the the instanton (darker circles) at 100 K. 100 system replicas are used to represent the closed Feynman path (CFP). A clear corner cutting effect to shorten the tunneling path is visible at this temperature.

with temperature dependent spring constants, the replicas collapse into each over above the crossover temperature and along with it, the entire MAP onto the MEP. The MAP is the path (along with nearby paths) that contributes most to the quantum partition function, see Eq. (3.19). The RAW-QTST can in fact be considered to be a general quantum transition state theory, but the prefactor was taken from Affleck's WKB analysis [54] of a simple barrier and is therefore not explicitly derived from rigorous first principles theory. It naturally tends to variational transition state theory [55] in the classical limit and variational centroid density theory [56, 8] above the the classical-quantum crossover temperature (see Eq. (1.27)). Moreover it is reduced to HQTST theory in the low temperature, harmonic limit. In analogy with classical, harmonic transition state theory where the transition state is a first order saddle point along the MEP, the instanton is a first order saddle point along the MAP.

The system used in Refs. [9, 10] and this study consists of 216 Cu atoms representing the (110) surface. The Cu atoms are separated into 6 layers, each containing 36 atoms. The

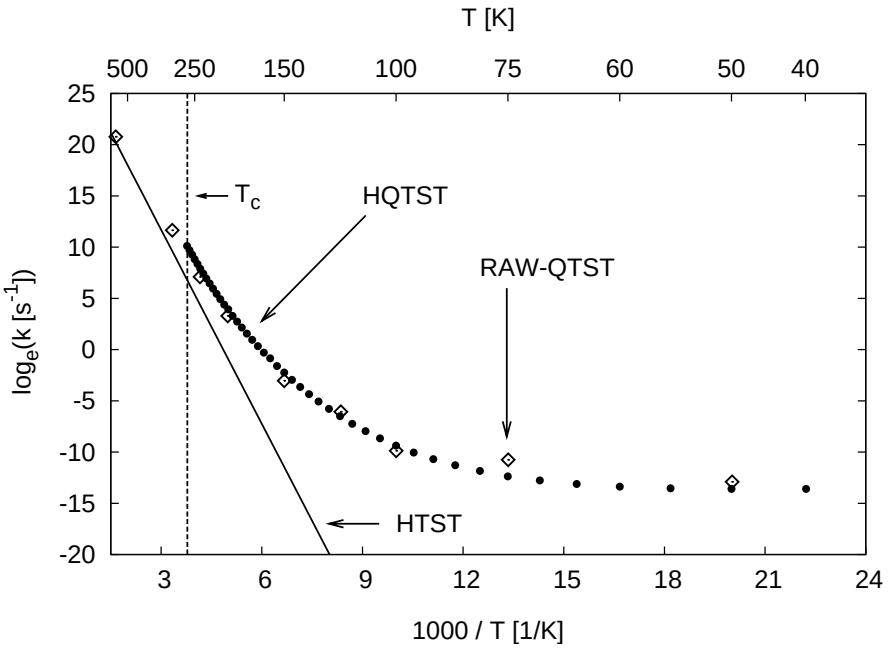

Figure 3.14: Comparison for the rate of associative desorption of H_2 from a Cu(110) surface where an EAM-type potential is used to describe the atomic interactions. Excellent agreement is found between a full anharmonic quantum rate theory (RAW-QTST) and its harmonic approximation (HQTST) over a wide range of temperature. An uniform shift has been applied to the RAW-QTST data (Ref. [10]) so it asymptotically approaches the HTST result in the high temperature limite. The crossover temperature is determined to be 264.6 K.

EAM potential gives the energetically most favorable configuration of the hydrogen atoms on the surface as aligned symmetrically along a surface valley, separated by a long bridge. The two hydrogen atoms adsorbed onto the surface are shown in figure Fig. (3.12), along with the desorption transition state. The energy of the transition state lies 0.544 eV above the energy of the absorbed state. The minimum energy path (MEP) has been traced out be the NEB [21] method and is depicted in Fig. (3.13). The MEP is completely contained within a plane spanned by the initial, transition and final state and is symmetric about a plane parallel to the surface normal, orthogonal to the MEP plane and intersecting the transition state. The movement of the surface Cu atoms is minimal compared to the movement of the H atoms, or just about 0.1 Å for the two nearest Cu atoms in the initial state.

The comparison between the HQTST and RAW-QTST results is shown in Fig. (3.14). The results in Ref. [10] were shifted by the classical prefactor, so they have been shifted back by a uniform constant. Quantum effects on the rate are found to be large at low temperature; at around 150 K the rate is completely dominated by the tunneling mechanism. Overall the agreement between the full anharmonic (RAW-QTST) results and the harmonic approximation (HQTST) is excellent. In the low temperature limit, 100 replicas were needed to properly resolve the CFP, fewer replicas resulted in an artificial rise in the the reaction rate at the low temperature end. Interestingly, the data from Ref. [10] seems to be a bit jagged, indicating that more replicas should have been used to achieve properly converged results.

3.5 Dissociative adsorption of H_2 onto a Cu(100) surface

The sticking coefficient for H_2 and D_2 on a Cu(100) surface has previously been measured over a limited temperature range by Rasmussen et al. [57]. Results based on instanton rate theory (HQTST) are compared to measured values from Ref. [57] as well to accurate quantum dynamics calculations by Somers et al. [58]. For details on the quantum mechanical wave packet propagation used by Somers et al., refer back to Ref. [59]. A potential energy function (PES5) recently developed by Olsen et al. [60] is used to perform the calculations. The 6D potential was fitted to a set of DFT calculations, using the GGA approximation and periodic boundary conditions to describe the system. The corrugation reduction procedure (CRP)[61] was used to generate the global potential energy surface.

A short derivation is presented on how to calculate the sticking coefficient directly from instanton theory. Define the sticking coefficient θ_o as

$$\theta_o = \frac{N^{\text{reactive}}}{N^{\text{total}}}, \tag{3.21}$$

where N^{reactive} is the number of reactive collisions per unit time per unit area and N^{total} is the total number of collisions per unit time per unit area. The latter is obtained from the elementary theory of ideal gases (a particularly good reference can be found in Ref. [44]) as

$$N^{\text{total}} = \frac{N}{4V}\bar{v} = \frac{N}{4V}\sqrt{\frac{8k_BT}{\pi M}}, \tag{3.22}$$

with N being the total number of particles, V the volume they occpy, $\bar{v}$ the average speed (Maxwell-Boltzmann distribution), k_B Boltzmann's constant, T the temperature, and M the mass of a gas molecule (note that M is *total* mass of the molecule). The numerator in Eq. (3.21) can be obtained in the following way: The number of reactive collision during a time t_1 within a surface area A_s is given by $A_s t_1 N^{\text{reactive}}$. This number can also be obtained from e.g. HQTST rate theory as $\eta_s t_1 N k_{\text{HQTST}}$, with k_{HQTST} being the single molecule HQTST rate at one reactive site within the surface area A_s. The factor η_s is used to account for the fact that only a fraction of the available sites might be available under the reaction conditions (or that there is more than one reaction site inside the surface area A_s). Thus,

$$N^{\text{reactive}} = \frac{\eta_s N k_{\text{HQTST}}}{A_s}. \tag{3.23}$$

Inserting Eqs. (3.22) and (3.23) into Eq. (3.21) gives

$$\theta_o = \frac{4\eta_s V}{A_s}\sqrt{\frac{\pi M}{8k_B T}}\; k_{\text{HQTST}}. \tag{3.24}$$

An expression for k_{HQTST} can be retrieved from instanton rate theory (harmonic quantum transition state theory) as

$$k_{\text{HQTST}} = \frac{\tilde{Q}}{Q^R}\exp\left(\frac{-V_{ins}}{k_B T}\right), \tag{3.25}$$

where V_{ins} is the effective potential at the instanton. Here, $\tilde{Q}$ is referred to as the instanton partition function. An expression for it will be developed later. First an expression for the reactant partition function, Q^R, will be developed. The simplest approximation to make is to consider an ideal diatomic gas, i.e., a collection of non-interacting rigid-rotor rotating dumbbells where molecular vibrations are treated within the harmonic approximation [note that this approximation is consistent with Eq. (3.22)]. For a single particle (k_{HQTST} is defined to be a single molecule rate constant), Q^R factors into

$$Q^R = Q_{trans}\; Q_{vib}\; Qelec\; Q_{rot}\; Q_{nucl}, \tag{3.26}$$

where

$$Q_{trans} = \left(\frac{2\pi M k_B T}{h^2}\right)^{3/2} V, \tag{3.27}$$

$$Q_{vib} = \frac{e^{-\hbar\omega/2k_BT}}{1-e^{-\hbar\omega/k_BT}}, \tag{3.28}$$

$$Q_{elec} = g\ e^{-E_e/k_BT}. \tag{3.29}$$

Here, the zero of the electronic energy E_e must be chosen properly and in correspondence with the zero of the energy used for the instanton rate k_{HQTST}. The most natural choice is to define the energy of the bottom of the well in the reactant region to be zero, implying E_e to be zero. This is consistent with the choice made in Eq. (3.25). The multiplicity of the electronic state is accounted for by g. For H_2 it is one, and thus $Q_{elec} = 1$ (note that for the temperature range we are interested in there will be no electronic excitations of H_2). For a homo-nuclear molecule like H_2 with nuclear spin $\frac{1}{2}$, Q_{rot} and Q_{nucl} couple together because of symmetry (see [12], chapters 6-4 and 6-5). This is the remainder of Q^R,

$$Q_{rot,nucl} = \sum_{\text{J even}} (2J+1)e^{-\hbar^2 J(J+1)/2Ik_BT} + 3\sum_{\text{J odd}} (2J+1)e^{-\hbar^2 J(J+1)/2Ik_BT}, \tag{3.30}$$

with I being the moment of inertia, μr_e^2, of the molecule (note that the *reduced* mass μ of the molecule enters in this expression). Together this gives the reactant partition function as

$$\begin{aligned} Q^R = & \left(\frac{2\pi M k_B T}{h^2}\right)^{3/2} V\ \frac{e^{-\Theta_v/2T}}{1-e^{-\Theta_v/T}} \\ & \left(\sum_{\text{J even}} (2J+1)e^{-\Theta_r J(J+1)/T} + 3\sum_{\text{J odd}} (2J+1)e^{-\Theta_r J(J+1)/T}\right), \end{aligned} \tag{3.31}$$

where

$$\Theta_v = \hbar\omega/k_B \tag{3.32}$$

and

$$\Theta_r = \hbar^2/2\mu r_e^2 k_B \tag{3.33}$$

Substituting k_{HQTST} and Q^R into (3.24) results in

$$\begin{aligned}\theta_o &= \frac{4\eta_s V}{A_s}\sqrt{\frac{\pi M}{8k_BT}}\tilde{Q}\exp\left(\frac{-V_{ins}}{k_BT}\right)\left(\frac{h^2}{2\pi M k_BT}\right)^{3/2}\frac{1}{V}\,\frac{1-e^{-\hbar\omega/k_BT}}{e^{-\hbar\omega/2k_BT}} \\ &\quad \left(\sum_{\text{J even}}(2J+1)e^{-\Theta_r J(J+1)/T}+3\sum_{\text{J odd}}(2J+1)e^{-\Theta_r J(J+1)/T}\right)^{-1} \\ &= \frac{8\eta_s\pi^2\hbar^3}{A_s M k_B^2 T^2}\sinh\left(\frac{\Theta_v}{2T}\right)\Gamma_{\mathrm{HQTST}} \\ &\quad \left(\sum_{\text{J even}}(2J+1)e^{-\Theta_r J(J+1)/T}+3\sum_{\text{J odd}}(2J+1)e^{-\Theta_r J(J+1)/T}\right)^{-1},\end{aligned} \tag{3.34}$$

where Γ_{HQTST} is the right hand side of Eq. (1.28) with $S_{ins}/\hbar = V_{ins}/k_BT$.

From the H_2/Cu(100) PES the following values are obtained for an H_2 molecule far from the surface: $\omega = 2\pi$ 4168.6 cm^{-1} and $r_e = 0.77815$ Å. Inserting these values in Eqs. (3.32) and (3.33) gives $\Theta_v = 5997.6\ K$ and $\Theta_r = 79.515\ K$ (in reasonable agreement with the values given in Table 6-1, page 95 in Ref. [12]). The area of the Cu(100) surface unit cell is $A_s = 4.8238^2$ bohr$^2 = 6.5160\times10^{-20}$ m^2 and the number of active sites is two, $\eta_s = 2$. With the all the above information the calculated sticking coefficient is

$$\begin{aligned}\ln(\theta_o) &= \ln\left(\frac{8\eta_s\pi^2\hbar^3}{A_s M k_B^2}\right)-2\ln(T)+\ln\left(\sinh\left(\frac{\Theta_v}{2T}\right)\right)+\ln(\Gamma_{\mathrm{HQTST}}) \\ &\quad -\ln\left(\sum_{\text{J even}}(2J+1)e^{-\Theta_r J(J+1)/T}+3\sum_{\text{J odd}}(2J+1)e^{-\Theta_r J(J+1)/T}\right).\end{aligned} \tag{3.35}$$

For comparison with Eq. (3.35) $\ln\Gamma_{\mathrm{HQTST}}$ in the third term in Eq. (3.35) can be replaced with

$$\Gamma_{\mathrm{qq-HTST}} = \prod_{i=1}^{N-1}\frac{1}{2\sinh(\hbar\omega_i/2k_BT)}e^{-\Delta E/k_BT}$$

where ω_i are the stable angular vibrational frequencies at the classical saddle point and ΔE is the energy of the saddle point, as compared to the reactant state.

For comparison between the present HQTST sticking coefficient and the quantum wave packet propagation (QD) from Ref. [60], refer to Fig. (3.15). In obtaining the QD data, Olsen et al. ran wave packet propagation with kinetic energy as low as 0.3 eV, which is still about an order of an magnitude larger than what would be consider chemically relevant

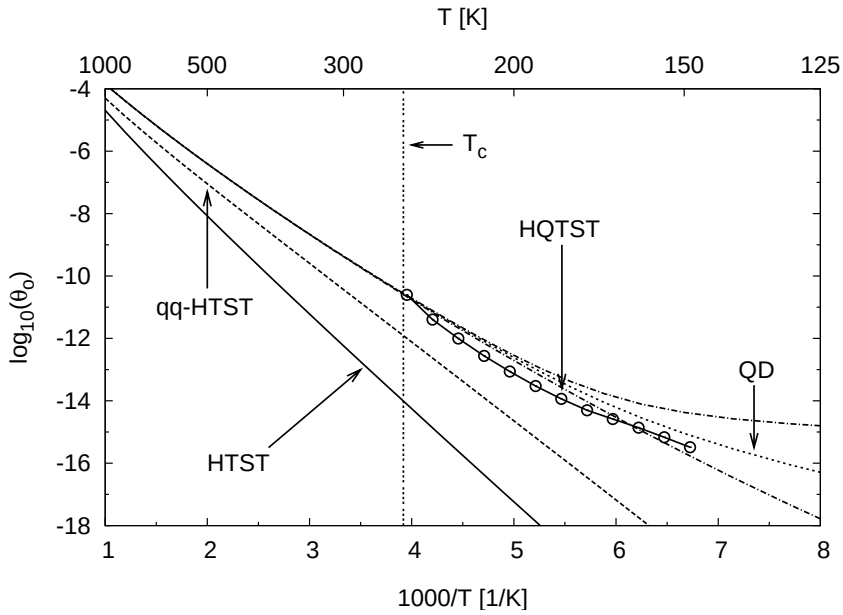

Figure 3.15: Comparison between the HQTST sticking coefficient and more accurate quantum dynamics calculations (QD). To emphasize the sticking enhancement due to tunneling, results for the sticking coefficient calculations based on qq-HTST (no tunneling, but zero point energy) and HTST (no tunneling, nor zero point energy) are presented as well. Overall, the agreement between the HQTST is satisfactory. The dash-dot lines above and below the QD line represent the uncertainty in the extrapolation scheme employed. The HQTST calculations are based on 100 replicas in the CFP and the crossover temperature, T_c, is 255.17 K.

for the sticking coefficient under investigation here. To rectify this dilemma, Olsen et al. extrapolate the results close to zero in energy, both by using a linear extrapolation scheme, as well as a quadratic one. The dash-dot lines around the QD results in Fig. (3.15) represent the error inherent in this procedure. The QD results are an average over several different extrapolations. Any statistical error due to the finite time length of the dynamical paths would be added to this 'extrapolation' error. Overall there is good agreement between the two different approaches, especially if all the uncertainties regarding the QD results are kept in mind. Also, the QD calculations are horrendously complicated and time consuming, representing months of computation on parallel machines with huge RAM. On the other hand, the HQTST ran in about 2 minutes on a somewhat aging Apple PPC laptop computer.

Finally, compare the HQTST sticking coefficient to the experimental results from Ras-

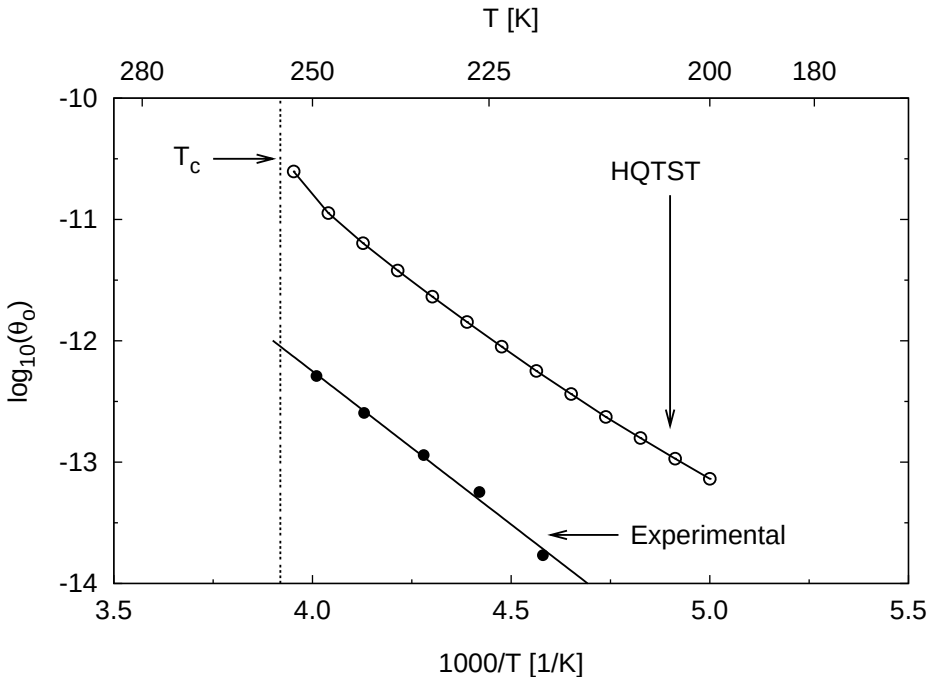

Figure 3.16: Comparison between the calculated HQTST sticking coefficient and experimental bulb measurements. The agreement is good, with the discrepancy between measured and calculated around 1-2 orders of magnitude.

mussen et al. [57], based an bulb experiments where the H_2 gas above the Cu surface was thermalized. Given the nature of the empirical, low dimensional potential used and any systematic experimental error, the agreement is surprisingly good (perhaps fortuitously). The discrepancy is only around 1-2 orders of magnitude. The comparison is shown in Fig. (3.16).

Chapter 4

QUANTUM RATE CONSTANTS FROM FIRST PRINCIPLES AND SEMI-EMPIRICAL ATOMIC FORCES

4.1 Hydrogen abstraction from ammoinaborane

The U.S. Department of Energy (DOE) has stipulated that hydrogen storage devices should contain a minimum of 6.5% hydrogen by mass and be capable of delivering hydrogen gas at a pressure of 1 bar at temperatures between 50-100 °C. At the current level of technology this constitutes a substantial hurdle. A great deal of effort has been given in the past to light metalhydrides, for example MgH_2 (7.6% by mass ratio), and other magnesium-metal alloys. Although great progress had been made, both in the understanding of these system, as well as with practical applications, fundamental problems pertaining to loading and unloading of the devices still persist. However, interest in magnesium and other metallic alloys as a potential storage medium remains high still to date.

Another particularly attractive candidate for a hydrogen storage device, due to the high hydrogen mass percent (19.5%), is ammoinaborane (also known as borazane), H_3BNH_3. Borazane is a structural analog of carbon based ethane. Solid ammoinaborane is known to thermally decompose at relatively mild temperatures [62, 63, 64] in two partially overlapping processes, both yielding H_2 gas and heat. The first process involves decomposition of ammoinaborane to hydrogen gas and a solid residue of polymeric aminoborane ($[H_2BNH_2]_x$). The associated change in enthalpy is measured to be $\Delta H = -(0.22 \pm 0.01)$ eV [62]. The second step is a further decomposition of the polymeric aminoborane to hydrogen gas and a noncrystalline residue, the exact composition of which depends on the sample heating rate and has the stoichiometry BNH_y with y ranging from 1.2-2.4 [64]. The two processes can be completely separated by initially decomposing ammoinaborane isothermally at a temperature below the melting temperature (385 K) followed by an additional heating up to 500 K [62]. Each step is found to release about 1 mol of H_2 per mol of ammoinaborane,

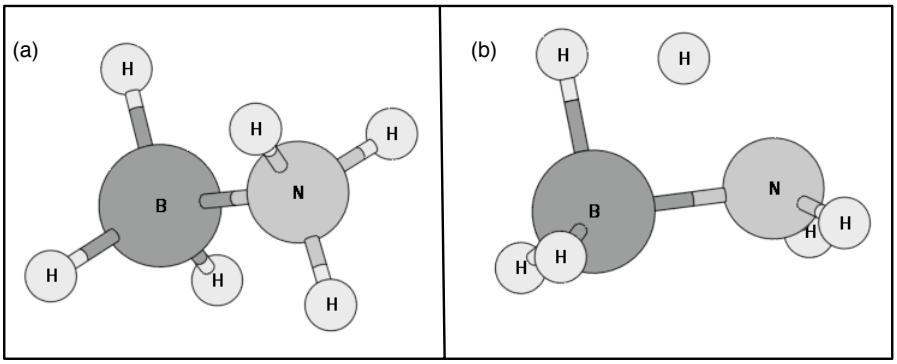

Figure 4.1: Reactant and transition states for H_3BNH_3. The reactant state (a) is in a staggered configuration (C_{3v} symmetry). Before reaching the transition state (b) the NH_3 group rotates into an eclipsed configuration and one of the NH bonds becomes stretched as the H atom reacts with one of the H atoms bonded to the boron atom. The remaining H atoms in the transition state have moved considerably upwards and are close to be in a plane, a preparation for the product configuration (H_2BNH_2). The final transition state has a C_s symmetry.

yielding an impressive overall hydrogen storage capacity of about 14% [63] relative the original amount of ammoinaborane. Interestingly enough the high mass percent is found to be independent of the heating rate, even though the first process is not run to completion [63]. Lower heating rates produce smaller amounts of other volatile side products, something that must be taken into account with regards to future applications, for instance as a generator for a fuel cell. Upon analyzing the gas phase products, monomeric aminoborane, borazine ($B_3N_3H_6$,BN-analog of benzene) and diborane (B_2H_6) have been detected [63]. An attempt to reduce the amount of gas phase side products has spurred an interest in aminoborane reactions in ionic solvents, see for example. Ref. [65] and references therein.

Previously Li et al. [66] have studied the dehydrogenation of ammoinaborane in the gas phase at the G3MP2B3 [67] level of theory using geometries optimized with B3LYP [68, 69, 70] and a aug-cc-pVTZ basis set. The rate constant for the process was calculated and reported using canonical variational transition state theory (CVT) [15], with and without small curvature tunneling correction (SCT) [13, 14, 15]. See Sec. (1.3) as well.

Here, a study of the hydrogen abstraction rate from H_3BNH_3 in the gas phase has been

conducted at the AM1 [71] level of theory, as implemented in the MOPAC [72] computational suite. AM1 (Austin Model 1) is a semi-empirical forcefield method used for the calculation of a molecular electronic structure. It is based on the Neglect of Differential Diatomic Overlap (NDDO) formalism which explicitly includes only two-center integrals for repulsion between two charge distributions located at each center. This is a considerable improvement over *ab-initio* Hartree-Fock methods where all two-center integrals need to be evaluated. Most present day semi-empirical methods are based on the NDDO approximation. Additional nuclear repulsion is added to NDDO in the AM1 formalism in the form of Gaussian charge centers located at various distances between any two nuclei as to effectively reduce the repulsion of the atom at close distances. The additional Gaussian charges lead to great improvements in the geometry and energy predictions, especially when dealing the hydrogen bonded systems. As compared to Li et al. [66], AM1 predicts the zero-point energy corrected barrier height to be 1.567 eV which is in reasonable agreement with the results reported in Ref. [66], of 1.41 eV at the G3MP2B3 level of theory, given the vast difference in sophistication between AM1 and G3MP2B3. Unfortunately the comparison between the heat of the reaction is not as favorable; by assuming ideal gas behavior AM1 predicts -0.92 eV, but the prediction at the G3MP2B2 level of theory is -0.19 eV. The experimentally derived value is -(0.22 $\pm$ 0.01) eV [62]. There are clearly some difference between the two potential energy surfaces that precludes any direct comparison between the two calculated rate constants, even if performed at the same level of approximation. The rate constant was calculated at various levels using the AM1 semi-empirical potential. The simplest and most commonly used approximation is the harmonic transition state theory (HTST), where the rate is calculated based on a hyper planar dividing surface at the saddle point, orthogonal to the reaction coordinate. The partition functions, in particular the vibrational partition function, are assumed to be purely classical and the potential harmonic. The term *quasi-quantum*, qq-HTST for short, will be adopted is the vibrational partition functions are made to be quantum mechanical, as to distinguish it from the classical HTST. The rate constant expressions are

$$k^{\mathrm{HTST}}(T) = \frac{1}{2\pi} \frac{\prod_i^{3N} \omega_i^R}{\prod_i^{3N-1} \omega_i^{TS}} \exp\left(-\Delta E / k_B T\right) \tag{4.1}$$

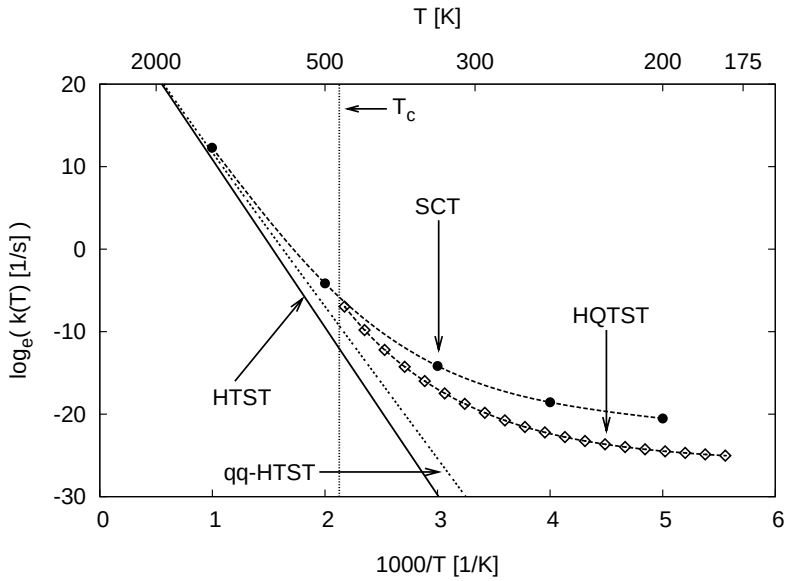

Figure 4.2: Reaction rates as a function of temperature for a hydrogen abstraction from gas phase ammoinaborane molecule. Quantum effects are seen to dominate the reaction rate, even at room temperature. The CFP is represented by 96 system replicas. The crossover temperature is calculated to be $T_c = 470.1$ K.

and

$$k^{\mathrm{qq-HTST}}(T) = \frac{k_B T}{2\pi h} \frac{\prod_i^{3N} 2\sinh\left(\hbar\omega_i^R/2k_BT\right)}{\prod_i^{3N-1} 2\sinh\left(\hbar\omega_i^{TS}/2k_BT\right)} \exp\left(-\Delta E/k_BT\right). \tag{4.2}$$

Here ΔE is the energy difference between the reactant state and the transition state on the Born-Oppenheimer potential surface, ω^R and ω^{TS} are the harmonic angular frequencies corresponding to stable vibrational modes at the reactant and transition states, respectively. The unstable mode at the transitions state is excluded from the transition state product. Both approximations include no tunneling and should coincide in the infinite temperature limit. The HQTST rate was calculated as described in Sec. (1.5). The results are shown in Fig. (4.2). For comparison, the rate was calculated using CVT with small curvature tunneling (SCT) corrections as calculated with the POLYRATE [73] package using AM1 [74]. Variationally moving the hyper planer dividing surface does not seem to be important for this system, the CVT rate (not shown in Fig. (4.2)) overlap the qq-HTST results in the entire temperature range under investigation. The crossover temperature was calculated to

be $T_c = 470.1$ K, according to Eq. (1.27). Close to the crossover temperature, the HQTST rate and CVT/SCT appear to compare favorably. But as the temperature is decreased even further, the two rates start to deviate, presumably since the tunneling path moves further away from the classical reaction coordinate. Compared to the HQTST, the SCT is generally referred to as a lesser approximation to the true rate since it is based on a harmonic expansion along the classical reaction coordinate. Alternatively, the HQTST rate is calculated as a harmonic expansion around the quantum mechanical reaction path, the minimum action path (MAP).

In conclusion, it is apparent that tunneling of hydrogen atoms is the dominant transition mechanism at 400 K, the temperature where hydrogen desorption is experimentally observed to occur. The rate calculation with HQTST theory which includes tunneling is 300 times larger than the rate constant evaluated from quasi-quantum TST, an approximation that includes zero point quantum effects but not tunneling. The semiclassical small curvature tunneling (SCT) approximation was found to overestimate the rate constant in this case by nearly a factor of 10.

4.2 H atom diffusion in metals

A great deal of effort over the last few decades has been directed towards studying hydrogen in metals, as is amply evident from the exhausting array of reported studies in the literature, both experimental and theoretical. See for example [51, 75, 76] and references therein. This interest can be explained by that from a theoretical standpoint hydrogen in metals can serve as phenomenological workbench for which knowledge and experience can be extracted from and extended to more complicated systems. Also, when embedded in or on metals, hydrogen and its isotopes, being the lightest of all the elements exhibit considerable amount of quantum mechanical characteristics, such as zero point energy effects, tunneling and discrete nature of the vibrational levels. On the experimental side, interstitial hydrogen changes the local electronic and magnetic properties of the surrounding medium, giving rise to potential structural changes and complex phase diagrams. Recently, with the current efforts to diversify the available energy resources, interest in the various properties of hydrogen in metals has been rekindled.

4.2.1 H atom diffusion in Ta

Here, a diffusion study of dilute hydrogen in the α-phase of elemental tantalum (Ta) has been carried out using the HQTST rate formulation. Ta has a bcc structure and experimentally it is a well known fact that quantum effects are much more pronounced in bcc metals than in fcc metals. Bcc metals generally have lower barriers between interstitial sites and the sites lie closer together than in fcc metals. Both facilitate quantum mechanical tunneling.

Forces and energies were generated at the DFT level of theory, utilizing a plane wave basis set and periodic boundary conditions. The Kohn-Sham equations [77] were solved with the *Vienna Ab-initio Simulation Package* (VASP) [35, 36, 37, 38], where the interaction between ion cores and electrons was described by the projector augmented wave formalism (PAW) [78]. The the default kinetic energy cut-off value for the plane wave basis function of 250 eV (18.4 Ry) was used. The exchange-correlation part of the potential was PW91 [79]. The Brillouin zone was sampled by a 3x3x3 k-point mesh generated with the Monkhorst-Pack scheme [80]. The system was described with 16 Ta atoms, with four atoms in four layers, in the bcc crystal configuration. After a volume relaxation, the lattice constant was determined to be 3.32 Å, in excellent agreement with the experimental value of 3.31 Å [81].

The most stable configuration was found to be with the H atom occupying a tetrahedral hole (T_d) in the crystal structure, as is most common for metals with a bcc structure. The diffusion was assumed to take place via hydrogen atom migration between two neighboring (T_d) configurations.

To reduce the computational effort, only five Ta atoms surrounding the two T_d sites where allowed to relax from the lattice configuration. Table (4.2.1) summarizes the effects of the chosen computational parameters on the classical reaction barrier. From the comparison, it is evident that the parameters employed here result in both the classical barrier height and curvature reasonably well converged. In Ref. [82], a larger system is used with approximately the same parameters in VASP. Compared to the experimental results from Ref. [83] based on the Grosky effect, all the theoretical values in Table (4.2.1) overestimate the reaction barrier height. However, the theoretical values are within acceptable range from the experimental results, especially when the the current level of accuracy for DFT

Table 4.1: Energy of the classical saddle point relative to the relaxed T_d in a Ta. The saddle point energy is relatively constant, as compared to the computational parameters used in the study, if a denser k-point grid is used and/or more Ta atoms (nTa) are allowed to relax from the bulk configuration. Relaxing the spin restriction did not introduce any changes. The calculated crossover temperature is underestimates in all instances.

k-point mesh	nTa atoms	ΔE [eV]	T_c [K]	Ref.
3 x 3 x 3	5	0.193	178	Present study
4 x 4 x 4	5	0.200	181	Present study
4 x 4 x 4	16	0.196	179	Present study
4 x 4 x 4	54	0.180	-	[82]
-	-	0.136 ± 0.009	$\approx$220	[83]

based methods is considered. It was found necessary to use 29 movable with another 29 shadow replicas in the discrete representation of the CFP over the entire temperature range. Second derivatives were estimated numerically with a finite difference scheme where the step size was set fixed to $1.0 \cdot 10^{-3}$ Å. The CPF was considered to be converged to the instanton once all force components where less than $1.0 \cdot 10^{-4}$ eV/Å and was achieved typical in less than 700 force calculation per movable image if the initial configuration was chosen to be a previously converged instanton at a higher temperature.

The hydrogen atom is self-trapped at a interstitial site by local relaxation of the neighboring lattice atom surrounding the interstitial site. A neighboring interstitial site will be higher in energy compared to the relaxed site if the hydrogen atom would be instantaneously teleported from the current site. Classically, thermal energy is needed to overcome the potential energy barrier separating the two sites. Quantum mechanically, the process requires thermal fluctuations to bring the two sites into *coincidence*, with the two sites at the same energy level and the hydrogen delocalized over both sites. This is referred to as thermally or phonon assisted tunneling.

Recently, Sundell and Whanström [84, 82] have carried out a numerical study on the same system, using very similar computational parameters. By setting up a three dimensional

grid for a hydrogen atom self-trapped in a T_d site and a hydrogen atom delocalized over two neighboring T_d sites, a three dimensional Schrödinger equation was solved and the vibrational levels along with tunneling matrix elements [85] extracted. The delocalization of the hydrogen atom was simulated by placing two hydrogen atoms at the different sites and using a linear combination of the symmetrized Hellmann-Feynman forces. Working within the framework of the high temperature limit of the small polaron theory [86], where the rate is expressed as

$$\nu = \frac{1}{\hbar}\left(\frac{\pi}{4E_c k_B T}\right)^{1/2} J^2 \exp\left(-E_c/k_B T\right), \tag{4.3}$$

with J as the tunneling matrix element and E_c the activation energy needed to induce the coincident configuration, Sundell et al. calculated the hydrogen diffusion rate between 100 K and 200 K and obtained results in good agreement with experimental work by Messer et al. [87]. Small polaron approximation is valid if the temperature is low enough so that excited vibrational states can be ignored, but high enough for the lattice vibrations to be treated classically.

Assuming a random walk model (uncorrelated jumps) to describe successive migrations between two stable T_d configurations, the diffusion constant, $D(T)$, as a function of temperature, can be calculated as

$$D(T) = n\frac{l^2}{2d}k(T) \tag{4.4}$$

$$= 9.13 \cdot 10^{-17} k(T)\ [\mathrm{cm}^2/\mathrm{s}] \tag{4.5}$$

where l the distance (1.17 Å) between two stable T_d sites, d is the dimensionality of the problem (three in this case), n is the number of symmetry cancels of escape (four in present case), and $k(T)$ is the rate constant as calculated by the HQTST rate theory.

The calculated HQTST rate is compared with two different experimental results, one based on the Grosky effect [83], and the other on NMR spin-lattice relaxation times [87]. In the Grosky effect measurements, a concentration gradient is introduced by expansion and contraction of the lattice caused by bending the sample. The hydrogen atoms migrate along the gradient, causing a time dependent anelastic strain. From the relaxation time of the anelastic strain, the diffusion constant can be obtained. Since the anelastic strain is

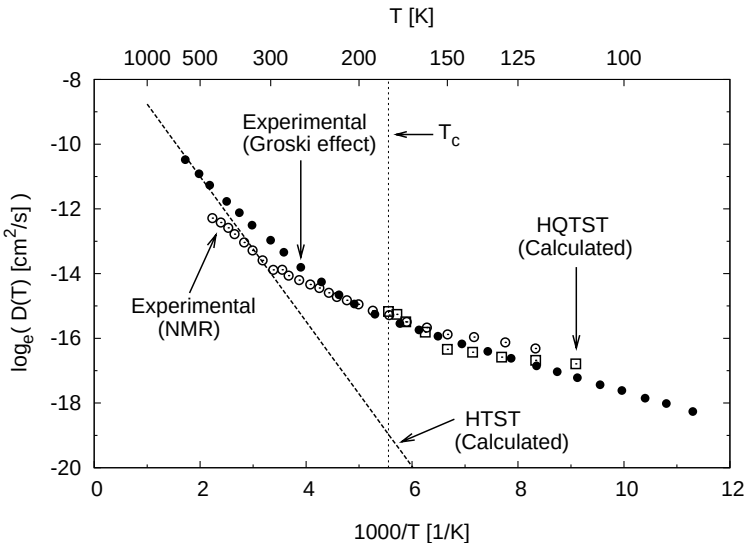

Figure 4.3: Diffusion constant for a hydrogen atom in Ta. The diffusion constant as calculated from the HQTST rate theory is in an overall good agreement with the experimental data. The CFP was represented by 29 movable system replicas and 29 shadow replicas, giving a total of 57 replicas. The crossover temperature was calculated from the curvature of the classical saddle point as 178 K, somewhat less than the experimental values of around 220 K. The open circles were extracted from Ref. [83] and the filled circles from Ref. [87].

macroscopic in nature, the diffusion constant obtained by the Grosky effect can be influenced by impurities (adatoms, vacancies, etc.), since hydrogen atoms will easily become trapped at impurities, especially at lower temperatures. This will result in a lower effective diffusion rate. On the other hand, the NMR spin-lattice relaxation times are much more closely related to the elementary jump processes. In figure Fig. (4.3) the comparison between the two experimental measurements and the calculated HQTST rate is depicted. At the lower temperature end, the Grosky effect measurements are found to underestimate the NMR relaxation times. As suggested by Messer et al. [87], the overall best fit through the experimental data should be drawn through the high temperature tail of the Grosky effect measurements and the low end tail of NMR measurements, since the NMR data was derived by assuming only jumps between two neighboring tetrahedral sites. The diffusion rate calculated from the HQTST approach is found to be in overall good agreement with the

experimental data in the temperature range (180 K - 110 K) of this study. Below 100 K the HQTST rate is predicted to be almost completely flat as a function of temperature, possible as a result of the finite resolution if the CFP. There is also some numerical noise apparent in the HQTST data. While the effective energy of the instanton and the contribution from the free rotation along the CFP could be calculated relatively easily, accurately calculating the CFP vibrational frequencies necessary for the prefactor was found to be extremely difficult. The difficulty was attributed to the lack of precision in the forces provided by VASP, a problem that is magnified when finite difference of forces are considered, as is necessary for estimating the matrix of second derivatives. Instead of performing a costly analysis of the optimal step size for the finite difference scheme, a overall downward slope of the calculated diffusion constant was accepted, as it adheres to common physical intuition, and by keeping in mind the inherent error of DFT and the experiment, the agreement was found to be most acceptable. As a side note, the increased deviation from the experimental data obtained by the Grosky effect measurements may support the hypothesis that the hydrogen diffusion rate at low temperatures are underestimated due to trapping.

4.2.2 H atom diffusion in Pd

Calculation were performed by the *Vienna Ab-initio Simulation Package* (VASP) [35, 36, 37, 38] code. The system was a 4 Pd atoms in the fcc crystal lattice configuration. The Brillouin zone was sampled by a 5x5x5 k-point mesh generated with the Monkhorst-Pack scheme [80] and the kinetic energy cut-off for the plane wave basis functions was 349.9 eV. Ultasoft Vanderbilt pseudopotentials (US-PP) [88] were used and the exchange-correlation part of the potential was PW91 [79]. All calculations were performed spin restrictive.

During the simulation one of the Pd atoms was kept frozen at the ideal lattice coordinates. The optimal site for the H atom was found to be in the octahedral hole, O_h, as is most common for fcc metals. Diffusion of the hydrogen atom was assume to occur between to adjacent octahedral hole, via a tetrahedral hole. Hydrogen diffusion in Pd exhibits inverse isotope effects, that is diffusion of deuterium if faster then hydrogen (protium), even though the former is heavier. The effect has been contributed to the difference in zero-point

t

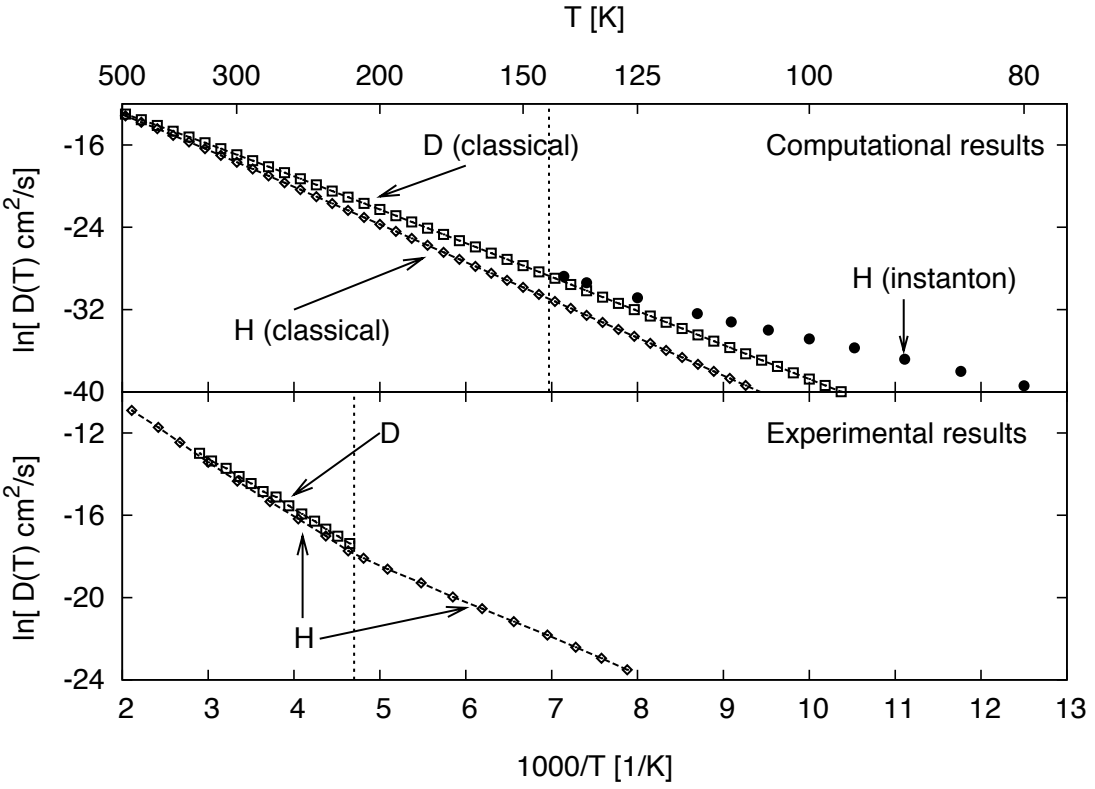

Figure 4.4: Comparison between calculated and experimental diffusion constants for hydrogen diffusion in Pd. The upper panel shows the calculated diffusion constants in the present study. In the classical regime, the inverse isotope effect between hydrogen and deuterium is reproduced. Quantum effects are calculated to be considerable below the crossover temperature,$T_c = 144$ K. The lower panel presents the experimental results from Ref. [89] The experimental crossover temperature is ≈220 K.

energy between the two isotopes in the Pd crystal and reproduced in the classical region.

Table (4.2.2) compares the parameters for Arrhenius, $D(T) = D_o \exp(-\Delta E/k_B T)$, like expression for the diffusion constants, as extracted from the computational and experimental results, Ref. [89]. The activation energies are in general found to be in good agreement with the experimentally extracted results, but the prefactors are underestimated by 1-2 orders of magnitude. It is well known that the potential energy surface for the Pd/H system displays

Table 4.2: Comparison between the calculated and experimental diffusion parameters. The parameters were extracted from a fit to an Arrhenius, $D(T) = D_o \exp(-\Delta E/k_B T)$, equation in the high and low temperature limit from Ref. [89]. The agreement between the calculated and experimental activation energies (ΔE) is generally good, but the calculated prefactors (D_o) are underestimates by 1-2 orders of magnitude. The discrepancy can be attributed to the anharmonic nature of the potential energy surface.

	System	D_o [cm^2/s]	ΔE [eV]
Computational	H (classical)	$7.7 \cdot 10^{-4}$	0.21
	D (classical)	$5.4 \cdot 10^{-4}$	0.21
	H (instanton)	$2.1 \cdot 10^{-7}$	0.17
Experimental	H (classical)	$5.3 \cdot 10^{-3}$	0.23
	D (classical)	$3.7 \cdot 10^{-3}$	0.22
	H (quantum)	$6.1 \cdot 10^{-5}$	0.15

some anharmonic features [90]. The anharmonic nature of the potential energy surface could possibly explain the observed discrepancy between the calculated and experimental crossover temperatures, as well as the diffusion prefactors.

4.3 Hydrogenation of ammonia precursors on Ru(0001) surface

Ammonia is one of the most vital and most produced chemical in the world; in 2004 the worldwide ammonia production was 109 million metric tons. With 80% of the ammonia produced being used by the agricultural industry in the form of artificial fertilizers to generate crops, and the exponential rise in human population, production of ammonia will almost certainly grow in the near future. Ammonia finds widespread usage in the manufacturing, production of high explosive, and in the polymer and textile industries. Additionally, with the advent of increased consciousness regarding environmental issues, avenues are currently being explored utilizing salts of ammonia as hydrogen storage devices and as catalytic reduction agents for removal of nitrogen oxide compounds from diesel engine exhaust.

Ammonia synthesis represents the quintessential heterogeneous catalysis reaction and

has, as such, been extensively studied, both experimentally and theoretically. The reaction mechanism on an iron surface is well characterized and follows a Langmuir-Hinshelwood scheme where both gaseous reactants adsorb and dissociate on the catalyst surface, followed by a stepwise hydrogenation of atomic nitrogen until NH_3 desorbs from the surface. Traditionally the reaction takes place on an iron based catalyst; it has since been recognized that ruthenium is the best elemental catalyst available. Especially at lower temperatures, ruthenium is found to have considerably higher activity. However, higher cost and shorter lifetime of ruthenium based catalysts have largely precluded a general industrial usage over more conventional iron based catalysts.

On the industrial scale, ammonia is synthesized by the Haber-Bosch process, where molecular nitrogen (N_2) and hydrogen (H_2) are reacted on a metal catalyst surface at elevated temperature ($\sim$700 K) and pressure ($\sim$200 atm). Although an effective catalyst is used, the Haber-Bosch process consumes vast amounts of energy, and ammonia production constitutes more than 1% of the global energy consumption. Since extreme reaction conditions are needed for activation of the very strong nitrogen-nitrogen triple bond, the initial dissociative adsorption of N_2 is commonly acknowledged as the rate determining step at the industrial scale. Nature, through the course of evolution, has produced microorganisms capable of producing ammonia via nitrogen fixation, catalyzed by the enzyme nitrogenase, at atmospheric conditions. The active site on the enzyme it proposed to be a $MoFe_7S_9$ cluster and unlike the Haber-Bosch process where the energetic nitrogen triple bond is broken, the enzyme directly hydrogenates the N_2 molecule.

Recently, Tautermann et al. [91] have published calculated rate constants for all the nitrogen hydrogenation steps on Ru(0001). In Ref. [91] a reduced dimensionality potential energy surface was used where the energy and forces were generated by a plane wave based DFT code using the RPBE functional [92]. The system size was a 2x3, two layer unit cell, constituting 12 Ru atoms that were kept fixed at the experimental lattice coordinates. The rate constants were subsequently calculated within transition state theory and quantum mechanical effects were accounted for by small curvature corrections (SCT) to the classical results, where the reaction path was traced by the Page-McIver method [93]. Some deviations from the classical Arrhenius behavior was found for the first two hydrogenation steps,

especially for the second step. The lack of quantum mechanical enhancement of the rate from the third and final step was attributed to the mass of the ammonia molecule.

Little difference has been found in classical reaction rates between steps and terraces on Ru(0001) [94]. For later comparison with results from Ref. [91] terraces are considered exclusively in the present study.

In the two following subsections, the reaction rates for the first two hydrogenation steps will be presented. Forces and energies were generated by *Vienna Ab-initio Simulation Package* (VASP) [35, 36, 37, 38], one of the most popular and powerful DFT [95] code available to date. VASP solves the Kohn-Sham equations [77] self-consistently for a given exchange-correlation functional, using periodic boundary conditions with plane-wave basis set and a generalized Vanderbilt ultrasoft pseudopotential (US-PP) [88] or projector augmented wave (PAW) [78] formalism to describe the interaction between ion cores and electrons. In the present study ultrasoft pseudopotentials were used.

4.3.1 $N_{\text{ads}} + H_{\text{ads}}$

Results are presented for the rate of reaction for the first hydrogenation step of nitrogen on a Ru(0001) surface. The Ru substrate was modeled by a three layer slap, with each layer containing 8 atoms. With the substrate and the adsorbed atoms the system contains 26 atoms. All Ru atoms were kept fixed at the experimental lattice configuration throughout the simulation, the two lattice parameters are given as $a = 2.706$ Å and $c = 4.282$ Å [81]. A vacuum layer of 11 Å was placed above the surface layer. The hydrogen atoms was found to adsorb at a fcc surface site and the nitrogen atom at a hcp surface site, in accordance with other studies [94, 96, 91]. The Brillouin zone was sampled with a 2x1x1 k-point mesh generated with the Monkhorst-Pack scheme [80] and the exchange-correlation functional was represented by the RPBE (revised Perdew-Burke-Ernzerhof) functional [92]. Preliminary checking indicated that the current k-point sampling resulted in adequately accurate forces and energy. As mentioned before, the Kohn-Sham equations were iteratively solved with the *Vienna Ab-initio Simulation Package* (VASP) [35, 36, 37, 38] DFT code.

The classical reaction barrier height was calculated to be 1.11 eV, in good agreement

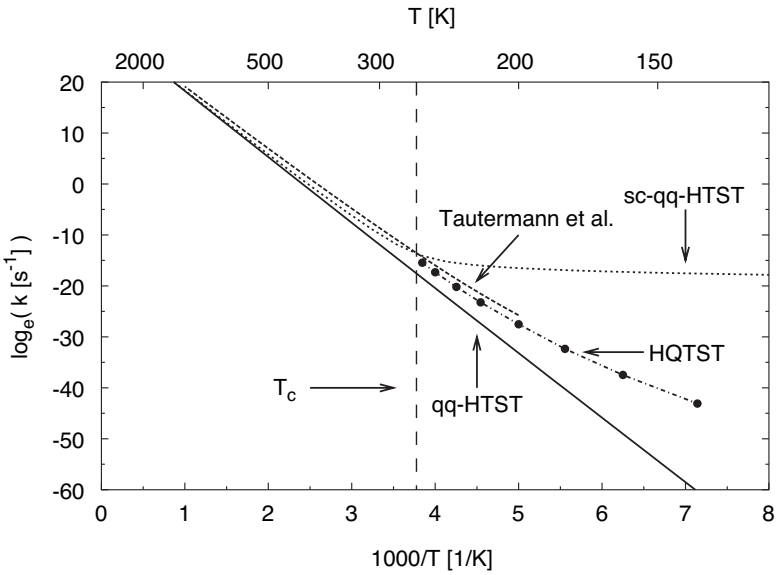

Figure 4.5: The rate constant as a function of temperature for the first hydrogenation step in the stepwise hydrogenation of nitrogen in ammonia production on a Ru(0001) surface. Comparison is made the recently published results by Tautermann et al. [91] using a small curvature tunneling correction (SCT) to the classical rate. A general good agreement is found above the crossover temperature between the SCT results and the semi-classically corrected [97] classical rate suggested by Fermann et al. (sc-qq-HTST) from the present study. The discrepancy can be explained by the slightly different barrier height between the two computational approaches employed. Below the crossover temperature the consistency between the SCT and HQTST rates is also favorable, over the range of the SCT results, the ratio of the two remains about constant. The crossover temperature was calculated to be $T_c = 263$ K. The line through the HQTST results is a guide for the eye only.

with the 1.07 eV value recently published by Tautermann et al. [91]. In the present study, the CFP was represented by 8 system replicas (and 8 shadow replicas) at the highest temperatures and up to 29 movable replicas at the lower temperature values. More replicas were needed at the lower temperature end to adequately describe the elongated CFP. The electronic structure was rigorously converged to obtain accurate forces for estimating the necessary second derivatives of the potential. Starting at a given temperature with a previously converged CFP from a higher temperature, resulted in a speedy convergence to the instanton, usually requiring only about 700 force calculations per movable replica. As each replicas can be efficiently parallelized over a set of processors, this does not constitute a

considerable computational task.

The results for the rate constant calculations are depicted in Fig. (4.5). The HQTST rate is compared to the results from Tautermann et al. [91]. Compared to the quasi-quantum rate constant (qq-HTST), considerable quantum effects are already present, even well about the crossover temperature. Quantum mechanical enhancement of the rate will though be minuscule at industrial relevant conditions. The small curvature corrected (SCT) rate (see Sec. 1.3) from Ref. [91] is found to be slightly higher at the high temperature end, since the barrier height reported there is smaller than the present one. Over the temperature range reported in Ref. [91], the SCT and HQTST results compare remarkably well, maintaining about the same slope throughout.

Preliminary results indicate that it is necessary to include the relaxation of N in the simulation; restricting the movement of the N atoms results in severe underestimation of the tunneling effect. In general, keeping the substrate fixed, is found to result in a good approximation to the reaction rate, especially at temperatures close to the crossover temperature. Only around 140 K will allowing the surface atoms to relax cause deviation from the results where all surface atoms as kept frozen, indicating the the tunneling path has moved away from the classical MEP.

4.3.2 $NH_{\text{ads}} + H_{\text{ads}}$

In the present study, a two layer, 4x2 rectangular cell was used (giving total of 16 Ru atoms) where the Ru atoms were kept fixed at the experimental geometry (a = 2.706 Å and c = 4.282 Å) [81] during all calculations. A vacuum layer of 11 Å was placed above the surface layer. The RPBE (revised Perdew-Burke-Ernzerhof) [92] exchange-correlation functional was used and the Kohn-Sham orbitals were expanded in a plane-wave basis set with kinetic energy up to 25.68 Ry (349.4 eV). The Brillouin zone was sampled with a (2N x N x 1) k-point mesh generated with Monkhorst-Pack scheme [80] with N= $1, 2, 3$. Convergence with respect to the k-point sampling was reached with N = 3. For temperatures ranging from 250 K - 140 K, 15 system replicas (with additional 15 shadow replicas) were found to be sufficient to describe the discrete CFP. At lower temperatures however, the

Figure 4.6: Three possible reaction paths for the NH +H reaction on a Ru(0001) surface. The topmost panel, (a), shows the path studied. The configuration on the left is the initial state with the NH molecular fragment at a hcp site and the reacting H atoms as a fcc site. The middle depicts the actual reaction path, where only the movements of the reacting hydrogen atoms is showed. There is a slight extra movement in the path since the reacting H atoms kicked the resulting NH_2 fragment to a equivalent bridge site. Because of the imposed boundary condition the NH_2 moves to a neighboring bridge site. The rightmost figure is the finial product, with a NH_2 fragment at a bridge site. The middle panel, (b), shows another possible reaction path where the reacting hydrogen atoms start at a fcc site situated further away than the one in panel (a). The saddle point along path (b) is only slightly higher than for the path in panel (a), ca. 0.08 eV. The bottom panel, (c), shows the reaction hydrogen atoms starting at an intermediate hcp site. The reaction actually progresses through the same saddle point as the reaction path in (a).

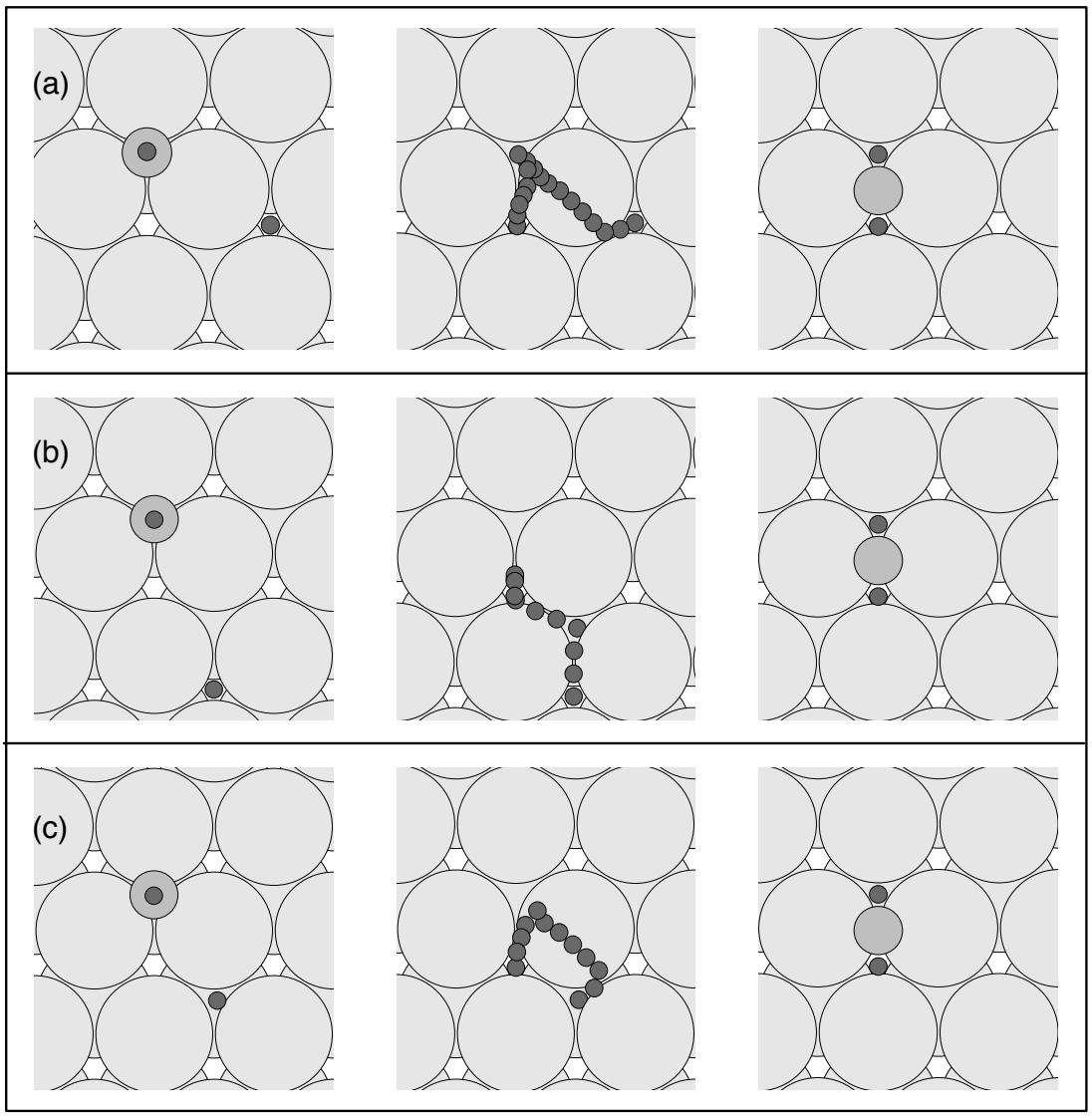
(a)
(b)
(c)

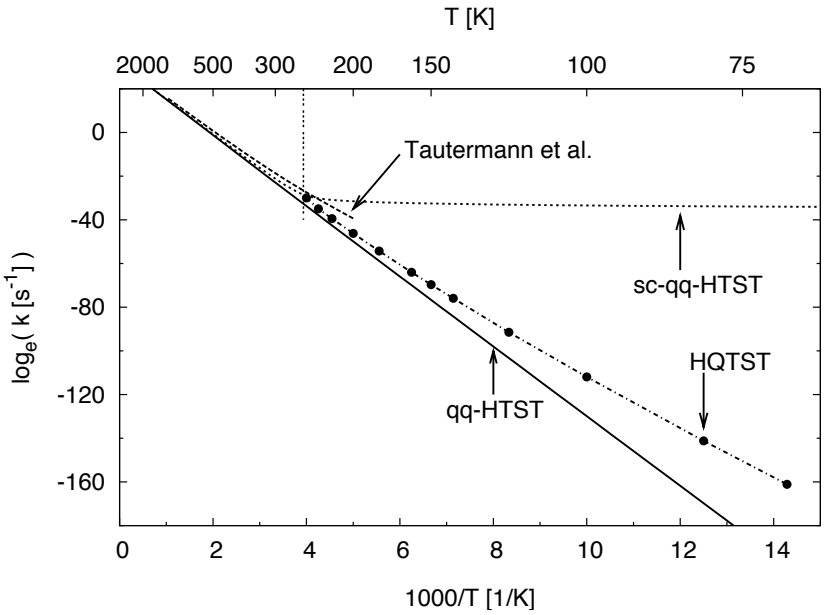

Figure 4.7: The rate constant as a function of temperature for the second hydrogenation step in the stepwise hydrogenation of nitrogen in ammonia production on a Ru(0001) surface. Comparison between the HQTST (and quasi-quantum) results in the present study and the SCT results from Ref. [91] are shown. In the high temperature limit there is good agreement between the qq-HTST, sc-qq-HTST and the SCT indicating the two different potential energy surface are represented similarly. The line through the HQTST results is a guide for the eye only. The crossover temperature was calculated to be 254.1 K and is represented by the horizontal dotted line.

number of system replicas was increased to 29 (and 29 shadow replicas) to ensure sufficient resolution of the Feynman path. Derivatives were determined by a $1.0 \cdot 10^{-3}$ Å step size and the electronic structure was rigorously converged by requiring the energy difference between two sequential iteration to be less than $1.0 \cdot 10^{-8}$ eV. The CFP was considered to have converged to the instanton if the maximum value of all force components was lower than $3.0 \cdot 10^{-4}$ eV/Å. Starting from a previously converged instanton at a higher temperature, convergence was typically achieved in about 500 - 800 force calculation, per movable image. As pointed out previously by Zhang et al. [96], there exist many different reaction paths for each of the hydrogenation steps, all with similarly energetic saddle points. Three different pathways for the second hydrogenation step are shown in Fig. (4.3.2). Similar

Table 4.3: Structural parameters for the reacting species in $NH + H \rightarrow NH_2$. Adsorption sites are given and for the transition state the magnitude of the imaginary frequency is listed. Numbers in parenthesis are from Ref. [91]. Distances are given in Å.

Species	Site or imag. freq.	Adsorption height	N-H bond length
H	fcc	1.08 (1.08)	-
NH	hcp	1.25 (1.30)	1.02 (1.03)
NH_2	bridge	1.64 (1.67)	1.02 (1.02)
TS($NH \rightarrow NH_2$)	1111 (1150) cm^{-1}	1.34 (1.39)	1.38 (1.44)

pathways exist for the first step, the only difference is that a single N atom is placed for the NH molecular fragment. In Fig. (4.3.2) paths (a) and (c) react through the same transition state. Starting with the configuration in panel (b), the reacting H atoms could conceivably travel along the reaction path depicted in the middle figure of panel (b) or along the reaction coordinate for path (c). The energy of the initial state increases as the reacting H atom is moved closer to the NH molecular fragment. Evidently, the increased proximity induces repulsive interactions between the reacting species. The energy difference is slight, with the initial configuration in panel (b) in Fig. (4.3.2) about 0.06 eV lower in energy than the starting configuration in panel (a). On the other hand, the reaction barrier is higher by ca. 0.08 eV for the path in panel (b) and it is considerably longer than in the path in panel (a). Both effects act as to favor the path in (a), especially at lower temperatures. The initial configuration in panel (c) is much higher in energy ($\sim$0.2 eV) and is not considered to be relevant in the present study. In this study, and in accordance with Ref. [91], reaction path (a) was focused on exclusively. At industrial conditions, all three pathways most likely will be in active competition. The reactive barrier for the path under study was found to be 1.39 eV (1.36 eV), as compared to 1.35 eV (1.31 eV) in Ref. [91], the numbers in the parenthesis are the zero-point energy corrected barrier heights. The difference can be attributed to the differences in the computational setup. In Ref. [91], a three dimensional potential energy surface was used to estimate the reaction rate constant

for the hydrogenation step. The reaction rate constant was calculated within the harmonic transition state theory (HTST). The small curvature tunneling correction (SCT) scheme, see Sec. (1.3), was used to incorporate quantal effects, such as zero-point energy, barrier penetration via tunneling and nonclassical barrier reflection. As is evident from Fig. (4.3.2), the reaction path is quite curved and the nitrogen atom moves slightly out of the coordinate range specified by the three dimensional potential energy employed in Ref. [91]. Fixing the nitrogen atom is therefore necessary. To compensate, Tautermann et al. introduce a reduced mass for the reacting hydrogen atom by considering the magnitude of the imaginary vibrational frequency at the saddle point in the reduced, three dimensional system and the full system.

In Fig. (4.7), a comparison between the HQTST rate, as calculated in the present study, Sec. (1.5), and the results presented in Ref. [91] is shown. In addition, to estimate the magnitude of including quantum mechanical effects in the rate, results based on the quasi-quantum rate and the semi-classical correction suggested by Fermann et al. [97] are showed as well. Quantum effects are found to be completely repressed at industrial relevant conditions, as could have been expected. But right below the crossover temperature, including effects from quantum mechanical tunneling enhances the reaction rates by about an order of an magnitude.

Because Ref. [91] employes both a different potential energy surface as well as a different method for the quantal effects, a direct comparison between the HQTST rate and the results reported therein is not feasible. Close to the crossover temperature, the discrepancy between the two sets of results is found to be small, presumably due to the different representations of the potential energy surfaces. According to Ref. [91] the barrier is slightly lower, hence the rate is higher. As the temperature is lowered further, the results from Ref. [91] and the present HQTST results increasingly diverge, in line with what has been observed in previous comparison between the two methods. The cause is likely the harmonic expansion centered around the classical reaction path employed in the small curvature approximation. As before, the semi-classical approximation (sc-qq-HTST) suggested by Fermann et. al [97] completely fails below the crossover temperature. However, close to the crossover temperature, the HQTST rate and the sc-qq-HTST appear to agree reasonably well.

Chapter 5

CONCLUSION AND DISCUSSION

This thesis presents an implementation of instanton theory [22, 25, 6] - a harmonic quantum transition state theory (HQTST) - that makes it possible to calculate quantum mechanical rate constants with relatively small computational effort. The method is efficient enough to use atomic forces directly obtained from first principles methods, without needing to develop analytical potential energy surfaces. The method is applied to several test problems where more accurate, higher level quantum rate theories can be applied, as well as to simulations of hydrogen atom diffusion and H_2 adsorption/desorption where atomic forces are obtained from density functional theory (DFT) or semi-empirical methods. The basic question that is addressed is how low the temperature needs to be in these systems for quantum mechanical tunneling of hydrogen atoms to become the dominant transition mechanism.

Previous calculations of quantum rate constants have in most cases relied on the development of analytical potential energy surfaces and subsequent propagation of quantum mechanical wave packets to find the reaction rate. Such an approach is limited to systems with only very few degrees of freedom, at most six, both because of the tedium and cost in developing the potential energy surface and because of the exponential scaling of the computational effort in the wave packet calculations. In previous applications of instanton theory, which is a statistical theory that avoids the need to calculate quantum dynamics, the problem of finding the instantons has usually been approached by identifying periodic, classical orbits on the inverted potential energy surface, an approach that is, again, only applicable to systems with few degrees of freedom [27, 98, 99, 100]. The methodology that is presented here, however, can be applied to systems with hundreds of degrees of freedom even when computationally demanding, first principles methods are used to evaluate the atomic forces. The approach takes advantage of the analogy between instanton theory and

classical harmonic transition state theory (HTST), in particular the fact that the instanton is a saddle point on an effective, quantum mechanical energy surface that results from the Feynman path integral formulation of quantum statistical mechanics [26, 28, 10]. There, the quantum mechanical delocalization of the system is described by creating several replicas of the system. Corresponding atoms in the replicas are connected with a spring interaction that depends on temperature [101, 9, 23]. The lower the temperature, the looser the springs and greater the quantum delocalization. The total number of degrees of freedom in this path integral construction is 3NP in three dimensions, where N is the number of atoms and P the number of system replicas. The dimensionality of the effective quantum mechanical energy surface can be very high since N is on the order of 100 and P is 10 to 50 for systems and conditions that are commonly used in simulation studies in condensed matter chemistry and physics. A recently developed method, the minimum mode method [30, 32, 31], for finding saddle points on high dimensional surfaces without the need for second derivatives and knowledge of the final state of the transition makes the search for the instanton practical even for such a large number of degrees of freedom. The calculation can easily be divided up and run on several computers simultaneously either by parallel execution and/or distributed computing. The calculations typically require on the order of a few hundred force evaluations per system replica at a given temperature.

Application of the instanton method to simple test problems with one or two degrees of freedom, where the exact quantum mechanical rate constant can be evaluated, indicate that the approximations on which the instanton theory is based hold well in systems of chemical interest and that the calculated rate constants are within a factor of two of the exact value. An application to a large test problem, the desorption of hydrogen molecules from a Cu(110) surface, where full quantum free energy calculations have been performed previously [10], also indicates that instanton theory provides a good approximation for the rate constant in that case.

An application of the instanton method to hydrogen desorption from ammoniaborane, H_3BHN_3, a promising hydrogen storage material, shows that tunneling of hydrogen atoms is the dominant transition mechanism at 400 K, the temperature where hydrogen desorption is experimentally observed to occur. The rate calculation with instanton theory which includes

tunneling is 300 times larger than the rate constant evaluated from quasi-quantum TST, an approximation that includes zero point quantum effects but not tunneling. In each case the AM1 semi-empirical method was used to evaluate the atomic forces. The semiclassical small curvature tunneling (SCT) [13, 14, 15] approximation was found to overestimate the rate constant in this case by nearly a factor of 10.

Calculations of the diffusion of hydrogen atoms in metals were also performed using DFT with a gradient dependent PW91 functional to evaluate the atomic forces. For Ta and Pd in particular, experimental data has shown clear changes in the effective activation energy as the temperature is lowered through a fairly narrow transition interval. In the case of Ta, the instanton calculations give very good agreement with the measured diffusion at low temperature, for both the activation energy and prefactor, supporting the interpretation that quantum mechanical tunneling is the dominant diffusion mechanism. For H in Pd, the calculated activation energy agrees well with the measured one but the calculated prefactor is too large by an order of magnitude, possibly due to anharmonic effects.

Finally, calculations were performed on the rate of two slow, elementary steps in the formation of ammonia on the Ru(0001) surface: N+H→NH and NH+H→NH_2. While industrial production of ammonia takes place at a high temperature where quantum tunneling of hydrogen atoms is not important, the project here was part of a larger theoretical study on the possibility of forming ammonia electrochemically at room temperature. The question was how important tunneling of the hydrogen atoms would be for such conditions. The instanton method shows that that tunneling only becomes important below room temperature; the best estimate of the crossover temperature is around 250 K. This system was used for several tests regarding the importance of including various degrees of freedom in the instanton calculations, ranging from calculations where only the adsorbed hydrogen atom could move to calculations where the adsorbed atoms could all move, as well as the top layer of the metal crystal - a DFT/instanton calculation involving a total of 26 atoms, including 10 movable atoms. Just below T_c, it turned out to be important to include the relaxation of the N-atom in addition to that of the H-atoms, but the relaxation of the surface atoms did not affect the rate until the temperature had been reduced to half the crossover temperature.

A troublesome fact regarding the instanton method is that the formalism becomes un-

defined over the quantum-classical crossover temperature [6]. This precludes estimation of the rate constant at higher temperatures, even though quantum mechanical effects may be present. While rates at cryogenic conditions can be important in astrochemistry and reactions in the interstellar medium, the higher temperature values of the rate constant are usually of greater interest when studying more common chemical events. A *modus operandi* for extending the instanton method above the crossover temperature or combining it with a simpler, more approximate method would be highly valuable and worth exploring.

A particularly simple and attractive scheme would be to obtain the rate constant above the crossover temperature by the semi-classical method as suggested by Fermann et al. [97]. Since the Fermann correction breaks down shortly after the temperature decreases below the crossover temperature, instanton rate theory would provide the rate constant in the low temperature region. Calculating the rate based on Fermann's correction to HTST is as expensive as the HTST rate calculation. Another possibility would be to combine the instanton results with results obtained by the small curvature approximation (SCT). However, applications of the small curvature approximation in many dimensions is much less tractable.

Another, perhaps more consistent, approach would be to consider the CFP as a classical entity. The saddle point could be found as usual, and then dynamical corrections performed to access the rate constant at temperatures both above and below the crossover temperature. This avenue has not been explored but yet, but is similar in spirit to the method suggested by Craig et al. [102, 103, 104]. How to treat the quantum mechanical zero-mode (related to the free rotation along the CFP) within this framework remains an open question.

The diffusion of different isotopes of hydrogen can be easily measured with great accuracy because of relatively large atomic mass ratios. The diffusion of the isotope would constitute a perfect test for the instanton method. However, since the curvature of the potential surfaces of the three isotopes is approximately the same, the crossover temperature is reduced for deuterium and tritium as the square root of the mass ratio between the two nuclei. This severely reduces the temperature range where instantons for all isotopes are defined. In this case, it would be critical to calculate the rate above the crossover temperature in a manner consistent with the instanton framework.

As future projects, implementation in other *ab initio* codes are planned. Arrangements have already been made for including the instanton method into the ADF (Amsterdam Density Functional) program suite [105]. Some lingering interest for similar plans regarding CP2K [106] and NWChem [107] remain.

BIBLIOGRAPHY

[1] J. C. Keck, J. Chem. Phys. **32**, 1035 (1960).

[2] J. C. Keck, Adv. Chem. Phys. **13**, 85 (1967).

[3] G. H. Jóhannesson and H. Jónsson, J. Chem. Phys. **115**, 9644 (2001).

[4] T. Bligaard and H. Jónsson, Comp. Phys. Commun. **169**, 284 (2005).

[5] R. P. Feynman and A. R. Hibbs, *Quantum Mechanics and Path Integrals* (McGraw-Hill Companies, New York, 1965).

[6] M. J. Gillan, J. Phys. C: Solid State Phys **20**, 3621 (1987).

[7] G. A. Voth, D. Chandler, and W. H. Miller, J. Chem. Phys. **91**, 7749 (1989).

[8] M. Messina, G. K. Schenter, and B. C. Garrett, J. Chem. Phys. **98**, 8526 (1993).

[9] G. Mills, G. K. Schenter, D. E. Makarov, and H. Jónsson, Chem. Phys. Lett. **278**, 91 (1997).

[10] G. Mills, Ph.D. thesis, University of Washington, 1996.

[11] G. Mills, H. Jónsson, and G. K. Schenter, Surf. Sci. **324**, 305 (1995).

[12] D. A. McQuarrie, *Statistical Mechanics* (University Science Books, Sausalito, California, 2000).

[13] R. T. Skodje and D. G. Truhlar, J. Chem. Phys. **77**, 5955 (1982).

[14] R. T. Skodje and D. G. Truhlar, J. Phys. Chem. **85**, 3019 (1981).

[15] D. G. Truhlar, A. D. Isaacson, and B. C. Garrett, in *Theory of Chemical Reaction Dynamic*, edited by M. Baer (CRC Press, Florida, 1985), Vol. 4, Chap. 2, pp. 66–129.

[16] L. Brillouin, Comptes Rendus **183**, 24 (1926).

[17] H. A. Kramers, Zeits. f. Phys. **39**, 828 (1926).

[18] G. Wentzel, Zeits. f. Phys. **38**, 518 (1926).

[19] R. A. Marcus and M. E. Coltrin, J. Chem. Phys. **67**, 2609 (1977).

[20] H. Hratchian and H. Schlegel, Journal of Chemical Theory and Computation **1**, 61 (2005).

[21] H. Jónsson, G. Mills, and K. W. Jacobsen, in *Classical and quantum dynamics in condensed phase simulations*, edited by B. J. Berne, G. Ciccotti, and D. F. Coker (World Scientific Publishing Co., Singapore, 1998), p. 385.

[22] S. Coleman, Phys. Rev. D **15**, 2929 (1977).

[23] D. Chandler and P. G. Wolynes, J. Chem. Phys. **74**, 4078 (1981).

[24] M. Messina, G. K. Schenter, and B. C. Garrett, J. Chem. Phys. **103**, 3430 (1995).

[25] W. H. Miller, J. Chem. Phys. **62**, 1899 (1975).

[26] V. A. Benderskii, S. Y. Grebenshchikov, E. V. Vetoshkin, G. V. Mil'nikov, and D. E. Makarov, J. Phys. Chem. **98**, 3300 (1994).

[27] V. A. Benderskii, D. E. Makarov, and C. A. Wright, *Chemical Dynamics at Low Temperatures*, Vol. LXXXVIII of *Advances in Chemical Physics* (Wiley, New York, 1994).

[28] D. E. Makarov and M. Topaler, Phys. Rev. E **52**, 178 (1995).

[29] G. Mills, G. K. Schenter, D. E. Makarov, and H. Jónsson, in *Classical and quantum dynamics in condensed phase simulations*, edited by B. J. Berne, G. Ciccotti, and D. F. Coker (World Scientific Publishing Co., Singapore, 1998), p. 405.

[30] G. Henkelman and H. Jónsson, J. Chem. Phys. **111**, 7010 (1999).

[31] G. Henkelman, G. Jóhannesson, and H. Jónsson, in *Methods for Finding Saddle Points and Minimum Energy Paths*, edited by S. D. Schwartz (Kluwer Academic Publishers, Dordrecht, The Netherlands, 2000), pp. 269–300.

[32] R. A. Olsen, G. J. Kroes, G. Henkelman, A. Arnaldsson, and H. Jónsson, J. Chem. Phys. **121**, 9776 (2004).

[33] G. Henkelman and H. Jónsson, J. Chem. Phys. **113**, 9978 (2000).

[34] G. Henkelman, B. P. Uberuaga, and H. Jónsson, J. Chem. Phys. **113**, 9901 (2000).

[35] G. Kresse and J. Hafner, Phys. Rev. B **47**, 558 (1993).

[36] G. Kresse and J. Hafner, Phys. Rev. B **49**, 14251 (1994).

[37] G. Kresse and J. Furthmüller, Comp. Mater. Sci. **6**, 15 (1996).

[38] G. Kresse and J. Furthmüller, Phys. Rev. B **54**, 11169 (1996).

[39] R. Malek and N. Mousseau, Phys. Rev. E **62**, 7723 (2000).

[40] C. Lanczos, *Applied Analysis* (Dover, New York, 1988).

[41] G. H. Golub and C. F. V. Loan, in *Matrix Computations*, 2 ed. (Johns Hopkins University Press, Baltimore, MD USA, 1989), p. 480.

[42] M. T. Heath, *Scientific computing: An introductory survey*, *McGraw-Hill series in computer science* (McGraw-Hill Companies, New York, 1997).

[43] C. Eckart, Phys. Rev. **35**, 1303 (1930).

[44] H. S. Johnston, *Gas phase reaction rate theory* (The Ronald Press Company, New York, 1966).

[45] R. P. McRae, G. K. Schenter, B. C. Garrett, G. R. Haynes, G. A. Voth, and G. C. Schatz, J. Chem. Phys. **97**, 7392 (1992).

[46] W. H. Miller, S. D. Schwartz, and J. W. Tromp, J. Chem. Phys. **79**, 4889 (1983).

[47] K. K. Baldridge, M. S. Gordon, R. Steckler, and D. G. Truhlar, J. Phys. Chem. **93**, 5107 (1989).

[48] J. H. Bárdarson, I. Magnusdóttir, G. Gudmundsdóttir, C.-S. Tang, A. Manolescu, and V. Gudmundsson, Phys. Rev. B **70**, 245308 (2004).

[49] V. Gudmundsson, G. Gudmundsdóttir, J. H. Bárdarson, I. Magnusdóttir, C.-S. Tang, and A. Manolescu, Eur. Phys. J. B **45**, 339 (2005).

[50] V. Gudmundsson, Y.-Y. Lin, C.-S. Tang, V. Moldoveanu, J. H. Bárdarson, and A. Manolescu, Phys. Rev. B **71**, 235302 (2005).

[51] G. Alefeld, R. M. Cotts, K. W. Kehr, H. Kronmüller, H. Peisl, A. Seeger, K. Sköld, T. Springer, A. C. Switendick, J. Völkl, F. E. Wagner, H. Wagner, W. E. Wallace, and G. Wortmann, in *Hydrogen in Metals I: Basic Properties*, Vol. 28 of *Topics in Applied Physics*, edited by G. Alefeld and J. Völkl (Springer-Verlag, Germany, 1978).

[52] M. S. Daw and M. I. Baskes, Phys. Rev. B **29**, 6443 (1984).

[53] C. Bae, D. L. Freeman, J. D. Doll, G. Kresse, and J. Hafner, J. Chem. Phys. **113**, 6926 (2000).

[54] I. Affleck, Phys. Rev. Lett. **46**, 388 (1981).

[55] P. Hänggi, P. Talkner, and M. Borkovec, Rev. Mod. Phys. **62**, 251 (1990).

[56] M. Messina, G. K. Schenter, and B. C. Garrett, J. Chem. Phys. **99**, 1674 (1993).

[57] P. Rasmussen, P. Holmblad, H. Christoffersen, P. Taylor, and I. Chorkendorff, Surf. Sci. **287/288**, 79 (1993).

[58] M. F. Somers, R. A. Olsen, and G. J. Kroes (unpublished).

[59] M. F. Somers, R. A. Olsen, H. F. Busnengo, E. J. Baerends, and G. J. Kroes, J. Chem. Phys. **121**, 11379 (2004).

[60] R. A. Olsen, H. F. Busnengo, A. Salin, M. F. Somers, G. J. Kroes, and E. J. Baerends, J. Chem. Phys. **116**, 3841 (2002).

[61] H. F. Busnengo, A. Salin, , and W. Dong, J. Chem. Phys. **112**, 7641 (2000).

[62] G. Wolf, J. Baumann, F. Baitalow, and F. P. Hoffmann, Thermochimica Acta **343**, 19 (2000).

[63] F. Baitalow, J. Baumann, G. Wolf, K. Jaenicke-Rößler, and G. Leitner, Thermochimica Acta **391**, 159 (2002).

[64] J. Baumann, F. Baitalow, and G. Wolf, Thermochimica Acta **430**, 9 (2005).

[65] M. Bluhm, M. Bradley, R. Butterick, U. Kusari, and L. Sneddon, J. Am. Chem. Soc. **128**, 7748 (2006).

[66] Q. S. Li, J. Zhang, and S. Zhang, Chem. Phys. Lett. **404**, 100 (2005).

[67] A. G. Baboul, L. A. Curtiss, P. C. Redfern, and K. Raghavachari, J. Chem. Phys. **110**, 7650 (1999).

[68] P. J. Stephens, F. J. Devlin, C. F. Chabalowski, and M. J. Frisch, J. Phys. Chem. **98**, 11623 (1994).

[69] A. D. Becke, J. Chem. Phys. **98**, 5648 (1993).

[70] C. T. Lee, W. T. Yang, and R. G. Parr, Phys. Rev. B **37**, 785 (1988).

[71] M. J. S. Dewar and D. M. Storch, J. Am. Chem. Soc. **107**, 3898 (1985).

[72] J. J. P. Stewart, I. Rossi, W.-P. Hu, G. C. Lynch, Y.-P. Liu, Y.-Y. Chuang, J. Li, C. J. Cramer, P. L. Fast, and D. G. Truhlar, MOPAC version 5.09mn, University of Minnesota, Minneapolis, 1999.

[73] J. C. Corchado, Y.-Y. Chuang, P. L. Fast, W.-P. Hu, Y.-P. Liu, G. C. Lynch, K. A. Nguyen, C. F. Jackels, A. F. Ramos, B. A. Ellingson, B. J. Lynch, V. S. Melissas, J. Villa, I. Rossi, E. L. Coitino, J. Pu, T. V. Albu, R. Steckler, B. C. Garrett, A. D. Isaacson, and D. G. Truhlar, POLYRATE version 9.4.1, University of Minnesota, Minneapolis, 2006.

[74] G. K. Schenter, is gratefully acknowledged for providing the CVT/SCT POLYRATE results. (unpublished).

[75] T. Schober, H. Wenzl, E. Wicke, H. Brodowsky, B. Baranowsky, R. Wiswall, R. Waswall, B. Stritzker, H. Wühl, H. Wipf, and C. A. Wert, in *Hydrogen in Metals II: Application-Oriented Properites: Application-Oriented Properites*, Vol. 29 of *Topics in Applied Physics*, edited by G. Alefeld and J. Völkl (Springer-Verlag, Germany, 1978).

[76] R. G. Barnes, P. Dantzer, H. Grabert, D. K. Ross, H. R. S. H. Vehoff, and H. Wipf, in *Hydrogen in Metals III: Properties and Applications*, Vol. 73 of *Topics in Applied Physics*, edited by H. Wipf (Springer-Verlag, Germany, 1997).

[77] W. Kohn and L. J. Sham, Phys. Rev. **140**, A1133 (1965).

[78] P. E. Blöchl, Phys. Rev. B **50**, 17953 (1994).

[79] J. P. Perdew and Y. Wang, Phys. Rev. B **45**, 13244 (1992).

[80] H. J. Monkhorst and J. D. Pack, Phys. Rev. B **13**, 5188 (1976).

[81] *Handbook of chemistry and physics*, edited by D. R. Lide (CRC, Boca Raton, New York, 1997).

[82] P. G. Sundell and G. Wahnstrom, Phys. Rev. B **70**, 224301 (2004).

[83] Z. Qi, J. Völkl, R. Lasser, and H. Wenzl, J. Phys. F: Met. Phys. **13**, 2053 (1983).

[84] P. G. Sundell and G. Wahnstrom, Phys. Rev. Lett. **92**, 155901 (2004).

[85] K. W. Kehr, in *Hydrogen in Metals I: Basic Properties*, Vol. 28 of *Topics in Applied Physics*, 1 ed., edited by G. Alefeld and J. Völkl (Springer-Verlag, Germany, 1978), Chap. 8, pp. 202–204.

[86] C. P. Flynn and A. M. Stoneham, Phys. Rev. B **1**, 3966 (1970).

[87] R. Messer, A. Blessing, S. Dais, D. Höpfel, G. Majer, C. Schmidt, A. Seeger, and W. Zag, Zeitschrift für Physikalische Chemie Neue Folge **2**, 61 (1986).

[88] D. Vanderbilt, Phys. Rev. B **41**, 7892 (1990).

[89] Y. Fukai and H. Sugimoto, Advances In Physics **34**, 263 (1985).

[90] M. Kemali, J. E. Totolici, D. K. Ross, and I. Morrison, Phys. Rev. Lett. **84**, 1531 (2000).

[91] C. S. Tautermann, Y. K. Sturdy, and D. C. Clary, J. Catal. **244**, 199 (2006).

[92] B. Hammer, L. B. Hansen, and J. K. Nørskov, Phys. Rev. B **59**, 7413 (1999).

[93] M. Page and J. James W. McIver, J. Chem. Phys. **88**, 922 (1988).

[94] A. Logadottir and J. K. Norskov, J. Catal. **220**, 273 (2003).

[95] P. Hohenberg and W. Kohn, Phys. Rev. **136**, B864 (1964).

[96] C. J. Zhang, M. Lynch, and P. Hu, Surf. Sci. **496**, 221 (2002).

[97] J. T. Fermann and S. Auerbach, J. Chem. Phys. **112**, 6787 (2000).

[98] V. A. Benderskii, V. I. Goldanskii, and D. E. Makarov, Phys. Rep. **233**, 195 (1993).

[99] V. A. Benderskii, S. Y. Grebenshchikov, E. V. Vetoshkin, G. V. Milnikov, and D. E. Makarov, J. Phys. Chem. **98**, 3300 (1994).

[100] S. Chapman, B. C. Garrett, and W. H. Miller, J. Chem. Phys. **63**, 2710 (1975).

[101] J. A. Barker, J. Chem. Phys. **70**, 2914 (1979).

[102] I. R. Craig and D. E. Manolopoulos, J. Chem. Phys. **123**, 034102 (2005).

[103] I. R. Craig and D. E. Manolopoulos, J. Chem. Phys. **122**, 084106 (2005).

[104] I. R. Craig and D. E. Manolopoulos, J. Chem. Phys. **121**, 3368 (2004).

[105] *http://www.scm.com/*, 2007.

[106] *http://cp2k.berlios.de/*, 2007.

[107] *http://www.emsl.pnl.gov/docs/nwchem/nwchem.html*, 2007.

[108] R. C. Egeberg, S. Ullmann, I. Alstrup, C. B. Mullins, and I. Chorkendorff, Surf. Sci. **497**, 183 (2001).

[109] J. T. P. Beebe, D. W.Goodman, B. D. Kay, and J. J. T. Yates, J. Chem. Phys **87**, 2305 (1987).

[110] H. Yang and J. L. Whitten, J. Chem. Phys. **96**, 5529 (1992).

[111] H. S. Bengaard, J. K. Nørskov, J. Sehested, L. P. Nielsen, A. M. Molenbroek, and J. Rostrup-Nielsen, J. Catal. **209**, 365 (2002).

[112] A. D. Johnson, S. P. Daley, A. L. Utz, and S. T. Ceyer, Science **257**, 223 (1992).

[113] S. P. Daley, A. L. Utz, T. R. Trautman, and S. T. Ceyer, J. Am. Chem. Soc. **116**, 6001 (1994).

[114] V. Ledentu, W. Dong, and P. Sautet, J. Am. Chem. Soc. **122**, 1796 (2000).

[115] A. Michaelides, P. Hu, and A. Alavi, J. Chem. Phys. **111**, 1343 (1999).

[116] S. Wright, J. F. Skelly, and A. Hodgson, Faraday Discuss. **117**, 133 (2000).

[117] S. Wright, J. F. Skelly, and A. Hodgson, Chem. Phys. Lett. **364**, 522 (2002).

[118] J. P. Perdew, in *Electronic Structure of Solids*, edited by P. Ziesche and H. Eschrig (Akademie Verlag, Berlin, 1991).

[119] The conjugate-gradient method is an efficient algorithm for optimizing saddle point structures in combination with the nudged elastic band and min-mode following methods (eg. the dimer method). However, the force projections used in these methods can be problematic for a traditional implementation of the conjugate-gradient algorithm because there is no energy consistent with the projected forces. Instead, we use a modified conjugate-gradient method in which line minimizations are done using a single Newton's method iteration. The gradient of the force along the line is evaluated with a finite difference step, and the step size required to zero that force is estimated with a linear approximation. This force-only conjugate-gradient method is recommended for both saddle point finding methods and standard geometry optimizations.

[120] K. Christmann, J. Chem. Phys. **88**, 519 (1979).

[121] J. Greeley and M. Mavrikakis, Surf. Sci. **540**, 215 (2003).

[122] G. Kresse and J. Hafner, Surf. Sci. **459**, 287 (2000).

[123] G. Kresse, Phys. Rev. B **62**, 8295 (2000).

[124] M. Mavrikakis, B. Hammer, and J. K. Nørskov, Phys. Rev. Lett. **81**, 2819 (1998).

[125] G. Henkelman and H. Jónsson, Phys. Rev. Lett. **86**, 664 (2001).

[126] A. Eichler, repeated the methane dissociation on Ir(111) calculations reported in Phys. Rev. Lett. **84**, 664, (2001) and found that the system size effects are largely due to the limitation of the k-point sampling; The converged barrier is approximately 0.7 eV and not 0.3 eV as reported., (Private Communication), 2002.

[127] J. C. Polanyi and Wong, J. Chem. Phys. **51**, 1439 (1969).

[128] M. J. Frisch, G. W. Trucks, H. B. Schlegel, M. A. R. G. E. Scuseria, J. R. Cheeseman, V. G. Zakrzewski, J. J. A. Montgomery, R. E. Stratmann, J. C. Burant, S. Dapprich, J. M. Millam, A. D. Daniels, K. N. Kudin, M. C. Strain, O. Farkas, J. Tomasi, V. Barone, M. Cossi, R. Cammi, B. Mennucci, C. Pomelli, C. Adamo, S. Clifford, J. Ochterski, G. A. Petersson, P. Y. Ayala, Q. Cui, K. Morokuma, D. K. Malick, A. D. Rabuck, K. Raghavachari, J. B. Foresman, J. Cioslowski, J. V. Ortiz, A. G. Baboul, B. B. Stefanov, G. Liu, A. Liashenko, P. Piskorz, I. Komaromi, R. Gomperts, R. L. Martin, D. J. Fox, T. Keith, M. A. Al-Laham, C. Y. Peng, A. Nanayakkara, C. Gonzalez, M. Challacombe, P. M. W. Gill, B. Johnson, W. Chen, M. W. Wong, J. L. Andres, C. Gonzalez, M. Head-Gordon, E. S. Replogle, and J. A. Pople, *Gaussian 98, Revision A.7* (Gaussian, Inc., Pittsburgh PA, 1998).

[129] R. R. Smith, D. R. Killelea, D. F. DelSesto, and A. L. Utz, Science **304**, 992 (2004).

[130] L. B. F. Juurlink, R. R. Smith, D. R. Killelea, and A. L. Utz, Phys. Rev. Lett. **94**, 208303 (2005).

[131] T. Klamroth and P. Saalfrank, J. Chem. Phys. **112**, 10571 (2000).

[132] J. Strömquist, L. Bengtsson, M. Persson, and B. Hammer, Surf. Sci. **397**, 382 (1998).

[133] J. R. Trail, D. M. Bird, M. Persson, and S. Holloway, J. Chem. Phys. **119**, 4539 (2003).

[134] C. L. A. Lamont, B. N. J. Persson, and G. P. Williams, Chem. Phys. Lett. **243**, 429 (1995).

[135] A. Michaelides and P. Hu, Surf. Sci. **437**, 362 (1999).

[136] C. Wert and C. Zener, Phys. Rev. **76**, 1169 (1949).

[137] G. H. Vineyard, J. Phys. Chem. Solids **3**, 121 (1957).

[138] E. Wigner, Trans. Faraday Soc. **34**, 29 (1938).

[139] E. Wigner, Z. Phys. Chem. Abt. B **32**, 203 (1932).

Appendix A

PREVIOUSLY PUBLISHED ARTICLE IN THE JOURNAL OF CHEMICAL PHYSICS

Theoretical calculations of CH_4 and H_2 associative desorption from Ni(111): could subsurface hydrogen play an important role?

by

G. Henkelman[1], A. Arnaldsson[2] and H. Jónsson[3]

Published in *J. Chem. Phys.*, **124**, 044706 (2006)

A.1 Summary

The results of theoretical calculations of associative desorption of CH_4 and H_2 from the Ni(111) surface are presented. Both minimum energy paths and classical dynamics trajectories were generated using density functional theory to estimate the energy and atomic forces. In particular, the recombination of a subsurface H-atom with adsorbed CH_3 (methyl) or H at the surface was studied. The calculations do not show any evidence for enhanced CH_4 formation as the H-atom emerges from the subsurface site. In fact, there is no minimum energy path for such a concerted process on the energy surface. Dynamical trajectories started at the transition state for the H-atom hop from subsurface to surface site also did not lead to direct formation of a methane molecule but rather led to the formation of a thermally excited H-atom and CH_3 group bound to the surface. The formation (as well as rupture) of the H-H and C-H bonds only occurs on the exposed side of a surface Ni atom. The transition states are quite similar for the two molecules, except that in the case of the C-

[1]Department of Chemistry and Biochemistry, The University of Texas at Austin, 1 University Station A5300, Austin, Texas 78712-0165

[2]Department of Chemistry, University of Washington, Box 351700, Seattle, Washington 98195-1700

[3]Department of Chemistry, University of Washington, Box 351700, Seattle, Washington 98195-1700 and Faculty of Science, VR-II, University of Iceland, 107 Reykjavik, Iceland

H bond, the underlying Ni atom rises out of the surface plane by 0.25 Å. Classical dynamics trajectories started at the transition state for desorption of CH_4 show that 15% of the barrier energy, 0.8 eV, is taken up by Ni atom vibrations, while about 60% goes into translation and 20% into vibration of a desorbing CH_4 molecule. The most important vibrational modes, accounting for 90% of the vibrational energy, are the four high frequency CH_4 stretches. By time reversability of the classical trajectories, this means that translational energy is most effective for dissociative adsorption at low energy characteristic of thermal excitations but energy in stretching modes is also important. Quantum mechanical tunneling in CH_4 dissociative adsorption and associative desorption is estimated to be important below 200 K and is, therefore, not expected to play an important role under typical conditions. An unexpected mechanism for the rotation of the adsorbed methyl group was discovered and illustrates strong three-center C-H-Ni contribution to the methyl-surface bonding.

A.2 Introduction

The critical step in the transformation of methane to more valuable chemicals is the dissociative adsorption on the surface of the catalyst to form an adsorbed methyl group, CH_3 and an adsorbed hydrogen atom. Much of the experimental and theoretical work has focused on this step. The most recent and most reliable measurements of the activation energy barrier for dissociative adsorption of CH_4 on Ni(111) give a value of 0.77 ± 0.10 eV [108]. Great care was taken in these measurements to block defects on the surface with unreactive Au atoms and to thermalize the methane gas with the surface. Previous measurements had given a smaller value of 0.55 eV [109].

Theoretical studies of the dissociative adsorption have employed various techniques for describing the energetics and have given estimates of the rate within harmonic transition state theory where the saddle point on the energy surface between the energy minimum corresponding to the methane molecule and the adsorbed methyl group and hydrogen atom gives the activation energy barrier for the transition. Witten and coworkers have used cluster models of the surface and calculated the energetics using Hartree-Fock and configuration interaction (CI) methods [110]. Their best estimate of the activation energy for dissociative adsorption is 0.72 eV. The distance between the C-atom and the closest Ni-atom at

the saddle point is 2.41 Å. Nørskov and coworkers have employed density functional theory methods using both the PW91 and RPBE functional, obtaining activation energies of 0.73 eV and 1.05 eV, respectively [111]. The minimum energy path for dissociative adsorption is, of course, the same as the minimum energy path for associative adsorption. The calculated MEP with the RPBE functional gives an activation energy of 0.4 eV for associative desorption of methane when starting with H-atom and CH_3-group adsorbed on the surface.

A traditional view of surface chemistry assumes that chemical reactions and dissociative chemisorption take place on the outer surface of the catalyst. However, in a series of experiments by Ceyer and coworkers [112, 113] the presence of subsurface hydrogen was shown to increase the efficiency of CH_3 and ethylene hydrogenation on a Ni(111) surface. Two theoretical studies of methane associative desorption have addressed this issue [114, 115]. In both studies, density functional theory (DFT) calculations using the PW91 functional were used to study various pathways for the recombination of the subsurface H-atom and surface adsorbed methyl group. Both groups report an activation energy barrier for the direct recombination process suggested by Ceyer and coworkers but in one case the first order saddle point is reported to be 1.08 eV higher in energy than the initial state [114], while in the other study it is reported to be 1.36 eV higher [115]. The saddle point geometry is reported to be quite unusual in that the C-Ni distance was very large – 2.5 Å in one [114] and 2.2 Å in the other [115]. Typically, the catalysis of a chemical reaction by a transition metal requires the overlap of the half-filled d-electron orbitals on a transition metal atom with the molecular orbitals of the chemical and because of the localized nature of the d-orbitals a typical transition state involves much shorter distances. In both reports it was pointed out that the activation energy barrier for the process starting from surface H- and CH_3 is considerably lower in energy, and the increased reactivity when the Ni catalyst is prepared with subsurface H-atoms is not due to a new reaction pathway but rather the additional energy given to the initial state of the desorption process by driving the H-atoms into subsurface sites [114, 115].

The reactivity of subsurface deuterium on Ni(111) has been studied by Wright, *et al* [116, 117]. Temperature programed desorption experiments of D in both subsurface and

surface sites show enhanced D_2 associative desorption on Ni(111) at 180 K, as compared to a thermal baseline. The angular distribution of desorbing molecules is consistent with subsurface D-atoms surfacing at vacant sites and diffusing on the surface before combining to form D_2. No evidence of a direct recombination process was observed.

Because of the surprising and somewhat inconsistent results reported on the direct recombination pathway involving subsurface hydrogen, we decided to look more carefully into this and apply a rigorous method for finding the minimum energy paths, the nudged elastic band method [11], as well as direct classical dynamics simulations to investigate the possibility of dynamically correlated reactive events.

A.3 Calculations

Density functional theory (DFT) calculations were done with the VASP code [35, 36, 37], using the PW91 functional [118], ultrasoft pseudopotentials [88], and with a plane wave basis set with a 350 eV cutoff. The nickel surface was represented as a four or five layer slab with either a p(2×2) or a p(3×3) cell. The former has four Ni atoms per layer and the latter has nine. Unless otherwise specified, the calculated results given below are for the largest system, five layers with 9 atoms each. The bottom two layers of the slab were constrained to their crystal lattice positions. The Brillouin zone was sampled with a 4×4×1 k-point mesh for the p(2×2) system and a 2×2×1 mesh for the p(3×3) system. The sensitivity of the calculated barriers to spin polarization, plane wave energy cutoff, k-point sampling, system size, and surface relaxation were tested and discussed in appendix A.7.

Classical trajectories were calculated using a combination of DFT evaluation of atomic forces and a verlet algorithm for the dynamics. A small time step size of 0.2 fs was used to ensure energy conservation. Energy barriers were calculated using the nudged elastic band (NEB) method [21] with the climbing-image modification to rigorously converge on saddle points [33, 34]. Once a minimum energy path was found, the dimer method [30] was used to reconverge saddle points after slab geometry had been changed or when calculation parameters had been changed. For these calculations, a force-based conjugate gradients method was used to optimize the geometry [119]. Saddle points and minima were considered converged when the maximum force in every degree of freedom was less than 0.001 eV/Å.

A.4 Results

The lattice constant for bulk nickel was calculated and found to be 3.52 Å, matching the experimental value. Using this lattice constant, slab geometries were generated with 12 Å of vacuum between the top of the slab and the bottom of its periodic image.

Adsorption at the four high symmetry binding sites was studied – the face centered cubic (FCC) and hexagonal close packed (HCP) threefold hollow sites, the bridge site between two surface atoms, and the on-top site above a single nickel atom. Both the H-atom and CH_3 have lowest energy at the FCC threefold site. The calculated binding energy of hydrogen was found to be 2.8 eV, matching the experimental binding energy of 2.77 eV measured by Christmann *et al.* [120], while the binding energy of CH_3 was found to be 1.8 eV. The binding energy at the HCP site is only a few tens of meV lower for both species. For the CH_3 group there is, furthermore, a minimum in the energy surface corresponding to binding on top of a Ni atom but this is 0.3 eV higher than the FCC site, The on-top site was not a local minimum for the hydrogen atom. Neither hydrogen nor methyl showed a local minimum in the energy surface at the bridge site.

Spin polarization is found to be moderately important for binding, decreasing hydrogen's binding energy by 0.1 eV. The bare Ni(111) surface is stabilized with spin polarization to a larger extent than it is with hydrogen bound to it. The reduction in the binding energy as the spin polarization is included is consistent with the fact that the hydrogen bound Ni(111) system has one less unpaired electron than the bare surface.

A.4.1 Subsurface hydrogen

It requires a large amount of energy, 0.6 eV, to drive a H-atom from a surface FCC site to a subsurface site. Figure A.1 shows the minimum energy path for hydrogen resurfacing. The activation energy for resurfacing is small, 0.1 eV. This energy profile is consistent with previous calculations by Michaelides, Hu, and Alavi [115], Ledentu, Dong and Sautet [114], and more recently Greeley and Mavrikakis [121]. The energy difference between the surface and subsurface sites makes it very unlikely to find thermal hydrogen in the subsurface layer; at room temperature and low H coverage, for example, it is 10^{10} times less probable. At

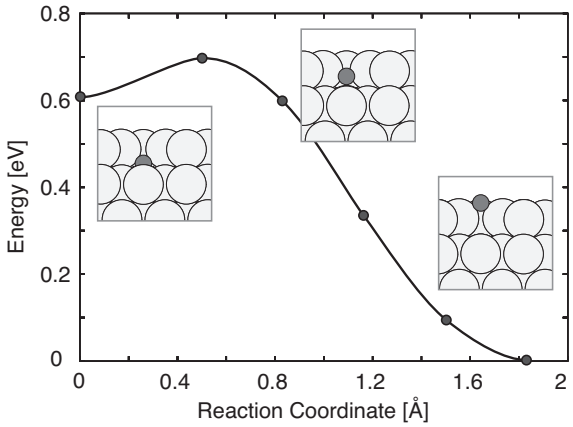

Figure A.1: A hydrogen atom is 0.6 eV higher in energy at a subsurface site than at a FCC hollow site at the surface. Hydrogen can resurface with a small energy barrier of 0.1 eV.

elevated temperature of 600K it is over $100,000$ times less probable. However, when H_2 gas pressure is high and the H-adatom coverage large, the subsurface sites will be populated to some extent and it is of interest to find out to what extent a reaction mechanism involving subsurface H-atoms could contribute to the rate of hydrogenation.

A.4.2 H_2 recombination from Ni(111)

To determine the mechanism of subsurface and surface hydrogen recombination, a nudged elastic band (NEB) is constructed with the initial state consisting of atomic surface hydrogen adsorbed in the preferred FCC hollow site [122, 123] directly above a subsurface hydrogen atom (see Fig. A.2). The final state consists of the H_2 molecule above the Ni(111) surface beyond the interaction distance. Intermediate images along the NEB (see Fig. A.2A) are placed linearly between the initial and final states. The linear interpolation is a good estimate of the direct recombination process. The fact that the NEB converges to a completely different path (see Figs. A.2 and A.3) shows that there is no direct recombination process. Rather, the hydrogen molecule wants to recombine on the exposed side of a nickel atom. In order for the NEB to cross this transition state and satisfy the initial and final state constraints, several intermediate minima appear (automatically) along the band. First, the subsurface hydrogen moves to an adjacent subsurface site (position a in Figs. A.2 and A.3),

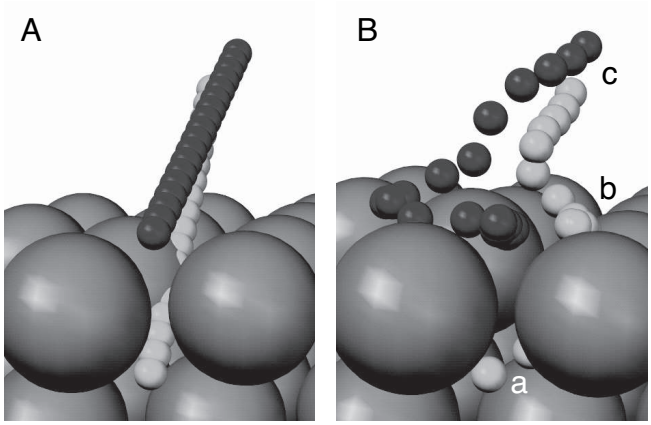

Figure A.2: Initial (A) and relaxed (B) nudged elastic band (NEB) for the process by which subsurface hydrogen combines with surface hydrogen to form a gas phase H_2 molecule above the Ni(111) surface. The initial NEB is a linear interpolation between a relaxed geometry in which the surface hydrogen is adsorbed in the FCC hollow site directly above the subsurface hydrogen and a relaxed geometry in which the H_2 molecule is above the surface beyond the interaction distance. The linearly interpolated initial band is an approximation to a direct recombination process but when the NEB relaxes, no such process is found. Instead, the NEB converges to a much more complicated path in which the subsurface hydrogen (a) first diffuses to a neighboring subsurface site so that it can surface at an unoccupied site. The other hydrogen atom (b) then moves to an adjacent surface site so they can recombine over a surface nickel atom to form H_2 (c).

so that it can emerge at an unoccupied surface site. At this point the two hydrogen atoms are directly across a surface nickel atom (position b in Figs. A.2 and A.3), requiring one hydrogen atom to move to an adjacent surface site so that the H_2 molecule can recombine (position c in Figs. A.2 and A.3) on the exposed site of the surface nickel atom.

Considering the reverse process, a dissociative adsorption reaction can simplify the description. The H_2 molecule dissociates over a surface nickel atom into adjacent surface sites. The rest of the process is simply required to move the hydrogen atoms to the specific final state in which a subsurface hydrogen atom is directly below a hydrogen atom adsorbed in an FCC hollow site.

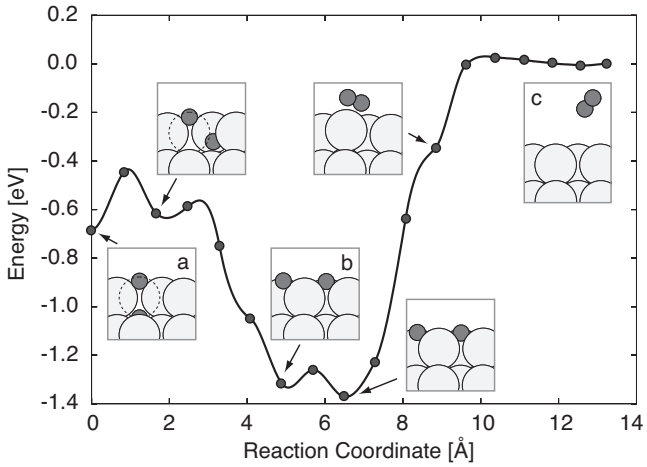

Figure A.3: The minimum energy path for H_2 formation from a subsurface and surface CH_3-group at the Ni(111) surface. The process involves multiple steps. A nudged elastic band (NEB) is constructed with an initial state (a) consisting of a surface hydrogen atom in the lowest energy hollow site on Ni(111) directly above a subsurface hydrogen, and a final state (c) consisting of the H_2 molecule above the metal surface. The NEB does not find a direct recombination mechanism. Instead, the minimum energy path breaks up into a set of processes. First the subsurface hydrogen moves to an adjacent subsurface site, allowing it to surface in an unoccupied site (b). Two hydrogen atoms then move to neighboring surface sites, one in the fcc and the other in the hcp hollow, so that the H_2 molecule (c) can recombine on the exposed side of a Ni surface atom.

A.4.3 CH_4 recombination from Ni(111)

The role of subsurface hydrogen in the recombination process with methyl on Ni(111) was investigated in the same manner as H_2. Figure A.4 shows a converged NEB with an initial state consisting of the methyl group in a hollow site directly above hydrogen in a subsurface site, and a final state with methane above the surface. Just as with H_2 recombination, no direct recombination process with subsurface hydrogen is found. Instead the NEB breaks up into a set of intermediate processes. First the methyl molecule moves to an on top site which allows the subsurface hydrogen atom to surface into an unoccupied hollow site. Then, as with H_2, recombination takes place on the exposed side of a surface nickel atom. Figure A.5 shows this three step recombination process.

These calculations show that there is no direct mechanism for methyl recombination

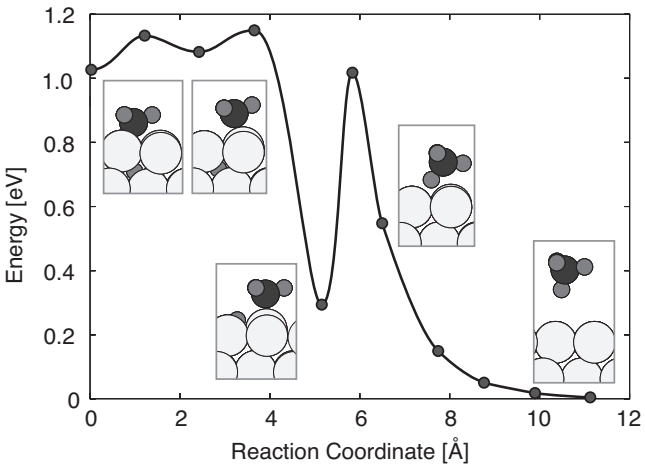

Figure A.4: The minimum energy path for CH_4 formation from a subsurface H-atom and surface H-atoms at the Ni(111) surface. The process involves multiple steps. The first step involves the methyl group hopping to an on-top site. Then the subsurface hydrogen hops to the surface. In the second step, methyl recombines with the surface hydrogen on the exposed surface of the raised Ni atom.

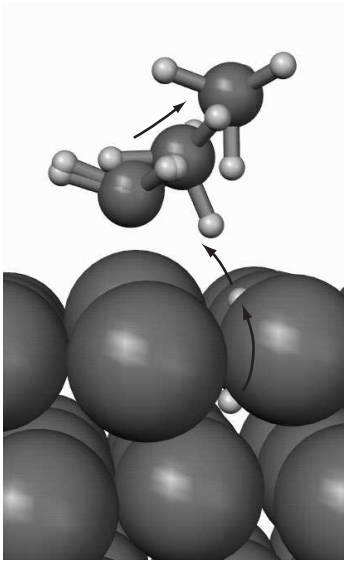

Figure A.5: Graphical representation of the methyl recombination process showing hydrogen resurfacing before recombining with methyl over a nickel surface atom.

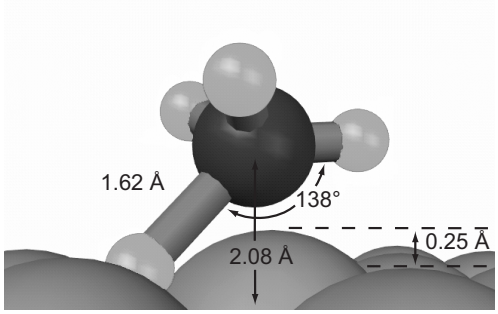

Figure A.6: Geometry of the saddle point for methyl recombination (and dissociation) on the surface of Ni(111). The methyl group and the surface hydrogen react on the exposed side of a single raised surface Ni atom. The Ni atom is raised by 0.25 Å at the transition state. It is likely that the upward displacement of this atom raises the energy of the Ni d-bands to favor bonding with the methyl group and reduce the barrier energy [124].

with subsurface hydrogen. The experimental evidence for the importance of subsurface hydrogen in methane recombination [112] is based on a non-equilibrium experiment in which subsurface hydrogen is induced under high pressure, and surface hydrogen is removed with an atomic Xe beam. The observed increase in reactivity does not result from a new and faster mechanism which opens up with the presence of subsurface H-atoms but it could be caused by the release of (non-thermal) energy stored in the subsurface hydrogen. We have done *ab initio* molecular dynamics simulations to test this. This is described in Sec. A.4.5.

The only theoretically observed mechanism for the dissociative adsorption of methane on Ni(111) involves methyl and hydrogen adsorbing onto the surface. Our most accurate simulation, with a five layer, nine atom per layer Ni(111) slab with three relaxed layers, a 350 eV plane wave energy cutoff, a 2×2×1 Monkhost-Pack k-point mesh, including spin-polarization has a barrier of 0.82 eV. This is in excellent agreement with the barrier of 0.77 eV obtained in recent experiments by Egeberg *et al.* [108].

The transition state geometry, shown in Fig. A.6, shows a remarkable nickel atom surface relaxation of 0.25 Å. The atom rises out of the surface to provide a favorable environment for the hydrogen-methyl bond breaking reaction. This was first observed in calculations of methane dissociation on Ir(111) [125], and then for methane on Ni(111) by Bengaard *et al.* [111]. The surface relaxation is moderately important for the reaction barrier; methane

Table A.1: Energy distribution of the CH_4 molecule as it leaves the Ni(111) surface. A 1 ps *ab initio* molecular dynamics simulation is started from the saddle point for methane dissociation, slightly displaced away from the surface so that the methane molecule desorbs from the surface. The 0.82 eV potential energy at the saddle (0.85 after being displaced) is partitioned into translation, rotation, and internal energy of the CH_4 molecule, and energy that is left behind in the nickel surface.

Energy	Mode or Subsystem
0.13 eV	Ni(111) slab
0.50 eV	CH_4 translation
0.03 eV	CH_4 rotation
0.19 eV	CH_4 vibration
0.85 eV	Total in CH_4 and Ni(111) system

reacting on a frozen surface has a barrier which is 0.14 eV higher. Mavrikakis, Hammer and Nørskov [124] have suggested that a strained surface can raise the energy of the d-band electron energy levels to enhance reactivity. The effect of surface relaxation on the barrier energy is less dramatic than reported in Ref. [125] because the saddle point calculations on Ir(111) were not converged with respect to k-point sampling [126].

A.4.4 Partitioning of CH_4 desorption energy

One of the intriguing possibilities suggested originally from the work of Polanyi [127], is state specific chemistry. If it is known which modes need to be excited in order to make molecules overcome a reaction barrier, there is the possibility of injecting energy into just those modes to enhance reactivity. In order to address this question for the methane dissociative adsorption reaction, a dynamics simulation was run starting from the saddle point for desorption. The molecule was moved a small (0.1 Å) distance away from the surface so that it desorbed from the surface during the simulation. A calculation of 150 fs was sufficient to reach a CH_4-surface distance of 5.3 Å, where the molecule is no longer interacting with the surface at this level of theory. It was then possible, by looking at the velocity of

Table A.2: Vibrational energy of a desorbing CH_4 molecule projected onto the normal modes. An averaging over 200 fs was calculated. This analysis suggests that energy in the symmetric and asymmetric stretch modes can equally enhance dissociative adsorption.

Energy	Mode Description	Frequency
0.021 eV	T2 ($\times$3) asymmetric stretch	3207 cm^{-1}
0.020 eV	A1 ($\times$1) symmetric stretch	3063 cm^{-1}
0.003 eV	E ($\times$2) asymmetric deformation	1551 cm^{-1}
0.002 eV	T2 ($\times$3) asymmetric deformation	1324 cm^{-1}

each atom in the system, to partition the energy into different modes of the system as the molecule leaves the surface. Such a partitioning is shown in Table A.1. The majority (59%) of the saddle point energy goes into translational energy of the methane molecule, making that the most important degree of freedom for dissociative adsorption. A further 22% and 4% of the energy goes into vibrational and rotation energy of CH_4 respectively. The final 15% of the energy is left behind in vibrational motion of the nickel atoms.

It was also possible to subdivide the internal CH_4 energy into its internal modes. To do this, the dynamical simulations were continued for 200 fs after the methane molecule was no longer interacting with the surface. The velocity of the molecule at each time step was projected onto the normal modes of the molecule. The kinetic energy in each mode could then be calculated, and the total energy found by the Virial theorem. The average energy in each mode is reported in Table A.2 along with the calculated frequency, symmetry, degeneracy and description of each mode. The CH_4 normal modes were calculated at the MP2 level using the GAUSSIAN98 software [128]. The frequencies, obtained with MP2 and a local basis set, were significantly closer to the experimental values than could be calculated with the periodic VASP code using a plane wave basis set.

Table A.2 shows that the high frequency stretch modes contain 88% of the vibrational energy of the desorbing CH_4 molecule. This energy is only ca. $1/20^{\text{th}}$ of the vibrational quantum so these classical dynamics cannot be expected to give an accurate description

of the vibrational motion of the CH_4 molecule. Our results do, however, suggest that the stretching modes are more important than the lower frequency deformation modes, and that there could be some enhancement of the dissociation rate if adsorbing methane molecules could be prepared with high energy in the stretching modes, and a high translational kinetic energy. Evidence of this enhancement was recently observed by Smith *et al.* [129] and Juurlink *et al.* [130].

A.4.5 Classical dynamics trajectories of H resurfacing near adsorbed CH_3

It is evident from the NEB calculations, that there does not exist a direct recombination mechanism for a subsurface hydrogen atom and an adsorbed methyl group on the Ni(111) surface. It is however, possible that the energy released (0.6 eV) when a hydrogen atom resurfaces enhances the CH_4 dissociation rate. Since the energy barrier for resurfacing is low (ca. 0.15 eV) we were able to run a classical dynamics simulation at 500 K to see what happens when the hydrogen resurfaces.

An initial geometry was chosen with a subsurface hydrogen atom directly below an adsorbed methyl in the hollow site of Ni(111). One methyl molecule on our nine atom-per-layer Ni surface corresponds to a 1/3 coverage, assuming that methyl molecules can occupy 1/3 of the FCC sites in a full monolayer. This configuration was chosen to maximize the chance of seeing a direct recombination event. A velocity scaling thermostat was used to generate a set of independent coordinates and velocities consistent with a temperature of 500 K. Fourteen such geometries were used as initial configurations to generate dynamics trajectories of 8.5 picoseconds (or until a reactive event took place), using a time step of 0.2 femtoseconds. Temperature was controlled with a weak Nosé thermostat, using a coupling mass of 5 amu.

During the dynamics runs, the methyl and subsurface hydrogen atom oscillated in their original potential basins, until either the methyl group or hydrogen atom hopped to a neighboring site. This typically happened several times before a surfacing event occurs, and the species may have accumulated a considerable distance from each other when finally such an event takes place. A surfacing event where the methyl group was in the hollow

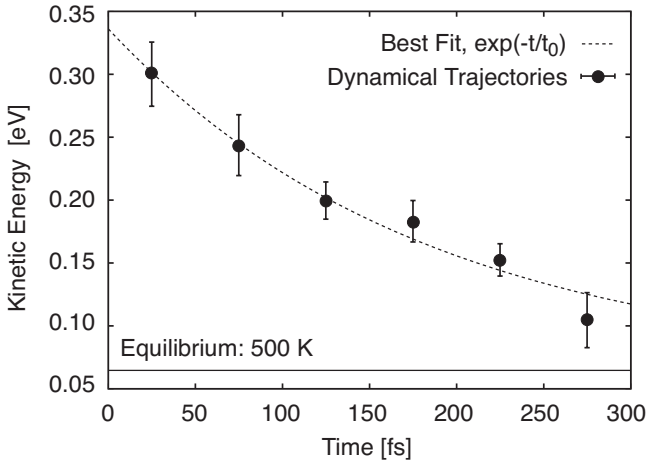

Figure A.7: Block averaged kinetic energy for the surfacing H-atom. The first 300 fs after the H-atom crosses the surface plane are broken into six 50 fs segments and averaged over each one. The error bars are the normalized standard deviation for each segment. An exponential fit to these data show a relaxation time, t_0, of 200 fs. This is expected to be an underestimation of the true relaxation time because we have used classical dynamics with a weak thermostat. These calculations show that a resurfacing H-atom will be hot due to the release of 0.6 eV of potential energy, but that this energy is dissipated to the substrate on the picosecond time scale.

site or in an on-top site adjacent to the hollow site where the hydrogen atom emerged was never observed. On average, a surfacing event took place every 4.5 ps. This time scale is consistent with a harmonic transition state theory estimate of the rate, a reaction barrier of 0.15 eV will be crossed on average after 6.5 ps at a temperature of 500 K, assuming a typical reaction prefactor of 5×10^{12} s^{-1}. A surfacing event took place in eleven of the fourteen trajectories within our time limit of 8.5 ps. Several different mechanisms were seen in these eleven trajectories where surfacing of the hydrogen atom occurred, as described below.

In one trajectory, the CH_3 group dissociated into CH_2 and an adsorbed hydrogen atom, before the subsurface hydrogen hopped to the surface. In three others, the methyl hopped to a neighboring hollow site before the hydrogen surfaced and thermalized. In four, the subsurface hydrogen hopped to an adjacent subsurface site before resurfacing. In the remaining three trajectories both the methyl and the subsurface hydrogen hopped laterally before the resurfacing event took place. In each case, the resurfacing hydrogen did not show any sign

of recombining with the methyl group. Instead, the resurfacing energy was transferred into kinetic energy of the hydrogen atom, which was dissipated into the surface on a time scale of 200 fs (shown in Fig. A.7).

This relaxation time is somewhat shorter than other calculated and measured lifetimes of hot adsorbed H-atoms on metal surfaces, in part due to a weak thermostat present during the dynamics. Klamroth and Saalfrank calculate a time scale of several picoseconds for adsorbed H-atoms to settle into binding sites on Cu(100) [131]. In these simulations, it was found that classical dynamics provides an accurate estimate of the energy decay time, as compared to full wave packet dynamics. Strömquist *et al.* [132] have done classical dynamics simulations of H/Cu(111) using a model energy landscape fit to *ab initio* data and found an energy relaxation time of 1.4 ps. Recently, Trail *et al.* [133] have found a shorter relaxation time of 0.8 ps from dynamics simulations using forces from DFT. They also estimate that electronic friction, due to electron-hole pair creation, will reduce the relaxation time scale for a H-atom on a metal surface by roughly 80% as compared to a Born-Oppenheimer classical dynamics simulation. Infrared reflection adsorption experiments [134] have also determined a sub-picosecond lifetime of 0.7 ps for H on Cu(111). The agreement between this wide range of computational techniques with experiment provides convincing evidence that energy dissipates from H-adatoms to the metal surface on the picosecond time scale.

The lateral diffusion of subsurface hydrogen and the adsorbed methyl molecule away from each other, as observed in the trajectory data, is supported by comparing the energetics between the initial configuration, in which the subsurface hydrogen is directly below the adsorbed methyl group. The energy of this configuration is 0.08 eV higher than the same species at infinite separation. This repulsive interaction between the subsurface H-atom and the surface methyl group will reduce the chance of finding a hot hydrogen atom in the vicinity of an adsorbed methyl molecule.

These dynamical trajectories support the suggestion that resurfacing hydrogen is unlikely to increase the CH_4 desorption rate, except by local heating in the case of an athermal subsurface population. In thermal equilibrium, the presence of subsurface hydrogen will not enhance the desorption rate of CH_4. Furthermore, unless there is a very high density of methyl groups on the surface, it is unlikely that a resurfacing hydrogen atom will find a

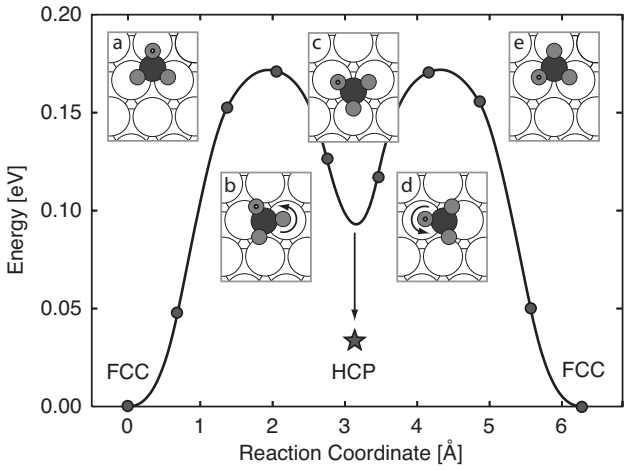

Figure A.8: The optimal mechanism for the rotation of a methyl group adsorbed on a Ni(111) surface involves first a displacement of the C atom from a FCC to an adjacent HCP hollow site. During this process, one of the hydrogen atoms maintains contact with an underlying Ni atom. In this intermediate state (indicated by $\star$), the methyl group has rotated by 60°. In the second step, the methyl group rotates about a different hydrogen atom and the C-atom gets displaced back to the original FCC site – completing the 120° rotation. This mechanism, and the high rotational barrier, indicates strong three center C-H-Ni interaction.

methyl group in the ca. 200 fs that it takes for the resurfacing energy to dissipate. Both the transition state and dynamics calculations indicate that subsurface hydrogen will not contribute to CH_4 recombination from Ni(111) under thermal catalytic conditions.

A.4.6 Methyl diffusion

The interaction of the CH_3 with the surface is of a strong three-center character. The H-atoms are strongly attracted to the nearby Ni atoms and the lowest energy configuration has the three hydrogen atoms pointed towards the adjacent surface nickel atoms. This effect has been discussed by Michaelides and Hu [135]. The strength of these bonds was investigated by finding the barrier for rotation of the CH_3 group. A NEB calculation was set up with the CH_3 sitting at a FCC hollow site in both the initial and final state, with the labeling of the H-atoms changed to reflect a 120° rotation about the surface normal going through the carbon atom. The initial chain of images was generated by a linear interpolation

between the initial and final states. Figure A.8 shows the converged minimum energy path. Remarkably, the hydrogen-metal binding is so strong that CH_3 does not rotate about the carbon atom. Instead, the carbon atom first gets displaced to an HCP site and the CH_3 group rotates 60° about one of the H-atoms (see Fig. A.8, inset a). In the second step, the carbon atom is displaced back to the FCC site and the CH_3 group rotates by another 60° about another one of the H-atoms, as shown in Fig. A.8, inset b. The overall methyl rotation barrier on Ni(111) is 0.17 eV. This illustrates how the NEB method can find a minimum energy path that is quite far removed from the initial guess and thereby reveal an unexpected transition mechanism.

A.4.7 Quantum effects

Quantum zero point and tunneling effects have been evaluated for dissociative adsorption of CH_4 on Ni(111) within the harmonic approximation. We have considered the dissociative adsorption process instead of associative desorption because previous studies have most often focussed on adsorption.

In classical transition state theory, after making a harmonic approximation for vibrational modes, the rate constant for dissociative adsorption can be written as [136, 137],

$$k_{\mathrm{cl}}^{\mathrm{hTST}} = \frac{1}{Q_{\mathrm{t,r}}^{\mathrm{init}}} \frac{\Pi_i \, \nu_i^{\mathrm{init}}}{\Pi_i \, \nu_i^{\ddagger}} \, e^{-(E^{\ddagger} - E^{\mathrm{init}})/k_B T}, \tag{A.1}$$

where ν_i^{init} and $\nu_i^{\ddagger}$ are the frequencies of harmonic vibrational modes at the initial state minimum and saddle point, respectively, and $Q_{\mathrm{t,r}}^{\mathrm{init}}$ is the product of translational and rotational partition functions of the initial gas phase molecule.

The normal modes of the CH_4 molecule in the gas phase and at the saddle point for dissociative adsorption were evaluated from the DTF forces using a finite difference scheme. The total zero point energy in the 9 vibrational modes of a gas phase CH_4 molecule was found to be 1.23 eV. At the saddle point, the frequencies obtained from small displacements of the C- and H-atoms while keeping the Ni atoms frozen gave a total zero point energy of 1.07 eV, from the 14 stable vibrational modes. The difference in the zero point energy of the initial and transition state is commonly used as a correction to the classical activation energy barrier. In this case, such a correction would lower the barrier by 0.16 eV (see Fig. A.9).

However, this approximation is only valid at low temperature when each vibrational mode is in its ground state.

A better approximation to the quantum mechanical rate constant can be obtained by using quantum mechanical partition functions for the vibrational modes in both the initial and transition states while keeping the classical mechanical definition of the normal modes. When the harmonic quantum partition function is used instead of the classical limit, the Wigner correction [138] to the classical rate constant is obtained,

$$k_{\mathrm{qm}}^{\mathrm{hTST}} = \frac{\Pi_i \sinh(x_i^{\mathrm{init}})/x_i^{\mathrm{init}}}{\Pi_i \sinh(x_i^{\ddagger})/x_i^{\ddagger}} \; k_{\mathrm{cl}}^{\mathrm{hTST}}, \tag{A.2}$$

where $x_i = h\nu_i/2k_BT$ is the ratio of the zero point energy to the thermal energy in each vibrational mode. The quantum correction to the classical rate can also be expressed as a temperature dependent correction to the classical activation energy barrier,

$$k_{\mathrm{qm}}^{\mathrm{hTST}} = e^{-\delta E/k_BT} \; k_{\mathrm{cl}}^{\mathrm{hTST}}. \tag{A.3}$$

In the case of the Wigner approximation, the correction to the classical barrier is

$$\delta E_{\mathrm{wig}} = -k_BT \ln \left[\frac{\Pi_i \sinh(x_i^{\mathrm{init}})/x_i^{\mathrm{init}}}{\Pi_i \sinh(x_i^{\ddagger})/x_i^{\ddagger}} \right]. \tag{A.4}$$

In the high temperature limit, the Wigner correction vanishes, and in the low temperature limit, it goes to the commonly used zero point energy correction,

$$\delta E_{\mathrm{zp}} = \sum_i \frac{h\nu_i^{\ddagger}}{2} - \sum_i \frac{h\nu_i^{\mathrm{init}}}{2}. \tag{A.5}$$

Figure A.9 shows a comparison of the classical barrier ($\Delta E = E^{\ddagger} - E^{\mathrm{init}}$), the zero point corrected barrier ($\Delta E + \delta E_{\mathrm{zp}}$), and the Wigner corrected barrier ($\Delta E + \delta E_{\mathrm{wig}}$) for the CH_4 dissociative adsorption barrier at temperature above 200 K. Plotting the quantum corrected rate in this way shows at which temperature quantum effects become important, and when the simple zero point energy correction can be used. At the operating temperature of a typical industrial catalyst, only a fraction of the simple zero point energy correction is appropriate.

The effect of quantum mechanical tunneling can also be estimated using a harmonic Wigner correction [139]. The ratio of the rate constant including both tunneling and zero

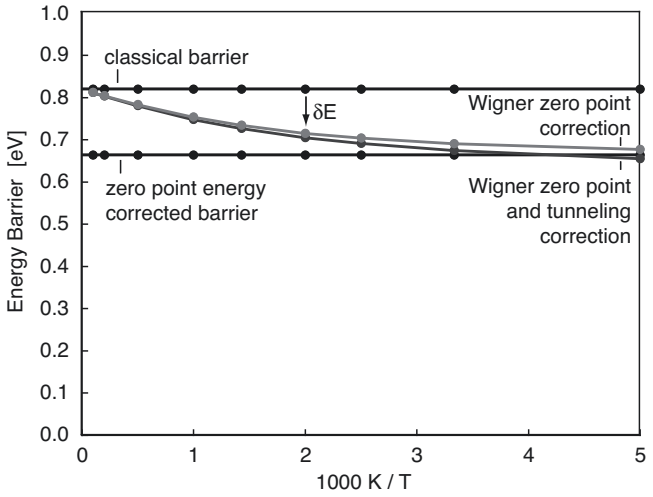

Figure A.9: Quantum mechanical correction, δE, to the energy barrier for dissociative adsorption of CH_4. The simple, commonly used zero point energy correction (Eq. A.5) shifts the classical barrier from 0.82 eV (upper line) down to 0.66 eV (lower line). This is a poor approximation at high temperature where the system is not confined to the ground state. The Wigner zero point energy correction (Eq. A.4, shown in red), which treats classical harmonic modes as quantum oscillators, smoothly switches between the simple zero point correction at low temperature to the classical barrier at high temperature. The addition of the Wigner tunneling correction (Eq. A.6, shown in blue) does not significantly change the barrier above the crossover temperature of 200 K (see Eq. A.7) for this reaction.

point energy and the rate constant that only includes zero point energy quantum effects is

$$k^{\mathrm{hTST}}_{\mathrm{qmzpt}}/k^{\mathrm{hTST}}_{\mathrm{qmzp}} = \frac{ih\nu^*/2k_BT}{\sin(ih\nu^*/2k_BT)} = \frac{x^*}{\sinh x^*}, \tag{A.6}$$

where ν^* is the imaginary frequency at the saddle point, and $x^* = ih\nu^*/2k_BT$. The correction can only be used above the crossover temperature for tunneling

$$T_c = \frac{\hbar\,|\nu^*|}{k_B}, \tag{A.7}$$

at which point the approximation diverges. The crossover temperature for the Wigner approximation is the same as that obtained from the WKB approximation [6]. Above this crossover temperature, the reaction mechanism can be thought of as over-the-barrier hop, but at lower temperature tunneling is the dominant mechanism. An appealing aspect of the Wigner tunneling correction (Eq. A.6) is that the imaginary frequency at the saddle

point, ν^*, enters into the quantum rate expression (Eq. A.2) in the same way that the real frequencies do in the Wigner zero point correction. The Wigner correction to the classical barrier (Eq. A.4) includes the tunneling correction (Eq. A.6) if the product over saddle point modes in the denominator includes the imaginary frequency mode along the reaction coordinate. For CH_4, we find that the imaginary frequency has a magnitude of 850 cm^{-1} at the saddle point which corresponds to a crossover temperature T_c of 200 K. The small difference between the Wigner correction with and without tunneling (Fig. A.9) shows how small the tunneling correction is above the crossover temperature.

A.5 Conclusions

We have carried out various calculations of associative desorption of H_2 and CH_4 to study, in particular, the role that subsurface H-atoms could play in these processes. We have carried out calculations of minimum energy paths, which are the paths with highest statistical weight in thermal systems, as well as calculations of classical dynamics and energy partitioning between vibrational modes. Although it might seem, judging from steric arguments, that a subsurface H-atom could readily react with a surface adsorbed methyl group or H-adatom, a minimum energy path for such a process was not found. Also, direct classical dynamics simulations of the surfacing of a subsurface H-atom, initially placed directly under a surface methyl group or surface bound H-atoms did not, in fourteen statistically independent trajectories, lead to associative desorption. Instead, the surface species either moves out of the way by hopping to other surface sites before the subsurface H-atom hops out to the surface, or the subsurface atom hops to adjacent subsurface sites before hopping out into a vacant surface site. The basic reason for this seems to be that the surface Ni-atoms can only catalyze H-H and H-CH_3 bond formation/rupture on the exposed, undercoordinated side. There is, furthermore, a small but significant repulsive interaction between a subsurface H-atom and a surface methyl group. Experimentally, enhanced reactivity in the presence of subsurface hydrogen has been observed [112, 117], but these experiments were carried out with high coverage of both surface and subsurface species and the effect is likely due to the local energy release of surfacing H-atoms resulting from the high energy, non-equilibrium initial state. In our classical dynamics simulations the excess kinetic energy

of a H-atom after hopping out to a surface site dropped very quickly, on the time scale of 200 fs, and no associative process was observed in fourteen trajectories. It is quite likely that a classical description of these processes is not adequate. It is, however, clear that under thermal conditions, the probability of finding an energetic atom on the surface is not affected by the presence of H-atoms in subsurface sites. The probability of finding an atom with energy E is only related to the Boltzmann factor $e^{-E/kT}$. The presence of an unstable state such as the subsurface hydrogen species does not increase the probability of finding a hot hydrogen atom on the surface under thermal conditions.

Our calculations also provide information about associative desorption of CH_4 and H_2 starting with surface species. In the saddle point configuration for CH_4 desorption, the underlying Ni-atom is lifted up from the surface plane by 0.25 Å. This reduces the energy of the saddle point configuration in a way that is analogous to strain effects [124]. An analysis of classical trajectories for desorption showed that about 15% of the saddle point energy goes into surface vibrational modes as the Ni atom relaxes back to its original position. The rest of the energy is taken up by the methane molecule and the majority, 60% of the total goes into translation, while vibration and rotation take up 20% and 5%, respectively. The symmetric and asymmetric stretches are found to be the most important vibrational modes. The principle of time reversal symmetry can be used to argue that these modes will also be most important for enhancing dissociative adsorption of methane on Ni(111), in agreement with recent experiments of Smith *et al.* [129] and Juurlink *et al.* [130].

A.6 Acknowledgments

We would like to thank Fernando Vila for for helping with the normal mode analysis, as well as Bruce Kay and Art Voter for their helpful discussions. This work was funded by the U.S. Department of Energy, Division of Materials Research, by RANNIS, the Icelandic Center for Research, and the Robert A. Welch foundation under grant No. F-1601.

A.7 Appendix: Convergence

The sensitivity of the CH_4 dissociation barrier on Ni(111) to various computational parameters is given in Table A.3. For each parameter, the energy difference is with respect to our most accurate calculation described above. The most sensitive computational parameter in our calculation is k-point sampling. Given more computing power, this should be increased to verify convergence. For the smaller, four atom per layer system, in which k-point sampling will be even more important, going from a 2×2×1 Monkhost-Pack k-point mesh to a 4×4×1 mesh did not change the binding energies by more than 0.1 eV. Spin polarization also plays a significant role, raising the barrier by 30%. Finally, surface relaxation and the number of layers in the Ni(111) slab are both needed to allow the large surface relaxation found at the transition state and to lower the barrier by 20%.

Table A.3: Sensitivity of the CH_4 dissociation energy barrier on Ni(111) with respect to computational parameters. Energy differences are with respect to a five layer, nine nickel atoms per layer slab with the bottom two layers frozen, a plane wave energy cutoff of 350 eV, a 2×2×1 Monkhost-Pack k-point mesh, spin polarized calculation for which an activation energy barrier of 0.82 eV was calculated.

Energy	Computational Parameter
0.30 eV	K-point sampling (Γ to 2×2×1)
0.25 eV	Spin polarization
0.15 eV	Surface relaxation (frozen to relaxed)
0.10 eV	System size (four to nine atoms per layer)
0.05 eV	Number of surface layers (four to five)
0.02 eV	Plane wave energy cutoff (240 eV to 350 eV)

VITA

Andri Arnaldsson was born in Reykjavík Iceland in April 1976. After a relatively uneventful childhood he graduated from Menntaskólinn in Reykjavík with a major in physics in 1996 and later with a B.Sc. degree in chemistry from the University of Iceland in 2000. After a short stint in the job market he enrolled at the University of Washington in 2001 and subsequently received his Ph.D. in chemistry in 2007.